DEVELOPMENT OF A SYSTEM FOR THE INVESTIGATION OF SPINNAKERS USING FLUID STRUCTURE INTERACTION METHODS

Development of a System for the Investigation of Spinnakers using Fluid Structure Interaction Methods

Proefschrift

ter verkrijging van de graad van doctor
aan de Technische Universiteit Delft,
op gezag van de Rector Magnificus prof. dr. ir. T.H.J.J. van der Hagen,
voorzitter van het College voor Promoties,
in het openbaar te verdedigen op maandag 12 februari 2018 om 12:30 uur

door

Hannes Florian RENZSCH

Diplom-Ingenieur (Fachhochschule) Schiffbau,
Fachhochschule Kiel, Kiel, Duitsland,
geboren te Bonn, Duitsland.

Dit proefschrift is goedgekeurd door de

promotor: prof. dr. ir. R.H.M. Huijsmans
copromotor: dr. ir. M.I. Gerritsma

Samenstelling promotiecommissie:

Rector Magnificus,	voorzitter
Prof. dr. ir. R.H.M. Huijsmans,	Technische Universiteit Delft
Dr. ir. M.I. Gerritsma,	Technische Universiteit Delft

Onafhankelijke leden:

Prof. dr. G. Thomas	University College London
Prof. Dr.-Ing. K.U. Graf	University of Applied Sciences Kiel
Prof. dr. P.A. Wilson	University of Southampton
Prof. dr. A.E.P. Veldman	Rijks Universiteit Groningen
Prof. dr. ir. M.L. Kaminski	Technische Universiteit Delft
Prof. ir. J.J. Hopman	Technische Universiteit Delft, reservelid
Keywords:	FSI, CFD, FEA, Membrane, Sails

CONTENTS

SUMMARY

While historically sailmaking and saildesign were considered as arts, in the 20th century, mainly from the 1980s onwards, engineering sciences have started to play an important role. Two fields are of particular interest: structural and fluid mechanics. Initially, the sails were tested in the wind tunnel, aggregate flow forces measured and the interaction of flow and structural behaviour implicitly captured by visual observation. No quantitative structural assessment was available in these experiments. With the advent of affordable powerful personal computers, programs were developed to compute the flow around sails and the structural reaction to the resulting forces. These programs were based on significantly simplified assumptions about the fluid mechanics - potential flow - as well as the complete neglect of any unsteady behaviour of flow or coupled result. These simplifications limit the applicability of these programs to upwind sails, essentially this airfoils working at small angles of attack. As downwind sails do not comply with these limitations they are still tested in the wind tunnel with the associated scale effects and limited outcome of quantitative results.

Within this thesis a method is being developed to capture the interaction between the complex viscous flow around downwind sails and compute the structural answer to the resulting forces. First a structural model suitable for downwind sails is developed. This is coupled to a commercial solver for simulations of viscous flow. The individual parts (structural and flow simulation as well as coupling) and the entire method are verified and validated. Finally an application example is given.

First, the structural model and coupling to the flow solver are developed. The particular challenge regarding the structural model is the requirement to compute the complex behaviour of downwind sails. By design these sails have negligible bending stiffness with the material being stiff in tension but without any meaningful compressive stiffness. To this end the classic CST-element is extended by a wrinkling model, a robust solver able to capture the resulting non-linearities is implemented. This model is coupled to a commercial RANS solver by a bespoke coupling algorithm. This algorithm ensures the conservative transfer of forces and deformations while keeping the coupled simulation stable.

Next, to ensure applicability of the structural and flow simulation models as well as the coupling, they are verified for grid and time step dependency and validated against analytical or experimental data. As no experimental data was freely available on the particular case of downwind sails, wind tunnel tests were conducted to provide at least aggregate flow forces and flying shapes. Particularly the structural simulation and coupling were successfully verified and validated, the simulation of partially separated flow around highly curved surfaces like downwind sails exhibited a strong sensitivity to e.g. small changes of the angle of attack. Validation of the flow simulation was hampered by uncertainties in the experimental data.

Finally, the method is used to compare three sail designs on a hypothetical yacht based on the AC90-rule. The impact of the sail design changes is clearly shown with small variations in sail (profile) depth resulting in very much different optimal angles of attack.

Improvements to the method could in particular be achieved by implicit or strong coupling of flow and structural simulation, this would yield time-accurate information on the sails unsteady behaviour. Further, even more involved flow simulation methods, e.g. large or detached eddy simulation instead of turbulence modelling might improve the accuracy of the flow simulation.

SAMENVATTING

Historisch wordt het ontwerpen en produceren van zeilen voor zeiljachten gezien als een kunst. Vanaf de jaren 1980 is echter de ontwikkeling ingezet om diverse geavanceerde rekenmethoden te ontwikkelen en gebruiken om meer grip te krijgen op dit complexe proces. Twee vakgebieden zijn hierin met name van belang: mechanica en stromingsleer. Voor het eerste onderzoek werden windtunnels gebruikt om zeilen op modelschaal te testen; de uitgeoefende krachten werden gemeten en de zeilvorm werd visueel vastgesteld. Het was echter niet mogelijk om een kwalitatieve analyse van deze vervorming te maken. Met het toenemen van de rekenkracht van computers werd het mogelijk om de stroming van de wind om de zeilen te berekenen, samen met de uitgeoefende krachten op de constructie. Beide delen van de software waren gebaseerd op vereenvoudigde modellen, zowel voor de stroming – potentiaal code – als voor de interactie tussen de stroming en de zeilen zelf. Deze vereenvoudigen beperken het gebruik van deze software tot aandewindse condities waarin de vleugelprofielen alleen onder kleine invalshoeken kunnen werken. De zeilen voor ruimewindse koersen vallen niet binnen de aannames van de software en moeten daardoor nog steeds in windtunnels getest worden; dit met inachtname van alle schaaleffecten en beperkte beschikbaarheid van kwalitatieve resultaten.

In deze promotie is een methode ontwikkeld om de interactie te beschrijven tussen de complexe viskeuze stroming rondom ruimewindse zeilen en vervorming van de zeilen als het gevolg van deze stroming. Allereerst is een mechanisch model ontwikkeld die geschikt is voor de ruimewindse zeilen. Deze is vervolgens gekoppeld aan een commerciële stromingssoftware die geschikt is voor het simuleren van viskeuze stromingen. Beide individuele delen van de software (zowel om de vervorming van de zeilen als de stroming te beschrijven) zijn afzonderlijk van elkaar én samen geverifieerd en gevalideerd. Vervolgens wordt er aan de hand van een voorbeeld getoond hoe het ontwikkelde model kan worden toegepast.

Om een correcte beschrijving van de modellen te toetsen zijn deze geverifieerd voor rekenrooster- en tijdsafhankelijkheid tegen beschikbare analytische of experimentele data. Aangezien er geen experimentele data beschikbaar was voor ruimewindse zeilen werden de resultaten vergeleken met de gemeten krachten en geobserveerde vormen van de zeilen bij modeltesten. Met name de vervormings- en koppelingsmodellen werden succesvol geverifieerd en gevalideerd. Het loslaten van de stroming om sterk gekromde oppervlakken, zoals het geval is bij ruimewindse zeilen, zorgt voor een hoge gevoeligheid voor kleine verschillen in zeilvorm. Het valideren van de stromingssimulatie werd daarnaast bemoeilijkt door onzekerheden in de beschikbare experimentele data.

Tenslotte is het bovenstaand beschreven model toegepast om drie ontwerpen van zeilen met elkaar te vergelijken voor een niet bestaand AC90 zeiljacht. De invloed van

verschillen in de zeilontwerpen zijn duidelijk zichtbaar; kleine wijzigingen in zeil (pro-fiel) diepte resulteerden in sterk verschillende optimale invalshoeken.

Het bovenstaande model kan verbeterd worden door de de koppeling tussen het vervormings- en stromingsmodel aan te passen. Dit zal leiden tot een nauwkeurige be-schrijving van het dynamische gedrag van de zeilvorm in de tijd. Daarnaast zal het toe-passen van meer ontwikkelde, en meer nauwkeurige stromingsmodellen, zoals de Large Eddy Simulation of Detached Eddy Simulation de turbulentie beter kunnen beschrijven en daarmee dus ook leiden tot een betere voorspelling van de zeilvorm.

NOMENCLATURE

AWA   Apparent Wind Angle; Resultant incident wind angle from true wind and headwind a moving sailing yacht encounters

AWS   Apparent Wind Speed; Resultant incident wind speed from true wind and headwind a moving sailing yacht encounters

Ax, Ay   Force Areas; Flow forces normalised by dynamic pressure head from incident flow

CFD   Computational Fluid Dynamics; Numerical method to calculate flow behaviour

Co   Courant Number; In finite volume methods: The ration between volumeflux through a cell face per timestep and the cells volume

FEM   Finite Element Method; Numerical method to compute behaviour of structures under load

FSI   Fluid-Structure-Interaction; Numerical simulation coupling flow forces acting on a body and the structural behaviour of the body resulting thereof to account for effects acting both ways

Re   Reynolds Number; The ratio between flow velocity times flow length on surface and fluid kinematic viscosity

Spinnaker   Headsail for use with the wind aft of the beam; resembling a triangular cutout of a balloon, attached to the boat only via the three corners

SST-Model   Shear-Stress-Transport turbulence model; developed by Menter, based on the near wall modelling of the k-ω turbulence model and the far-field modelling of the k-ε turbulence model

TFWT   Twisted flow wind tunnel; Wind tunnel with flow conditioning to mimic the atmospheric boundary layer and incident flow angle distribution a moving sailing yacht encounters

VMG   Velocity Made Good; Effective velocity of a yacht relative to a certain direction, typically directly up- or downwind

VPP   Velocity Prediction Program; Program to determine the achievable velocity of a yacht for a given set of wind conditions

1

INTRODUCTION

1.1. SAILS AND SAIL DESIGN

Historically, sails are one of the major propulsion methods for yachts and ships. Despite this, due to the limitations of the available materials, little effort has been put into the optimisation of sails until the 20th century. Until the 1950s sails were made out of hemp or cotton. The cut of these sails was based purely on experience, the sails had to be "broken in" and regularly recut to correct for stretch and deformation. Only the arrival of synthetic sailcloth enabled the sailmakers to design sails to a particular shape. Still, due to the limited engineering possibilities in those days, sailmaking was more an art than a science. The arrival of computers, powerful enough to perform the necessary calculations for three-dimensional design by dedicated CAD programs and the involved engineering calculations, enabled the sailmakers to optimise the sails during the design stage and not only by trial and error later on. Major drivers of the development of dedicated software were international competitions like the America's Cup, where significant research and development budgets were available.

Generally, sails can be classed in two categories: those creating driving force by acting like a wing and those acting like a drag body. Historically this difference separated upwind sails like main and jib / genoa from downwind sails like a spinnaker. In fluid mechanical terms this separation is akin to creating lift by attached flow and creating drag by separated flow. Recently this distinction has been vanishing as spinnakers are now typically designed to operate at smaller wind angles with at least partially attached flow.

From a design viewpoint the challenge designing upwind sails is to keep the designed airfoil-like shape despite the large and varied stresses acting on the material. The actual displacement of the sail under load and the strains are quite small in design-conditions. On a downwind sail a major challenge is to achieve an effective flying shape under wind loads as the sail behaves like a section cut out of a balloon. The only fixed points known are the leads of halyard, tackline / aftguy and sheet. The remainder of the sail can basically take any shape possible within the limits of the sails cut. The stresses and strains on a downwind sail are usually only a small fraction of the allowable stress of the material, the displacement from the originally designed shape often quite large.

1.2. SAIL ANALYSIS AND OPTIMISATION

As in any engineering application, testing, evaluation and optimisation are major parts of the way to a successful sail design. While the design of a typical sail for the average cruising yacht is still based mostly on experience, in racing yacht application more involved methods are required to obtain optimal performance. Typically, these are experimental testing and numerical simulation. The analysis of sails is complicated by the fact, that they are flexible structures with their flying shape being determined by the interaction of flow forces and structural behaviour. Therefore, evaluation of flow as well as structural behaviour has to be carried out in unison to achieve a correct result for both.

For the choice of the method used, typically a distinction is made between upwind and downwind sails, as above. Basically it can be stated that, with the sails trimmed for optimal efficiency, the flow around upwind sails is mostly attached. The flow around downwind sails is typically characterised by spontaneous, possibly periodic separation with the sails trimmed for maximum lift. Structurally, upwind sails can be described as highly loaded membranes with little curvature and little displacement under load compared to the designed shape. Due to this, small errors in the replication of the structure can lead to significant errors of the sails flying shape. The structure of downwind sails is characterised by much higher curvature, significantly smaller loads and large displacements of the sails surface compared to the designed shape. Due to this, small errors in the replication of the structure have little impact on the flying shape.

Due to the small models necessitated by wind tunnel size, the major shortcomings of wind tunnel testing are scale effects of flow and structural behaviour. Using reasonably scaled structural elements of rigging it is impossible to achieve Reynolds similarity of the flow. Still, complicated flow features, like separation, are captured quite accurately. Similarly, structural similarity usually can not be achieved. Due to manufacturing constraints of the models, usually the panellisation of the sails surface is significantly simplified, a correct stress-strain-weight relationship of the cloth usually can not be achieved either. The advantages of wind tunnel testing are that flow around and structure behaviour of the sails are directly interdependent like at full scale and that the sails can be trimmed like on the boat.

Simulations are typically carried out in full scale. While for upwind sails the major challenge is accurate structural modelling, for downwind sails it is the correct prediction of flow separation and the sails large displacements. The attached flow around upwind sails can be satisfactorily simulated using inviscid flow modelling,. e.g. by Vortex-Lattice-Methods. The partially detached flow around downwind sails necessitates high fidelity modelling of the viscous flow using RANS methods with involved turbulence models to correctly capture the near wall behaviour. To achieve the correct flying shape, in the case of upwind sails, all structural features have to be modelled correctly. This requires high grid resolutions and advanced model element libraries, yet, with current finite element programs, it is perfectly feasible. For spinnakers the structural model can be somewhat simplified, yet it has to be able to cope with significant geometrical non-linearities due to the large displacements and correctly model the structurally non-linear behaviour of sail cloths under compression.

For the reasons stated above, numerical simulation currently is the major design tool for upwind sails. Downwind sails are still mostly tested in wind tunnel experiments. The

aim of this thesis is to develop a method that allows the accurate modelling of downwind sail using Fluid-Structure-Interaction methods, attempting to rival or surpass the value of wind tunnel experiments for downwind sail design.

1.3. PROBLEM DEFINITION AND OBJECTIVES

The value of evaluating downwind sails by testing scale models in the wind tunnel is limited by several factors. Mainly these are scale effects, affecting the accuracy of transferring the measured forces to full scale and the need to build a new model of the sail for every change in sail cut. Further the structural layout of the sail is usually significantly simplified for the model. Simulation of viscous flow and of a non-idealised structure allows to evaluate the flow around a sail or its structural behaviour in a timely manner without the influence of scale effects. To assess the quality of a sail, the computation of flow and structure have to be coupled to evaluate not only the separate aspects but the interaction thereof.

The aim of the present work is therefore to develop a system that allows the accurate coupled simulation of the flow around and the structural behaviour of downwind sails in full scale. This includes the development of a finite element code capable of simulating the highly non-linear behaviour of such sails in a robust and efficient fashion and the interface coupling this FE-code to an existing RANS flow code in an efficient manner.

1.4. OUTLINE OF THE THESIS

Within this thesis first the current state of the art of experimental and numerical sail testing is presented in Chapter 2. Due to simulation methodology the separate reviews are given for flow and structural simulation and fluid-structure-interaction coupling.

The mathematical model for the structural simulation is discussed in Chapter 3, starting with the classical triangular membrane element and continuing with extensions of the model for the computation of wrinkling behaviour. Following that, two different solution strategies employed during the present work are discussed.

A short synopsis of the two typical approaches to coupling of flow and structural simulation is given in Chapter 4.

As any simulation is only as good as its validation, in-depth validation of flow and structural simulation and the coupled approach is given in Chapter 5. While validation is based on literature data as far as possible, some wind tunnel experiments were required to generate suitable data. These are presented in detail.

An application example of the method developed within this work is presented in Chapter 6. To demonstrate the capabilities of the method several parametrically varied asymmetric spinnaker designs for the stillborn AC90 class are compared.

Finally, the results are discussed and recommendations are given in Chapter 7.

2

STATE OF THE ART

2.1. EXPERIMENTAL TESTING

First steps to quantify sail performance were taken by *Davidson* [1] in 1936 by measuring driving and side force and heeling moment on the sails of the yacht *Gimcrack* at full scale, resulting in the so-called *Gimcrack-Coefficients*, the first set lift and drag data for sailing yacht rigs. Modern methods of sail testing in a wind tunnel were mostly developed at the MIT by *Hazen* [2] in the context of the MHS ocean racing handicapping project and at the Wolfson Unit, Univ. of Southampton's wind tunnel by *Marchaj* [3] and *Claughton et al.* [4]. These developments focussed mostly on measurement techniques and generation of generalised data for evaluation of yacht sails without individual tests.

A major advance on testing method of downwind sails was achieved by the commissioning of the University of Auckland's *Twisted Flow Wind Tunnel* by *LePelley et al.* [5]. While upwind sails encounter a comparatively homogeneous flow field, the incident flow on downwind sails has major vertical gradients of velocity and direction. Modelling this flow field by selective blockage of the flow and directional vanes allows to evaluate, and in consequence design, downwind sails for these particular flow conditions.

The next major advance came from Auckland as well by the introduction of real-time velocity prediction into the evaluation of the generated forces and moments (*LePelley et al.* [6]). Commonly, during wind tunnel tests, the sails were either trimmed for maximum drive, optimal lift to drag ratio or the trim systematically varied to generate response surfaces. Real-time velocity prediction allows to include the boat's particulars into wind tunnel testing. This effectively limits the allowed heeling moment, requiring the wind tunnel operator to trim for maximum boat speed for given true wind angle and speed.

One of the most recent advances is the introduction of flying shape capturing methods at various wind tunnels and on full scale sails (*LePelley et al., Graf et al., Mausolf et al.* [7–9]), based on various kinds of photogrammetric techniques. These techniques have been further extended by shape capturing in a time series and simultaneous pressure measurements on these sails, e.g. by *Motta et al.* [10] and *Deparday et al.* [11, 12].

A significant challenge is the acquisition of good validation data, measurements of

5

two-dimensional flow around sail-like profiles were presented by *Collie* and *Wilkinson* [13, 14].

Flow forces for parametrically varied spinnaker-like three-dimensional shapes were presented by *Lasher* [15]. Unfortunately local flow behaviour was not captured during these measurements and the models were quite small.

During an intensive study of pressure distributions on various sail configurations in 2009 and 2010 *Viola et al.* produced a copious amount of qualitative data [16–19]. Significant further research has been invested into the understanding of the particular local properties of the flow around downwind sails or similar two-dimensional sections (e.g. *Flay et al.* [20] or *Viola et al.* [21]).

2.2. SIMULATION

A program for simulations using Fluid-Structure-Interaction (FSI) basically consists of three major parts: Flow simulation, structural simulation and coupling. Applied to the analysis of downwind sails these are the simulation of viscous, turbulent, possibly detached single phase flow, the structural behaviour of thin, flexible, anisotropic materials undergoing large displacements and the two-way coupling thereof.

2.2.1. FLOW SIMULATION

Fluid flow can be simulated using two basic paradigms: ideal, inviscid fluids or viscous fluids. Initial application of CFD to sails were limited to inviscid Vortex-Lattice-Methods (*Thrasher et al.* [22]), sometimes with empirical extensions (*Register et al.* [23]). A comparison of measured and simulated forces of upwind sails was presented by *Milgram et al.* [24]. While the inviscid approach holds quite well for the simulation of flow around upwind sails where little or no flow separation occurs it is not suitable to simulate the flow in any sailing state where flow separation has a significant impact on the flow's behaviour. With the above mentioned empirical extensions it may be possible to detect the onset of flow separation, yet the correct calculation is impossible.

To correctly simulate partially separated flow viscous fluid models have to be used. The earliest RANS calculations of the flow around sails in downwind conditions were carried out in 1996 by *Hedges et al.* [25], showing the necessity of taking viscous flow behaviour into account. *Collie et al.* carried out a large scale investigation of the impact of the choice of turbulence models and grid parameters on the simulated flow around upwind [26, 27] and downwind [13, 28, 29] sails using 2-D profile slices of the sail. Several authors have simulated the three dimensional flow around upwind sails including geometry optimisation or permutation methods using RANS methods [30–32]. An in-depth investigation of the effect of grid resolution in three-dimensional downwind cases was presented by *Viola* [33].

Most recent research in the simulation of viscous flow around downwind sails, e.g. *Nava et al.* [34], shows that turbulence resolving methods like LES have the *potential* to significantly improve the capturing of separation points compared to RANS methods, albeit at a significantly higher computational effort (by a factor of 120).

2.2.2. STRUCTURAL SIMULATION

To simulate the structural behaviour of the sail using a finite-element method basically two models can be used: shell or membrane elements. Shell elements have in-plane as well as bending stiffness, typically modelled by solving for six degrees of freedom (DoF) per node (*Levy et al.* [35]) or by introducing a hinge stiffness at the edges (*Grinspun, Wardetzky et al.* [36, 37]). Membrane elements have only in-plane stiffness, reducing the degrees of freedom to three per node (*Zienkiewicz* [38]. In a strict sense the shell element is the correct description, however, if the ratio between bending and direct stiffness approaches zero, as it typically does for sailcloths used for downwind sails, the difference between shell and membrane elements vanishes.

Very important for the correct simulation of the sail's structural behaviour is the ability of the model to correctly model the behaviour of the material under compressive stress as shown by *Heppel* [39]. In the case of shell elements this is done by a buckling analysis with the buckling strain approaching zero as the bending stiffness vanishes. This buckling analysis, if done correctly, actually captures the out of plane deformations of the material, yet it requires a fine enough discretisation of the surface and is quite expensive computationally. For membrane elements typically a wrinkling model is implemented keeping the direct stresses equal or larger than zero. The wrinkles are assumed to be on sub-element scale, therefore resulting out of plane deformations of the real material are not represented. In this thesis, we will limit ourselves to wrinkling models.

Historically, first wrinkling models were formulated by *Stein et al.* and *Miller et al.*, based on properties observed during experiments with isotropic membranes [40, 41]. In these models the material properties were modified, giving uniaxial stress-strain behaviour. In later models the strain vector is modified by introducing a wrinkling strain, artificially shortening the surface normal to the wrinkles, to capture the actual structural behaviour of the surface (*Kang et al., Lu et al.* [42, 43]). Validation data can be found in various published experiments experiments (*Stein et al., Wong et al.* [40, 44])

In 2002 a promising approach to the solution of FEA cases with large deformations, even structural failure, was proposed by *Hao et al.* [45]. In the proposed *Moving Particle Finite Element Method* it is attempted to combine the advantages of a classical finite element approach with those of a meshfree method. In the paper application examples indicating the suitability for the simulation of large deformations are shown. Evaluating the applicability of such a method to the particular issues of sail structures is beyond the scope of this thesis.

2.2.3. FLUID-STRUCTURE-INTERACTION

Due to the progress of development of flow simulation techniques, starting with potential flow methods, first FSI applications on sails were for upwind sails. One of the first methods published was by *Fukasawa et al.* [46]. *LeMaître et al.* [47, 48] developed a model where the structural behaviour of the sail was based solely on string elements, the aerodynamic loads were initially mimicked by a simple analytical distribution, later by an inviscid flow model. The first practical applications of a FSI code coupling the FEA model of the sails with a solver for inviscid flow were reported by *Heppel* and *Ranzenbach et al.* [39, 49, 50]. Current applications have for example been published by *Malpede et al.* [51].

Since the beginning of work on this thesis the work on RANS-based sail-FSI has gathered pace internationally. The first report prior to the author's work was by *Richter et al.* [52]. In this case the two solvers (RANS and FEA) were coupled in a so-called batch mode, having an external script trigger two separate programs with data exchange by file.

Since the first publication of the author on the work documented within this thesis [53] various practitioners have published approaches to the problem of RANS-based sail-FSI. Basically, two general approaches can be distinguished: Fully explicit coupling by batch mode and attempts at capturing the sail's dynamics to some extent. The most relevant publications regarding batch-mode coupling were by work-groups associated to *Heppel et al.* [54, 55]. Examples of the second group can be found in the work of *Lombardi et al.* [56] and *Durand et al.* [57]. While *Lombardi et al.* use Aitken underrelaxation to stabilise the coupling, *Durand et al.* have modified the batch mode coupling approach by introducing an approximation of the flow Jacobian matrix, calculated by potential flow methods, into the structural solution.

A different focus is present in the work of *Trimarchi et al.* [58], here the relevance lies in the application of specialised thin shell elements for the structural modelling instead of the usual membrane elements.

The author's work is present in various publications ([8, 53, 59–62]), several of the above authors have based parts of their work on the author's publications.

REFERENCES

[1] K. S. M. Davidson, *Some experimental studies of the sailing yacht,* Transactions of the Society of Naval Architects and Marine Engineers **44**, 288 ff (1936).

[2] G. S. Hazen, *A model of sail aerodynamics for diverse rig types,* in *New England Sailing Yacht Symposium* (1980).

[3] C. A. Marchaj, *Aero-Hydrodynamics of Sailing* (Adlard Coles Ltd., London, 1988).

[4] A. R. Claughton and I. M. C. Campbell, *Wind tunnel testing of sailing yacht rigs,* in *13th International Symposium on Yacht Design and Construction (HISWA)* (1994).

[5] D. L. Pelley, P. Ekblom, and R. G. J. Flay, *Wind tunnel testing of downwind sails,* in *High Performance Yacht Design Conference* (2006).

[6] D. L. Pelley and P. Richards, *Effective wind tunnel testing of yacht sails using a real-time velocity prediction program,* in *The 20th Chesapeake Sailing Yacht Symposium* (2011).

[7] D. J. L. Pelley and O. Modral, *V-spars: A combined sail and rig shape recognition system using imaging techniques,* in *3rd High Performance Yacht Design Conference* (2008).

[8] K. Graf, C. Boehm, and H. Renzsch, *Cfd- and vpp-challenges in the design of the new ac90 america's cup yacht,* in *19th Chesapeake Sailing Yacht Symposium* (2009).

[9] J. Mausolf, J. Deparday, K. Graf, H. Renzsch, and C. Boehm, *Photogrammetry based flying shape investigation of downwind sails in the wind tunnel and at full scale on a sailing yacht,* in *The 20th Chesapeake Sailing Yacht Symposium* (2011).

[10] D. Motta, R. Flay, P. J. Richards, D. J. L. Pelley, J. Deparday, and P. Bot, *Experimental investigation of asymmetric spinnaker aerodynamics using pressure and sail shape measurements,* Ocean Engineering **90**, 104 (2014).

[11] J. Deparday, P. Bot, F. Hauville, B. Augier, and M. Rabaud, *Full-scale flying shape measurement of offwind yacht sails with photogrammetry,* Ocean Engineering **127,** 135 (2016).

[12] J. Deparday, *Experimental studies of Fluid-Structure Interaction on Downwind sails,* Ph.D. thesis, Ecole Navale de Lanvéoc-Poulmic (2016).

[13] S. J. Collie, *Application of Computational Fluid Dynamics to Two-Dimensional Downwind Sail Flows,* Ph.D. thesis, Department of Mechanical Engineering and Engineering Science, School of Engineering, University of Auckland (2006).

[14] S. Wilkinson, *Partially Separated Flow Around Masts and Sails,* Ph.D. thesis, University of Southampton (1984).

[15] W. C. Lasher, *Experimental force coefficients for a parametric series of spinnakers,* in *16th Chesapeake Sailing Yacht Symposium* (2003).

[16] I. M. Viola and R. G. J. Flay, *Force and pressure investigation of modern asymmetric spinnakers,* International Journal of Small Craft Technology, Trans. RINA **151** (2009).

[17] I. M. Viola and R. G. J. Flay, *Pressure distribution on modern asymmetric spinnakers,* International Journal of Small Craft Technology, Trans. RINA **152**, 41 (2010).

[18] I. M. Viola and R. G. J. Flay, *On-water pressure measurements on a modern asymmetric spinnaker,* in *Proceedings of the 21th International HISWA Symposium on Yacht Design and Construction* (2010).

[19] I. M. Viola and R. G. J. Flay, *Sail pressures from full-scale, wind-tunnel and numerical investigations,* Ocean Engineering (2011).

[20] R. G. J. Flay, A. Piard, and P. Bot, *Aerodynamics of a highly cambered circular arc aerofoil: Experimental and cfd investigations,* in *International Conference on Innovation in High Performance Sailing Yachts, 4th Edition,* edited by P. Bot (2017).

[21] I. M. Viola and A. Arredondo-Galeana, *The leading-edge vortex of yacht sails,* in *International Conference on Innovation in High Performance Sailing Yachts, 4th Edition,* edited by P. Bot (2017).

[22] D. F. Thrasher, D. T. Mook, and A. H. Nayfeh, *A computer-based method for analyzing the flow over sails,* in *4th Chesapeake Sailing Yacht Symposium* (1979).

[23] D. S. Register and R. K. Irey, *Analysis of steady flow over interacting sails,* in *6th Chesapeake Sailing Yacht Symposium* (1983).

[24] J. H. Milgram, D. B. Peters, and D. N. Eckhouse, *Modelling iacc sail forces by combining measurements with cfd,* in *11th Chesapeake Sailing Yacht Symposium* (1993).

[25] K. L. Hedges, P. J. Richards, and G. D. Mallinson, *Computer modelling of downwind sails,* Journal of Wind Engineering and Industrial Aerodynamics **63**, 95 (1996), special issue on sail aerodynamics.

[26] S. J. Collie, M. G. Gerritsen, and P. S. Jackson, *A Review of Turbulence Modelling for use in Sail Flow Analysis,* Tech. Rep. (Department of Engineering Science, University of Auckland, 2001).

[27] S. J. Collie, M. G. Gerritsen, and M. J. O'Sullivan, *Numerical simulation of the turbulent flow past upwind yacht sails,* (2002), submitted to Journal of Wind Engineering and Industrial Aerodynamics 2002.

[28] S. J. Collie, P. S. Jackson, M. G. Gerritsen, and J. B. Fallow, *Two-dimensional cfd-based parametric analysis of downwind sail designs,* International Journal of Small Craft Technology **146**, 21 (2004).

[29] S. J. Collie and M. G. Gerritsen, *The challenging turbulent flows past downwind yacht sails and practical application of cfd to them,* in *2nd High Performance Yacht Design Conference* (2006).

[30] J. Yoo, J. Kim, I.-R. Park, H. Ahn, and S.-H. Van, *Cfd calculations aon the sail-like three dimensional airfoils,* in *2nd High Performance Yacht Design Conference* (2006).

[31] B. Krebber and K. Hochkirch, *Numerical investigation of the effects of trim for a yacht rig,* in *2nd High Performance Yacht Design Conference* (2006).

[32] J. Paton and H. Morvan, *Using computational fluid dynamics to model sail interaction–the [']slot effect' revisited,* Journal of Wind Engineering and Industrial Aerodynamics **97**, 540 (2009).

[33] I. M. Viola, *Downwind sail aerodynamics: A cfd investigation with high grid resolution,* Ocean Engineering **36**, 974 (2009).

[34] S. Nava, J. Cater, and S. Norris, *Large eddy simulation of downwind sails,* in *International Conference on Innovation in High Performance Sailing Yachts, 4th Edition,* edited by P. Bot (2017).

[35] R. Levy and W. R. Spillers, *Analysis of Geometrically Nonlinear Structures,* second edition ed. (Kluwer Academic Publishers, 2003).

[36] E. Grinspun, *A discrete model of thin shells,* in *Discrete Differential Geometry: An Applied Introduction (Desbrun, Grinspun, Schröder, Wardetzky) SIGGRAPH Asia 2008* (2008).

[37] M. Wardetzky, M. Bergou, A. Garg, D. Harmon, D. Zorin, and E. Grinspun, *Simple and efficient implementation of discrete plates and shells,* in *Discrete Differential Geometry: An Applied Introduction (Desbrun, Grinspun, Schröder, Wardetzky) SIGGRAPH Asia 2008* (2008).

[38] O. C. Zienkiewicz, *The finite element method in engineering science <dt.>* (Hanser, 1971).

[39] P. Heppel, *Accuracy in sail simulation: Wrinkling and growing fast sails,* in *1st High Performance Yacht Design Conference* (2002).

[40] M. Stein and J. M. Hedgepeth, *Analysis of Partly Wrinkled Membranes*, Tech. Rep. (NASA, 1961).

[41] R. K. Miller and J. M. Hedgepeth, *An algorithm for finite element analysis of partially wrinkled membranes,* AIAA Technical Notes **82**, 1761 (1982).

[42] S. Kang and S. Im, *Finite element analysis of wrinkling membranes,* Journal of Applied Mechanics **64**, 263 (1997).

[43] K. Lu, M. Accorsi, and J. Leonard, *Finite element analysis of membrane wrinkling,* International Journal for Numerical Methods in Engineering **50**, 1017 (2001).

[44] Y. W. Wong and S. Pellegrino, *Wrinkled membranes part i: Experiments,* Journal of Mechanics of Materials and Structures **1**, 3 (2006).

[45] S. Hao, H. S. Park, and W. K. Liu, *Moving particle /nite element method,* International Journal for Numerical Methods in Engineering **53**, 1937 (2002).

[46] T. Fukasawa and M. Katori, *Numerical approach to aeroelastic responses of three-dimensional flexible sails,* in *11th Chesapeake Sailing Yacht Symposium* (1993).

[47] O. L. Maître, S. Huberson, and J. E. S. de Cursi, *Application of a non-convex model of fabric deformations to sail cut analysis,* Journal of Wind Engineering and Industrial Aerodynamics **63**, 77 (1996), special issue on sail aerodynamics.

[48] O. L. Maître, J. E. S. D. Cursi, and S. Huberson, *Large displacement analysis for ideally flexible sails,* European Journal of Mechanics - A/Solids **17**, 619 (1998).

[49] R. Ranzenbach and Z. Xu, *Fluid-structure interaction simulation of a code zero sail,* in *I International Symposium on Yacht Design and Production* (2004).

[50] R. Ranzenbach and Z. Xu, *Sail aero-structures: Studying primary load paths and distortion,* in *17th Chesapeake Sailing Yacht Symposium* (2005).

[51] S. Malpede, F. D'Angeli, and R. Bouzaid, *Advanced structural analysis method for aeroelastic simulations of sails,* in *The Third International Conference on Innovation in High Performance Sailing Yachts* (2013).

[52] H. J. Richter, K. C. Horrigan, and J. B. Braun, *Computational fluid dynamics for downwind sails,* in *16th Chesapeake Sailing Yacht Symposium* (2003).

[53] K. Graf and H. Renzsch, *Ranse investigations of downwind sails and integration into sailing yacht design processes,* in *2nd High Performance Yacht Design Conference* (2006).

2

[54] J. Paton, H. Morvan, and P. Heppel, *Fluid structure interaction of yacht sails,* in *International Conference on Innovation in High Performance Sailing Yachts* (2008).

[55] V. G. Chapin, N. de Carlan, and P. Heppel, *Performance optimization of interacting sails through fluid structure coupling,* in *The Second Interantional Conference on Innovation in High Performance Sailing Yachts* (2010).

[56] M. Lombardi, N. Parolini, A. Quarteroni, and G. Rozza, *Numerical simulation of sailing boats: Dynamics, fsi, and shape optimization,* in *Variational Analysis and Aerospace Engineering: Mathematical Challenges for Aerospace Design,* Springer Optimization and Its Applications, edited by G. Buttazzo and A. Frediani (Springer US, 2012) pp. 339–377.

[57] M. Durand, A. Leroyer, C. Lothodé, F. Hauville, M. Visonneau, R. Floch, and L. Guillaume, *{FSI} investigation on stability of downwind sails with an automatic dynamic trimming,* Ocean Engineering **90**, 129 (2014), innovation in High Performance Sailing Yachts - {INNOVSAIL}.

[58] D. Trimarchi, S. Turnock, D. J. Taunton, and D. Chapelle, *The use of shell elements to capture sail wrinkles, and their influence on aerodynamic loads,* in *2nd International Conference on Innovation in High Performance Sailing Yachts* (2010).

[59] H. Renzsch, O. Müller, and K. Graf, *Flexsail - a fluid structure interaction program for the investigation of spinnakers,* in *International Conference on Innovation in High Performance Sailing Yachts* (2008).

[60] H. Renzsch and K. Graf, *Fluid structure interaction simulation of spinnakers - getting closer to reality,* in *2nd International Conference on Innovation in High Performance Sailing Yachts* (2010).

[61] H. Renzsch and K. Graf, *Fluid structure interaction simulation of spinnakers - towards simulation driven sail design,* in *21st International HISWA Symposium on Yacht Design and Yacht Construction* (2010).

[62] H. Renzsch and K. Graf, *Fluid structure interaction simulations of spinnakers; getting closer to reality,* International Journal of Small Craft Technology, The Transactions of The Royal Institution of Naval Architects, Part B2 **153**, 71 (2011).

3

STRUCTURAL SIMULATION THEORY

To calculate the structural behaviour of the sail a Finite Element approach is used. This means that the sail is discretised into small elements for which the structural behaviour can easily be computed. Due to the nature of discretising this approach always remains an approximation of the real behaviour, yet, by making the elements small enough, a satisfactory representation of the real behaviour can be achieved.

3.1. FINITE ELEMENT MODELLING

In published finite element theory several approaches to the modelling of thin, essentially two-dimensional, materials are given; membrane, plate and shell elements. A membrane element is characterised by having two degrees of freedom per node, the in-plane displacements. Plate elements, based on Kirchhoff's plate theory have three degrees of freedom per node, the out of plane displacement and rotation about two perpendicular axes lying within the elements plane. Shell elements have six degrees of freedom per node; displacement in and rotation about all three axes of a Cartesian coordinate system. Typically the rotation about an axis normal to the element's plane is omitted reducing it to five degrees per node. Due to their characteristics membrane and shell elements are particularly suited to the modelling of sails and similar structures as plate elements are not capable of capturing the in-plane stresses. When using membrane elements it is assumed that the material's bending stiffness has no noteworthy influence on the structure's behaviour. The shell element takes all these effects into account, however, when bending stiffness is approaching zero, it effectively becomes a membrane element.

3.1.1. FEM NOMENCLATURE

To properly describe the behaviour of the finite elements used in the simulations a particular nomenclature is required, differentiating between undeformed as well as deformed element states and world, element and material coordinate systems.

Lower case italics indicate scalar values, lower case bold a vector and upper case bold a matrix.

Roman letters:

x   location of node
u   displacement of node
H   Hessian matrix
T   transformation matrix
C   transformation matrix triangular element
c   cosine
s   sine

Greek letters:

α corner angle
ε strain
ϕ potential energy
φ strain energy density
σ stress
θ angle between two two-dimensional coordinate systems

Symbols and subscripts:

ˆ   material coordinate system
ˉ   element coordinate system
˜   coordinate system aligned with principal stresses respectively wrinkling direction
$_i$ node i
$_j$ edge j
$_{xx}$ stress or strain in world coordinate x
$_{yy}$ stress or strain in world coordinate y
$_{xy}$ shear stress or strain in world coordinates

3.1.2. The CST Element

For the modelling of the sail *Constant Stress Triangle (CST)* elements are used. These elements were first described by *Zienkiewicz* in 1971 [1]. These triangular elements are characterised by assuming that

a) The individual stress components are constant over the whole element
b) The stress-strain relationship is linear
c) The strains are only dependent on the element's in-plane deformations.

Based on these assumptions the degrees of freedom of a singular element can be reduced to the relative in-plane displacement of the three nodes forming the element with the initial location of a node *i* being given as $\bar{\mathbf{x}}_i$ and its displacement as $\bar{\mathbf{u}}_i$.

In total, the following formulae are based on four coordinate systems:

• A three-dimensional cartesian "global" coordinate system (x, y, z) which is constant for the entire structure. Within this coordinate system each node has three translational degrees of freedom.

- A two-dimensional cartesian element coordinate system given by $(\bar{x}, \bar{y})$. This co-ordinate system exists per element and lies in the element plane. Within this co-ordinate system each node has two translational degrees of freedom. Any nodal displacement normal to the element plane leads to a re-orientation of the coordinate system versus the global coordinate system.

- A two-dimensional cartesian material coordinate system given by $(\hat{x}, \hat{y})$. This co-ordinate system lies in the element plane as well and aligned with the materials principal axes.

- A fictitious two-dimensional cartesian wrinkled coordinate system given by $(\tilde{x}, \tilde{y})$, see Section 3.1.3.

Starting with an arbitrary two-dimensional cartesian coordinate system (x, y), the generalised stress-strain relationship can be written as

$$\boldsymbol{\sigma} = \mathbf{H}\boldsymbol{\varepsilon}, \tag{3.1}$$

with the Hessian matrix $\mathbf{H}$ being the partial derivative of the stress by the strain components:

$$\mathbf{H} = \begin{bmatrix} \frac{\partial \sigma_{xx}}{\partial \varepsilon_{xx}} & \frac{\partial \sigma_{xx}}{\partial \varepsilon_{xx}} & \frac{\partial \sigma_{xx}}{\partial \varepsilon_{xy}} \\ \frac{\partial \sigma_{yy}}{\partial \varepsilon_{xx}} & \frac{\partial \sigma_{yy}}{\partial \varepsilon_{yy}} & \frac{\partial \sigma_{yy}}{\partial \varepsilon_{xy}} \\ \frac{\partial \sigma_{xy}}{\partial \varepsilon_{xx}} & \frac{\partial \sigma_{xy}}{\partial \varepsilon_{yy}} & \frac{\partial \sigma_{xy}}{\partial \varepsilon_{xy}} \end{bmatrix}. \tag{3.2}$$

Usually this Hessian or stiffness matrix is given in the material oriented coordinate system, e.g. for woven orthotropic fabrics aligned with warp and fill direction, see Figure 3.1.
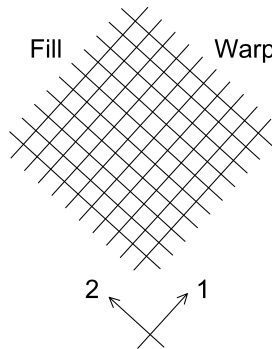

Figure 3.1: Typical material oriented coordinate system for orthotropic material.

For the finite element simulation, the sail's surface will be discretised using triangular elements as shown in Figure 3.2. Please note that side 3 is parallel to the x-axis of an element coordinate system $(\bar{x}, \bar{y})$. This does not induce any loss of generality but simplifies the following derivations.
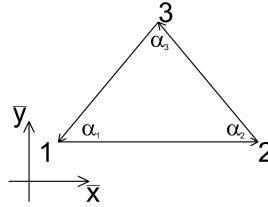
Figure 3.2: Triangular element in element coordinate system.

3

As the finite elements each have their own element oriented coordinate system (see Figure 3.2), first the material oriented stress-strain relationship has to be transformed into the element oriented coordinate system. The following derivation closely follows the procedure outlined by *Arcaro* [2].

In an arbitrary two-dimensional cartesian coordinate system (x, y), the strain in an infinitesimal line segment in direction of a unit vector **v** (see Figure 3.3) can be written as

$$\varepsilon_{\mathbf{v}} = c_i^2 \varepsilon_{\bar{x}\bar{x}} + s_i^2 \varepsilon_{\bar{y}\bar{y}} + 2 c_i s_i \varepsilon_{\bar{x}\bar{y}}, \tag{3.3}$$

with $\mathbf{v} = \begin{bmatrix} c \\ s \end{bmatrix}$, $c = \cos\theta$ and $s = \sin\theta$, θ as given in Figure 3.3.
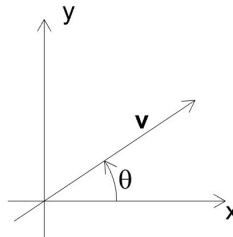

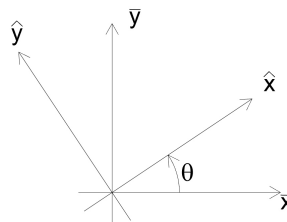Figure 3.3: Unit vector **v** in coordinate system (x, y).

Figure 3.4: Relation between material $(\hat{x}, \hat{y})$ and element $(\bar{x}, \bar{y})$ coordinate systems.

Applying (3.3) to the situation given in Figure 3.4 yields the following transformations

of strain and stress:

$$\begin{bmatrix} \varepsilon_{\hat{x}\hat{x}} \\ \varepsilon_{\hat{y}\hat{y}} \\ \varepsilon_{\hat{x}\hat{y}} \end{bmatrix} = \begin{bmatrix} c^2 & s^2 & 2cs \\ s^2 & c^2 & -2cs \\ -cs & cs & (c^2-s^2) \end{bmatrix} \begin{bmatrix} \varepsilon_{\bar{x}\bar{x}} \\ \varepsilon_{\bar{y}\bar{y}} \\ \varepsilon_{\bar{x}\bar{y}} \end{bmatrix} \Rightarrow \hat{\boldsymbol{\varepsilon}} = \mathbf{T}\bar{\boldsymbol{\varepsilon}}, \tag{3.4}$$

$$\begin{bmatrix} \sigma_{\hat{x}\hat{x}} \\ \sigma_{\hat{y}\hat{y}} \\ \sigma_{\hat{x}\hat{y}} \end{bmatrix} = \begin{bmatrix} c^2 & s^2 & 2cs \\ s^2 & c^2 & -2cs \\ -cs & cs & (c^2-s^2) \end{bmatrix} \begin{bmatrix} \sigma_{\bar{x}\bar{x}} \\ \sigma_{\bar{y}\bar{y}} \\ \sigma_{\bar{x}\bar{y}} \end{bmatrix} \Rightarrow \hat{\boldsymbol{\sigma}} = \mathbf{T}\bar{\boldsymbol{\sigma}}. \tag{3.5}$$

For numerical convenience the formulae are manipulated as follows:

$$\hat{\boldsymbol{\varepsilon}} = \begin{bmatrix} \varepsilon_{\hat{x}\hat{x}} \\ \varepsilon_{\hat{y}\hat{y}} \\ \sqrt{2}\varepsilon_{\hat{x}\hat{y}} \end{bmatrix}, \bar{\boldsymbol{\varepsilon}} = \begin{bmatrix} \varepsilon_{\bar{x}\bar{x}} \\ \varepsilon_{\bar{y}\bar{y}} \\ \sqrt{2}\varepsilon_{\bar{x}\bar{y}} \end{bmatrix},$$

$$\hat{\boldsymbol{\sigma}} = \begin{bmatrix} \sigma_{\hat{x}\hat{x}} \\ \sigma_{\hat{y}\hat{y}} \\ \sqrt{2}\sigma_{\hat{x}\hat{y}} \end{bmatrix}, \bar{\boldsymbol{\sigma}} = \begin{bmatrix} \sigma_{\bar{x}\bar{x}} \\ \sigma_{\bar{y}\bar{y}} \\ \sqrt{2}\sigma_{\bar{x}\bar{y}} \end{bmatrix},$$

$$\mathbf{T} = \begin{bmatrix} c^2 & s^2 & \sqrt{2}cs \\ s^2 & c^2 & -\sqrt{2}cs \\ -\sqrt{2}cs & \sqrt{2}cs & (c^2-s^2) \end{bmatrix},$$

$$c = \cos\theta, s = \sin\theta .$$

Therefore in a material coordinate system (3.1) can be written as:

$$\hat{\boldsymbol{\sigma}} = \hat{\mathbf{H}}\hat{\boldsymbol{\varepsilon}}, \tag{3.6}$$

as well as in an element coordinate system:

$$\bar{\boldsymbol{\sigma}} = \bar{\mathbf{H}}\bar{\boldsymbol{\varepsilon}}. \tag{3.7}$$

Given that $\mathbf{T}\mathbf{T}^T = \mathbf{I}$ or $\mathbf{T}^T = \mathbf{T}^{-1}$ respectively, applying (3.4) and (3.5) to (3.1) yields the following for the stress - strain relationship in an element coordinate system:

$$\bar{\boldsymbol{\sigma}} = \mathbf{T}^T\hat{\mathbf{H}}\mathbf{T}\bar{\boldsymbol{\varepsilon}}, \tag{3.8}$$

and

$$\bar{\mathbf{H}} = \mathbf{T}^T\hat{\mathbf{H}}\mathbf{T}. \tag{3.9}$$

As stated above, the aim of applying the above described stress-strain relationship to a discrete finite element is to obtain an equation for nodal forces as a function of nodal displacements. To this end we have to describe strain as a function of these nodal displacements and compute the resulting stress from these. Typically this is done using so-called shape functions, these give a direct relation between nodal displacements and strain in the element coordinate system. This relation has to be transformed to a global coordinate system based on the elements current orientation at each step of the solution.

As the elongation and resulting strain in the elements edges can easily be calculated in element as well as global coordinate system from relative node displacements without

transformation between these coordinate systems, a formulation for strains based on edge elongations is derived.

In Figure 3.2 the following geometrical relationships can be observed:

$$
\begin{aligned}
\theta_1 + \alpha_2 = \pi &\Rightarrow \begin{cases} c_1 = -\cos\alpha_2 \\ s_1 = +\sin\alpha_2 \end{cases} \\
\theta_2 = \alpha_1 + \pi &\Rightarrow \begin{cases} c_2 = -\cos\alpha_1 \\ s_2 = -\sin\alpha_1 \end{cases}
\end{aligned}
\tag{3.10}
$$

with θ_1 and θ_2 being the rotation of edges 1 and 2 against the $\bar{x}$-axis (keeping in mind that edge 3 is parallel to $\bar{x}$).

Using these relations in (3.3) for each edge j ($j = 1$ to 3) yields the strains ε_j:

$$
\begin{bmatrix} \varepsilon_1 \\ \varepsilon_2 \\ \varepsilon_3 \end{bmatrix} = \begin{bmatrix} \cos^2\alpha_2 & \sin^2\alpha_2 & -\sqrt{2}\cos\alpha_2\sin\alpha_2 \\ \cos^2\alpha_1 & \sin^2\alpha_1 & +\sqrt{2}\cos\alpha_1\sin\alpha_1 \\ 1 & 0 & 0 \end{bmatrix} \begin{bmatrix} \varepsilon_{\bar{x}\bar{x}} \\ \varepsilon_{\bar{y}\bar{y}} \\ \sqrt{2}\varepsilon_{\bar{x}\bar{y}} \end{bmatrix} \Rightarrow \boldsymbol{\varepsilon} = \mathbf{C}\bar{\boldsymbol{\varepsilon}},
\tag{3.11}
$$

with

$$
\boldsymbol{\varepsilon} = \begin{bmatrix} \varepsilon_1 \\ \varepsilon_2 \\ \varepsilon_3 \end{bmatrix}, \mathbf{C} = \begin{bmatrix} \cos^2\alpha_2 & \sin^2\alpha_2 & -\sqrt{2}\cos\alpha_2\sin\alpha_2 \\ \cos^2\alpha_1 & \sin^2\alpha_1 & +\sqrt{2}\cos\alpha_1\sin\alpha_1 \\ 1 & 0 & 0 \end{bmatrix} \ .
$$

It can be shown that the determinant $|\mathbf{C}|$ is given by

$$
|\mathbf{C}| = \sqrt{2}\sin\alpha_1\sin\alpha_2\sin\alpha_3 ,
\tag{3.12}
$$

and the inverse $\mathbf{C}^{-1}$ by

$$
\mathbf{C}^{-1} = \frac{1}{|\mathbf{C}|} \begin{bmatrix} 0 & 0 & \sqrt{2}\sin\alpha_1\sin\alpha_2\sin\alpha_3 \\ \sqrt{2}\cos\alpha_1\sin\alpha_1 & \sqrt{2}\cos\alpha_2\sin\alpha_2 & -\sqrt{2}\sin\alpha_1\sin\alpha_2\sin\alpha_3 \\ -\sin^2\alpha_1 & \sin^2\alpha_2 & \sin(\alpha_1-\alpha_2)\sin\alpha_3 \end{bmatrix} .
\tag{3.13}
$$

The edge strains ε_j, $j = 1, ..., 3$, can as well be computed directly from the nodal displacements $\mathbf{u}_i$. The displacement of the entire element in the global coordinate system by vectors $\mathbf{u}_i$ is show in Figure 3.5, the deformation of a single edge due to displacement in Figure 3.6.

In Figure 3.5 the individual components of the displacement vectors $\mathbf{u}_i$ are defined as follows:

$$
\mathbf{u}_1 = \begin{bmatrix} u_1 \\ u_2 \\ u_3 \end{bmatrix}, \mathbf{u}_2 = \begin{bmatrix} u_4 \\ u_5 \\ u_6 \end{bmatrix}, \mathbf{u}_3 = \begin{bmatrix} u_7 \\ u_8 \\ u_9 \end{bmatrix} \ .
$$

For the purpose of describing the behaviour of a single edge, in Figure 3.6 the undeformed edge is defined by $\lambda\mathbf{e}$, with $\mathbf{e}$ being a unit vector in direction of the undeformed edge and λ the edge's length, the deformed edge by $\mathbf{l}$, and the nodal displacements by $\mathbf{p}$ and $\mathbf{q}$. From these vectors the following relations can be formulated (see [2]):

$$
\lambda\mathbf{e} + \mathbf{q} - \mathbf{l} - \mathbf{p} = \mathbf{0},
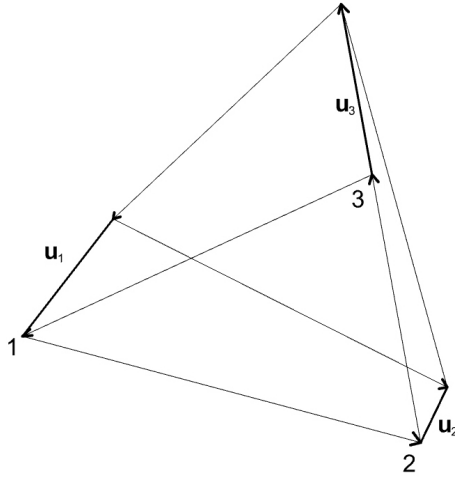\tag{3.14}
$$

Figure 3.5: CST element in undeformed and deformed state with displacement vectors [2]
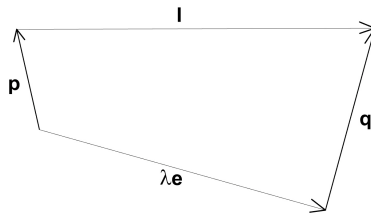

Figure 3.6: Element edge in undeformed and deformed state with displacement vectors [2]

or

$$\mathbf{l} = \lambda \mathbf{e} + \mathbf{q} - \mathbf{p}. \tag{3.15}$$

By defining the normalised deformation of the edge

$$\mathbf{z} = \frac{\mathbf{q} - \mathbf{p}}{\lambda}, \tag{3.16}$$

with $\mathbf{q} - \mathbf{p}$ being the relative displacement of the two nodes describing the edge, and therefore its deformation vector, the vector of the deformed edge $\mathbf{l}$ can be written as

$$\mathbf{l} = \lambda \left(\mathbf{e} + \mathbf{z} \right). \tag{3.17}$$

Squaring the normalised vector of the deformed edge $(\mathbf{e} + \mathbf{z})$ results in

$$1 + \delta = (\mathbf{e} + \mathbf{z})^2 = 1 + 2\mathbf{e}^T \mathbf{z} + \mathbf{z}^T \mathbf{z} \Rightarrow \delta = 2\mathbf{e}^T \mathbf{z} + \mathbf{z}^T \mathbf{z}. \tag{3.18}$$

Then (3.17) gives:

$$|\mathbf{l}|^2 = \mathbf{l}^T \mathbf{l} = \lambda^2 \left(1 + \delta \right). \tag{3.19}$$

Generally, applying the above equations to an edge j of an element, $\mathbf{u}_j$ is the unitary vector parallel to the undeformed edge j and λ_j the corresponding undeformed length.

For the calculation of strain as a function of above deformations, Green's strain definition is used. Generally Green's strain of a material line is defined as

$$\varepsilon_G = \frac{1}{2} \left(\frac{\ell^2 - L^2}{L^2} \right), \tag{3.20}$$

where ε_G is the Green strain, L the original length of the material line and ℓ its deformed length.

Applying (3.19) to the Green strain definition (3.20) results in:

$$\varepsilon_G = \frac{\mathbf{l}^T \mathbf{l} - \lambda^2}{2\lambda^2} = \frac{\delta}{2}. \tag{3.21}$$

Computation of resulting nodal forces as reaction to nodal displacements is based on the concept of potential energy. While external potential energy is calculated as nodal displacement times opposing force

$$\phi_{ext} = -\mathbf{F}^T \mathbf{u}, \tag{3.22}$$

the internal potential energy or potential strain energy resulting from a deformation of an element due to external forces is calculated as the integral of strain energy density over the element's volume:

$$\phi_{int} = \int_v \varphi \, dv = \frac{1}{2} \bar{\boldsymbol{\varepsilon}}^T \bar{\boldsymbol{\sigma}} At, \tag{3.23}$$

with

$$\varphi = \frac{1}{2} \bar{\boldsymbol{\varepsilon}}^T \bar{\boldsymbol{\sigma}}, \tag{3.24}$$

and At being the element's un-deformed volume. As membrane elements are considered, t is assumed to be constant and small. Combining (3.22) and (3.23), the nodal reaction forces resulting from a deformation of an element due to nodal displacements can be calculated as the derivative of the potential strain energy by these displacements.

Applying (3.7), (3.9) and (3.11) yields

$$\varphi = \frac{1}{2} \bar{\boldsymbol{\varepsilon}}^T \bar{\mathbf{H}} \bar{\boldsymbol{\varepsilon}}, \tag{3.25}$$

which expands to

$$\varphi = \frac{1}{2} \boldsymbol{\varepsilon}^T \left(\mathbf{T}\mathbf{C}^{-1}\right)^T \hat{\mathbf{H}} \left(\mathbf{T}\mathbf{C}^{-1}\right) \boldsymbol{\varepsilon} \Rightarrow \varphi = \frac{1}{2} \boldsymbol{\varepsilon}^T \mathbf{H} \boldsymbol{\varepsilon} = \varphi\left(\varepsilon_1, \varepsilon_2, \varepsilon_3\right), \tag{3.26}$$

with

$$\mathbf{H} = \mathbf{C}^{-T} \bar{\mathbf{H}} \mathbf{C}^{-1}, \tag{3.27}$$

and

$$\bar{\mathbf{H}} = \mathbf{T}^T \hat{\mathbf{H}} \mathbf{T}. \tag{3.28}$$

Applying (3.26) to (3.28) to (3.23) yields

$$\phi = \frac{1}{2} \boldsymbol{\varepsilon}^T \left(\mathbf{H}\right) \boldsymbol{\varepsilon} At = \frac{1}{2} \boldsymbol{\varepsilon}^T \left(\mathbf{T}\mathbf{C}^{-1}\right)^T \hat{\mathbf{H}} \left(\mathbf{T}\mathbf{C}^{-1}\right) \boldsymbol{\varepsilon} At. \tag{3.29}$$

Using the edge strains ε_j in (3.23), the gradient of the potential strain energy by a nodal displacement component u_i can be calculated by

$$\phi = \int \varphi\left(\varepsilon_1, \varepsilon_2, \varepsilon_3\right) dv \Rightarrow \frac{\partial \phi}{\partial u_i} = \left(\frac{\partial \varphi}{\partial \varepsilon_1} \frac{\partial \varepsilon_1}{\partial u_i} + \frac{\partial \varphi}{\partial \varepsilon_2} \frac{\partial \varepsilon_2}{\partial u_i} + \frac{\partial \varphi}{\partial \varepsilon_3} \frac{\partial \varepsilon_3}{\partial u_i}\right) At. \tag{3.30}$$

(3.26) can be differentiated by $\boldsymbol{\varepsilon}$ as

$$\varphi = \frac{1}{2} \boldsymbol{\varepsilon}^T \mathbf{H} \boldsymbol{\varepsilon} \Rightarrow \begin{bmatrix} t\frac{\partial \varphi}{\partial \varepsilon_1} \\ t\frac{\partial \varphi}{\partial \varepsilon_2} \\ t\frac{\partial \varphi}{\partial \varepsilon_3} \end{bmatrix} = \left(\mathbf{H}t\right) \boldsymbol{\varepsilon}. \tag{3.31}$$

Then (3.1) yields

$$\boldsymbol{\sigma} t = \left(\mathbf{H}t\right) \boldsymbol{\varepsilon}. \tag{3.32}$$

The gradient of the potential strain energy can be written as

$$\frac{\partial \phi}{\partial u_i} = \left(\boldsymbol{\sigma}^T \frac{\partial \boldsymbol{\varepsilon}}{\partial u_i}\right) At. \tag{3.33}$$

Differentiating the edge strains ε_j with respect to the components k of displacement vectors $\mathbf{p}$ and $\mathbf{q}$ (see Figure 3.6) gives

$$\begin{aligned} \frac{\partial \varepsilon_j}{\partial p_k} &= -\frac{1}{\lambda} \left(e_k + z_k\right), \\ \frac{\partial \varepsilon_j}{\partial q_k} &= +\frac{1}{\lambda} \left(e_k + z_k\right). \end{aligned} \tag{3.34}$$

For each individual edge j the above equations are:

$$\mathbf{z}_1 = \frac{\mathbf{u}_3 - \mathbf{u}_2}{\lambda_1}, \delta_1 = 2\left(\mathbf{e}_1\right)^T \mathbf{z}_1 + \left(\mathbf{z}_1\right)^T \mathbf{z}_1, \varepsilon_1 = \frac{\delta_1}{2}, \nabla\varepsilon_1 = \frac{1}{\lambda_1} \begin{bmatrix} \mathbf{0} \\ -\left(\mathbf{e}_1 + \mathbf{z}_1\right) \\ +\left(\mathbf{e}_1 + \mathbf{z}_1\right) \end{bmatrix},$$

$$\mathbf{z}_2 = \frac{\mathbf{u}_1 - \mathbf{u}_3}{\lambda_2}, \delta_2 = 2\left(\mathbf{e}_2\right)^T \mathbf{z}_2 + \left(\mathbf{z}_2\right)^T \mathbf{z}_2, \varepsilon_2 = \frac{\delta_2}{2}, \nabla\varepsilon_2 = \frac{1}{\lambda_2} \begin{bmatrix} +\left(\mathbf{e}_2 + \mathbf{z}_2\right) \\ \mathbf{0} \\ -\left(\mathbf{e}_2 + \mathbf{z}_2\right) \end{bmatrix}, \quad (3.35)$$

$$\mathbf{z}_3 = \frac{\mathbf{u}_2 - \mathbf{u}_1}{\lambda_3}, \delta_3 = 2\left(\mathbf{e}_3\right)^T \mathbf{z}_3 + \left(\mathbf{z}_3\right)^T \mathbf{z}_3, \varepsilon_3 = \frac{\delta_3}{2}, \nabla\varepsilon_3 = \frac{1}{\lambda_3} \begin{bmatrix} -\left(\mathbf{e}_3 + \mathbf{z}_3\right) \\ +\left(\mathbf{e}_3 + \mathbf{z}_3\right) \\ \mathbf{0} \end{bmatrix}.$$

3.1.3. Membrane Wrinkling Analysis

Basically, for typical simple finite elements the same stress-strain relationship under in plane extension and compression is assumed. The CST element described above is no exception. Unfortunately this does not correctly describe the behaviour of materials like sailcloth which are quite stiff under in plane extension but simply fold under compression. While the resulting geometry of a wrinkled fabric in reality depends on various factors like the (very small) bending stiffness and the actual principal strains, the folds that form due to compression in the simulation of a discretised membrane depend on size and shape of the finite elements as well as the orientation of their edges. These folds are essentially numerical artefacts, not an actual representation of the geometry (*Heppel* [3]). In some cases, depending on grid orientation, long folds can appear in the geometry, effectively inducing bending stiffness into the geometry, a so-called grid-locking effect (*Pitkäranta* [4]).

Typically, in finite element analyses, two different methods are used to include this material non-linearity; either shell elements coupled with a buckling analysis or membrane elements together with a wrinkling model.

Shell elements have at least five degrees of freedom per node to include bending moments into the element equation. This allows to detect the onset of buckling and the buckling mode by performing an eigenvalue analysis of the stiffness matrix. For problems where the material's bending stiffness is of significance to the results this approach is assumed to be the correct one. The onset and mode of wrinkling are highly dependent on the material's bending stiffness and the stress parallel to the wrinkles (*Wong et al.* [5]). Examples of these problems include localised analyses of highly loaded corners and cutouts. Correct computation of the resulting wrinkles requires sufficiently fine resolution of the surface.

For problems where the bending stiffness can be safely assumed to be negligible in the context of the analysis, a simpler approach can be used. If the bending stiffness is set to zero for a shell element and all rows and columns of the stiffness matrix containing only zeros are removed, the shell element reduces to a membrane element, e.g. the CST element. Due to the lack of bending stiffness the eigenvalue analysis would become non-defined and the wrinkling frequency infinite. As for these problems the acute geometrical shape of the wrinkles is typically of no concern to the global solution, the out

of plane displacements due to the wrinkles are disregarded and the system of equations modified in a way that both principle stresses are equal or larger than zero. This happens due to a so-called wrinkling model (*Miller et al., Kang et al., Heppel, Lu et al.* [3, 6–8]). Typical examples of these problems include global analyses of sails, parachutes and tent roofs. Usage of the wrinkling model allows to capture wrinkles smaller than the elements used.

For the purpose of this thesis the CST element, as described in the previous chapter, extended by a wrinkling model, is chosen. Several wrinkling models are presented in literature, based on different approaches (*Miller et al., Liu et al., Kang et al., Lu et al.* [6–9]).

Initial wrinkling models, as presented by *Miller et al.* [6], modified the element stiffness matrix to the extent that stiffness is only present in the direction of the first (larger) principal strain. Due to the condition of principal stresses and strains having to be aligned this approach is limited to isotropic materials. Furthermore, in regions of fully slack cloth, the stiffness matrix may become singular, effectively preventing calculation of a valid solution. A solution to the latter shortcoming was presented by *Liu et al.* [9]. They introduced the concept of a *penalty parameter*. Instead of setting the stiffness in the direction of the second principal stress to zero, it is divided by this penalty parameter, resulting in a very small stiffness, which is still sufficient to ensure numerical stability of the solver.

Kang et al. and *Lu et al.* [7, 8] argued that the modification of the element's stiffness matrix is physically incorrect as the material properties do not change in reality. They introduced a *wrinkling strain*, modifying the element strain until negative principal stresses vanish. For isotropic materials the effect is exactly the same as in the approach given by *Miller et al.* [6]. Due to the non-alignment of principal strains and stresses in anisotropic materials the wrinkling angle in these cases has to be found numerically.

WRINKLING CRITERIA

To define mathematically if wrinkling occurs, a criterion to evaluate the state of the element has to be defined. Generally three states can be observed: taut, slack and wrinkled. Literature (e.g. *Liu et al.* [9]) gives three different criteria defining these states: stress based, strain based and mixed stress-strain criterion. These criteria are as follows:

1. Stress based criterion

    - $\sigma_2 > 0 \Rightarrow$ taut
    - $\sigma_1 \leq 0 \Rightarrow$ slack
    - $\sigma_1 > 0$ and $\sigma_2 \leq 0 \Rightarrow$ wrinkled

2. Strain based criterion

    - $\varepsilon_2 > 0 \Rightarrow$ taut
    - $\varepsilon_1 \leq 0 \Rightarrow$ slack
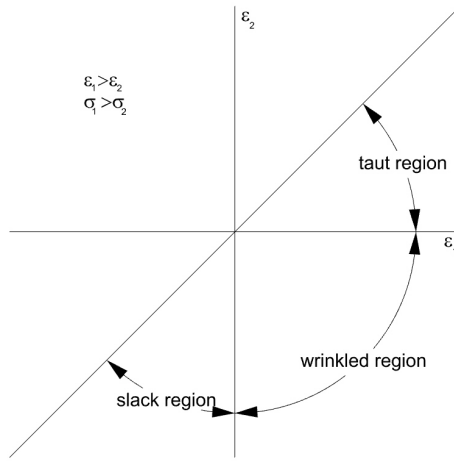   - $\varepsilon_1 > 0$ and $\varepsilon_2 \leq 0 \Rightarrow$ wrinkled

3. Mixed Stress-Strain criterion

- $\sigma_2 > 0 \Rightarrow$ taut
- $\varepsilon_1 \leq 0 \Rightarrow$ slack
- $\varepsilon_1 > 0$ and $\sigma_2 \leq 0 \Rightarrow$ wrinkled

with σ_1, σ_2, $\varepsilon 1$ and $\varepsilon 2$ being the larger respectively smaller of the principal stresses and strains, calculated without application of the wrinkling model.

As, for example, Hooke's law for an isotropic material in two dimensions, aligned with the principal strains, respectively stresses, is given by

$$\begin{bmatrix} \sigma_1 \\ \sigma_2 \end{bmatrix} = \frac{E}{1-v^2} \begin{bmatrix} 1 & v \\ v & 1 \end{bmatrix} \begin{bmatrix} \varepsilon_1 \\ \varepsilon_2 \end{bmatrix}, \tag{3.36}$$

strain and stress in the two principal directions are coupled by the Poisson ratio v. Due to this coupling, the stress resulting from a principal strain close to zero can be significantly affected when the absolute value of the other principal strain is relatively large. This can even lead to a change of sign. These effects are further explained blow.

The effect of these different criteria can be depicted by a Mohr's circles, see Figures 3.7 to 3.9.

Figure 3.7: Mohr's circle for the stress based criterion [9]

As can be derived from Equation (3.36), both criteria based solely on stress or strain have significant shortcomings in the prediction of wrinkling:

1. In cases where ε_1 is slightly larger and ε_2 significantly smaller than zero, Hooke's law without consideration of wrinkling might predict negative values for σ_2 as well as σ_1, while in fact σ_1 would be slightly above zero in the wrinkled membrane. This effect is missed by the stress based criterion which would predict a slack instead of wrinkled membrane in this case.

Figure 3.8: Mohr's circle for the strain based criterion [9]
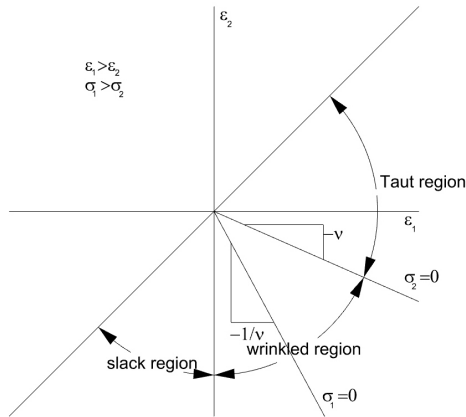
Figure 3.9: Mohr's circle for the mixed criterion [9]

2. Similarly, in cases where ε_1 is significantly larger than zero and ε_2 IS in fact slightly negative, but σ_2 calculated according to Hooke's law would in fact be positive, the strain based criterion would predict a wrinkled instead of taut membrane.

3. The mixed criterion captures the above exceptional cases and represents the most accurate description of the state of the membrane. It is used for the simulations described in this thesis.

WRINKLING MODEL

The description of the numerical model given in this section closely follows the approach given by *Kang et al.* [7].

As stated above, a membrane model is not capable of modelling the actual wrinkled surface. To circumvent this limitation, we define the fictitious non-wrinkled membrane which has a smooth surface, representing the average surface which would be attained after the wrinkles were removed.

Assuming a small element under homogeneous deformation in the state of wrinkling, as shown in Figure 3.10, this element would be in a state of uniaxial tension. In the deformed configuration, the direction of this tension would be perpendicular to the wrinkling direction. Assuming a material point of an element in non-wrinkled configuration κ_0 at the location (x_1, x_2, x_3) in a global coordinate system with x_1 and x_2 being in the material plane and x_3 perpendicular to it, the same point in a wrinkled configuration κ_w has the global coordinates (X_1, X_2, X_3). Further, by defining a local reference frame $(\tilde{x}_1, \tilde{x}_2)$ on the element in κ_0 in a way that the $\tilde{x}_1$-axis is aligned with the direction of uniaxial tension in κ_w, $\tilde{x}_2$ being perpendicular to $\tilde{x}_1$ is aligned with the wrinkling direction. The axis $\tilde{X}_1$ of the corresponding coordinate system $(\tilde{X}_1, \tilde{X}_2)$ in state κ_w is aligned with the direction of uniaxial tension as well. Similarly, a material line element aligned with $\tilde{x}_1$ in κ_0 is aligned with $\tilde{X}_1$ in κ_w. However, a material line element aligned with $\tilde{x}_2$ in κ_0, is only aligned with $\tilde{X}_2$ in κ_w, if all shear strain with respect to $(\tilde{x}_1, \tilde{x}_2)$ in κ_0 vanishes.

Defining $\mathbf{e}_i$, $\mathbf{E}_i$, $\tilde{\mathbf{e}}_i$ and $\tilde{\mathbf{E}}_i$ as the base vectors along x_i, X_i, $\tilde{x}_i$ and $\tilde{X}_i$ respectively, under the assumption of small strain, the stress-strain relationship in reference frame $(\tilde{x}_1, \tilde{x}_2)$ can be written as

$$\sigma^{IJ} = \mathbf{C}^{IJKL}\varepsilon_{KL}, \tag{3.37}$$

with the stress σ^{IJ}, the strain ε_{KL} and the stiffness matrix $\mathbf{C}^{IJKL}$.

Assuming a membrane element ABCD in state κ_0 is deformed to shape A"B"C"D" in state κ_w, this deformation can be seen as a sequence of several individual deformations. First we define rigid rotation from ABCD to $\bar{A}\bar{B}\bar{C}\bar{D}$. Next follows the deformation by uniaxial tension from $\bar{A}\bar{B}\bar{C}\bar{D}$ to A'B'C'D'. Last is the pure wrinkling deformation from A'B'C'D' to A"B"C"D". To distinguish the state of uniaxial tension without wrinkling (A'B'C'D') from the state of uniaxial tension where wrinkling may occur (A"B"C"D"), (A'B'C'D') will from here on be called the state of *natural uniaxial tension*. A"B"C"D" is the genuine final state of uniaxial tension in the presence of wrinkling. In Figure 3.10 the initial and final states ABCD and A"B"C"D" are shown as well as the fictitious non-wrinkled membrane replacing the wrinkled one.
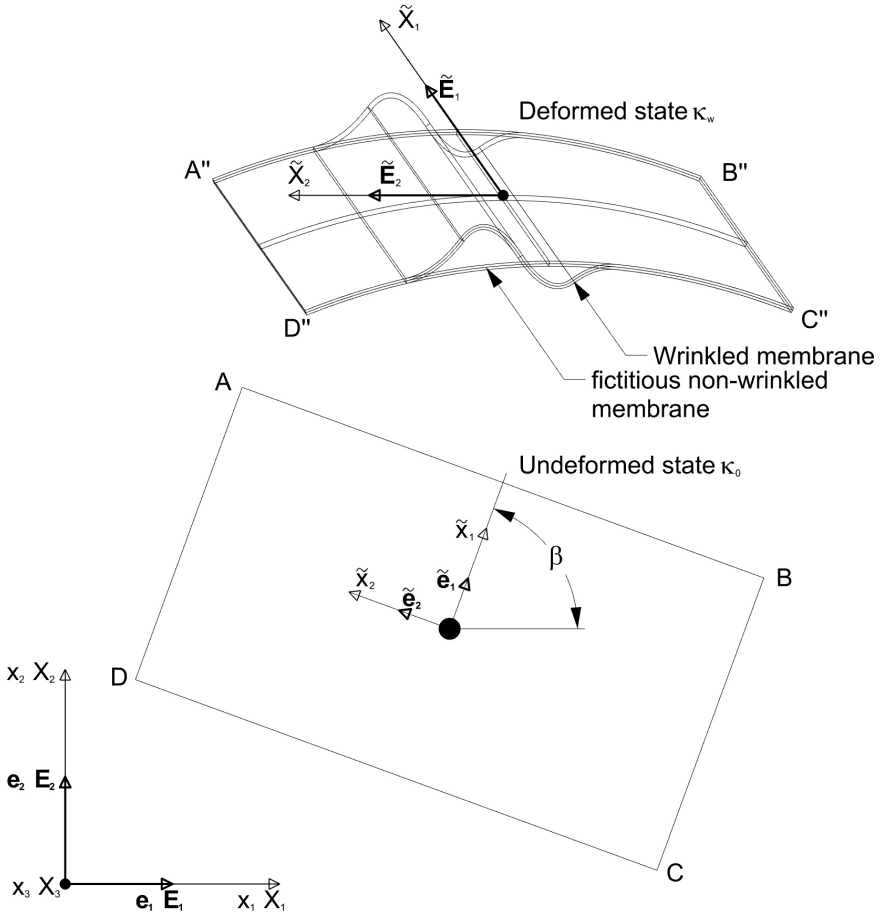
Figure 3.10: Coordinate systems for undeformed and wrinkled membrane states as well as fictitious non-wrinkled membrane.

From the collapsed representation of 3.37

$$
\begin{bmatrix} \tilde{\sigma}_{11} \\ \tilde{\sigma}_{22} \\ \sqrt{2}\tilde{\sigma}_{12} \end{bmatrix} = \begin{bmatrix} \tilde{C}_{11} & \tilde{C}_{12} & \sqrt{2}\tilde{C}_{13} \\ \tilde{C}_{21} & \tilde{C}_{22} & \sqrt{2}\tilde{C}_{23} \\ \sqrt{2}\tilde{C}_{31} & \sqrt{2}\tilde{C}_{32} & \tilde{C}_{33} \end{bmatrix} \cdot \begin{bmatrix} \tilde{\varepsilon}_{11} \\ \tilde{\varepsilon}_{22} \\ \sqrt{2}\tilde{\varepsilon}_{12} \end{bmatrix} , \tag{3.38}
$$

with $\tilde{C}_{IJ}$ being the stiffness matrix in the $\tilde{x}$ frame, it is important to note that, due to the uniaxial nature of the stress in the wrinkled membrane element, $\tilde{\sigma}_{22} = \tilde{\sigma}_{12} = 0$. Applying this condition and solving for $\tilde{\varepsilon}_{11}$ yields:

$$
\tilde{\sigma}_{11} = a \cdot \tilde{\varepsilon}_{11} , \tag{3.39}
$$

with

$$
\begin{aligned}
a = \frac{1}{\tilde{C}_{23}\tilde{C}_{32} - \tilde{C}_{22}\tilde{C}_{33}} &\left[\tilde{C}_{11} \left(\tilde{C}_{23}\tilde{C}_{32} - \tilde{C}_{22}\tilde{C}_{33} \right) \right. \\
&\left. + \tilde{C}_{12} \left(\tilde{C}_{21}\tilde{C}_{33} - \tilde{C}_{23}\tilde{C}_{31} \right) + \tilde{C}_{13} \left(\tilde{C}_{31}\tilde{C}_{22} - \tilde{C}_{21}\tilde{C}_{32} \right) \right] .
\end{aligned} \tag{3.40}
$$

As flexural stiffness of the membrane element is assumed to be neglegible, inducing wrinkling from state A'B'C'D' to A"B"C"D" does not change the stresses within the membrane element. Therefore the stress-strain relationship given in (3.39) remains valid for the state of *uniaxial tension* under the occurance of wrinkling A"B"C"D" as well as the state of *natural uniaxial tension* A'B'C'D'.

Similarly, inserting the condition for *natural uniaxial tension* - $\tilde{\varepsilon}'_{22}$ and $\tilde{\varepsilon}'_{12}$ giving exactly slack state normal to $\tilde{\varepsilon}'_{11}$, but no wrinkling - together with (3.39) into (3.38):

$$
\tilde{\varepsilon}'_{22} = \frac{\tilde{C}_{21}\tilde{C}_{33} - \tilde{C}_{23}\tilde{C}_{31}}{\tilde{C}_{23}\tilde{C}_{31} - \tilde{C}_{22}\tilde{C}_{33}} \tilde{\varepsilon}'_{11} , \tag{3.41}
$$

and

$$
\sqrt{2}\tilde{\varepsilon}'_{12} = \frac{\tilde{C}_{22}\tilde{C}_{31} - \tilde{C}_{21}\tilde{C}_{32}}{\tilde{C}_{23}\tilde{C}_{31} - \tilde{C}_{22}\tilde{C}_{33}} \tilde{\varepsilon}'_{11} . \tag{3.42}
$$

By *Kang et al.* [7] it is shown for the purely wrinkling deformation from A'B'C'D' to A"B"C"D" that

$$
\tilde{\varepsilon}'_{11} = \tilde{\varepsilon}''_{11} \text{ and } \tilde{\varepsilon}'_{12} = \tilde{\varepsilon}''_{12} \text{ but } \tilde{\varepsilon}'_{22} \neq \tilde{\varepsilon}''_{22} . \tag{3.43}
$$

Therefore from (3.42) it follows that

$$
\sqrt{2}\tilde{\varepsilon}''_{12} = \frac{\tilde{C}_{22}\tilde{C}_{31} - \tilde{C}_{21}\tilde{C}_{32}}{\tilde{C}_{23}\tilde{C}_{31} - \tilde{C}_{22}\tilde{C}_{33}} \tilde{\varepsilon}''_{11} , \tag{3.44}
$$

(3.43) implies that (3.42) respectively (3.44) remain valid regardless of the amount of wrinkling. Therefore (3.42) and (3.44) are invariant to the magnitude of wrinkling and valid for the wrinkled state as well as the state of natural uniaxial tension, while (3.41) is only valid in the state of natural uniaxial tension.

From the above formulae and observations the direction of the uniaxial tension can be determined. This direction is coincident with the $\tilde{x}_1$ axis in Figure 3.10. Note that $\tilde{\varepsilon}_{11}$ is the strain component along this axis in case of wrinkling. The angle of rotation between x_1 and $\tilde{x}_1$ β can be found as follows:

1. Assume an angle β^*

2. Transform the strain components ε_{ij} to the components ε_{ij}^* in the x_1^* frame by rotation from x_1 by β^*

3. Check whether $\varepsilon_{11}^* > 0$

4. If $\varepsilon_{11}^* > 0$, set $\tilde{\varepsilon}_{11} = \varepsilon_{11}^*$

5. Calculate $\tilde{\varepsilon}_{22}$ and $\tilde{\varepsilon}_{12}$ from $\tilde{\varepsilon}_{11}$ using (3.41) and (3.42)

6. Find $\beta = \beta^*$ such that $\tilde{\varepsilon}_{12} = \varepsilon_{12}^*$ and $\tilde{\varepsilon}_{22} \geq \varepsilon_{22}^*$

Due to symmetry we need to find β only for $0 \leq \beta < \pi$. Key is finding the root of the equation $f(\beta) = \tilde{\varepsilon}_{12} - \varepsilon_{12}^*$, where β is implicit, by a numerical method.

To find above root, Ridder's method [10, 11] - a combination of *Regula Falsi* and approximation by an exponential function - has been chosen. The advantage of this method above other - possibly more efficient - approaches lies in the fact that convergence even for not well-behaved functions is guaranteed due to the bracketing inherent to the *Regual Falsi*. For well-behaved functions, the rapid convergence ($m = 2^{0.5}$) due to the approximation of the function using exponential factors is realised.

When the conditions relevant for the chosen wrinkling criterion (Section 3.1.3, stress, strain or mixed criterion) are satisfied, there exists only one solution for β. The wrinkling strain $\varepsilon_w = \tilde{\varepsilon}_{22} - \varepsilon_{22}^*$ is a measure of the amount of wrinkling. In the wrinkled state, ε_w is always larger than zero.

3.2. SOLUTION OF SYSTEM OF EQUATIONS

The equations given above describe the stiffness matrix for a singular element. Classically in finite element analysis these individual element stiffness matrices are assembled to a global stiffness matrix, inverted and with the external forces solved for the nodal displacements. Unfortunately this approach does not work for the membrane equations given above for the following reasons:

1. Due to calculating only in-plane forces from the membrane stresses, the structure is not statically defined in the non-stressed state.

2. The geometrical as well as material behaviour of the structure is highly non-linear

These two peculiarities introduce the following requirements: An alternative to the classic stiffness matrix determined solely by the element properties has to be found. The method has to be iterative by nature to approximate the non-linear behaviour by small linearised steps.

Some examples for approaches fulfilling these requirements are:

- Finding a criterion for the solution different from force equilibrium (*Arcaro* [2]). A typical criterion would be the minimisation of the total potential energy of the system. The total potential energy is the sum of the element stresses times strains less the sum of external nodal forces times nodal displacements. This approach lends itself to a Newton type solution as well. Of particular elegance is the possibility to solve without the need for a global stiffness matrix.

- Modelling the structure as a pseudo-dynamic system (*Barnes* [12]). In this approach virtual masses are allocated to the nodes. These masses undergo acceleration due to the differential of external and internal nodal forces. To enable convergence measures to dampen the nodal motions are introduced. This approach is used quite regularly for highly non-linear FE solutions(e.g. ANSYS LS-Dyna, RELAX [3]) and works without a global stiffness matrix as well. Nodal velocities and displacements are obtained by integration over time using appropriate integrations schemes.

- Introducing artificial springs at each node at the beginning of the solution process (*Heppel et al.* [13]). With increasing external loads during the progress of the solution, as the system described by the membrane elements becomes stable in itself due to stress-stiffening, the stiffness of the springs is gradually reduced to zero. This approach lends itself to a Newton or implicit solution approach.

During the development of the program the first and second of the approaches mentioned above were implemented and will be described in more detail below.

3.2.1. MINIMISATION OF TOTAL POTENTIAL ENERGY

The first approach mentioned above is based on the minimisation of potential energy. To this end two different sources of pontential energy need to be defined: *External* potential energy as calculated by a displacement times an opposing force:

$$\phi_{ext} = -\mathbf{F}^T\mathbf{u}, \tag{3.45}$$

and *internal* potential energy or potential strain energy contained within an deformed element, as described in Section 3.1.2. This is calculated as the integral of strain energy density over element volume:

$$\begin{aligned}\phi_{int} &= \int_V \varphi dv \\ &= \int_V \left(\frac{1}{2}\varepsilon \cdot \sigma\right) dv.\end{aligned} \tag{3.46}$$

(3.45) and (3.46) indicate that, when an element is deformed by an external force, yielding to this force and simultaneously increasing stress and strain, the external potential energy is reduced while the internal potential energy increases. Equilibrium for a system is found at the minimum of the total potential energy of the entire system

$$\phi_{total} = \sum_{elements} \phi_{int} - \sum_{nodes} \mathbf{F}^T\mathbf{u}. \tag{3.47}$$

To solve this system, it is necessary to calculate the gradient of total potential energy by the individual nodal displacement components:

$$\nabla\phi_{total} = \sum_{elements} \nabla\phi_{int} - \sum_{nodes} \mathbf{F}. \tag{3.48}$$

Based on (3.47) and (3.48) the system can be solved e.g. by using a Newton method.

While providing an elegant approach to the solution of the present system of equations, it was not possible to obtain stable solutions by minimisation of potential energy when including a wrinkling model. Most probably, this is caused by lack of a well defined gradient of potential energy in wrinkled or slack areas of the membrane structure.

3.2.2. DYNAMIC RELAXATION WITH KINETIC DAMPING

The second approach mentioned above is called *Dynamic Relaxation.* In this approach the structure is modelled as a pseudo-dynamic system, oscillating around the nodal equilibrium positions. To obtain a static solution this oscillation has to be dampened. Typically two different methods are used to this end:

Viscous Damping An artificial viscosity is introduced, mimicking a damped spring-mass system.

Kinetic Damping The total kinetic energy of all nodes is traced. If a peak is detected, all motions are stopped, then the nodes are released again.

In the program kinetic damping is used, the following description closely follows the one given by *Barnes* [12].

The idea behind the method of dynamic relaxation is based on Newton's second law of motion:

$$\mathbf{R}_i(t) = m_i \cdot \ddot{\mathbf{u}}_i(t), \tag{3.49}$$

where $\mathbf{R}_i(t)$ is the total force (sum of internal and external) acting on node i at time t, m_i is the nodes virtual mass and $\ddot{\mathbf{u}}_i(t)$ is the resulting acceleration. As a static equilibrium ($\ddot{\mathbf{u}}_i(t_{end}) = \mathbf{0}$) and not an accurate description of dynamic behaviour is sought, the virtual masses are calculated to ensure fast and stable convergence.

(3.49) is solved for all nodes i in the structure by explicitly integrating time by centred finite differences. The acceleration term $\ddot{\mathbf{u}}_i(t)$ can then be written as:

$$\ddot{\mathbf{u}}_i(t) = \frac{\dot{\mathbf{u}}_i(t + \Delta t/2) - \dot{\mathbf{u}}_i(t - \Delta t/2)}{\Delta t}. \tag{3.50}$$

Similarly the geometry at time $t + \Delta t/2$ can be written as:

$$\mathbf{u}_i(t + \Delta t) = \mathbf{u}_i(t) + \Delta t \cdot \dot{\mathbf{u}}_i(t + \Delta t/2). \tag{3.51}$$

Substituting (3.50) into (3.49) yields the following equation for the velocities at time $t + \Delta t/2$:

$$\dot{\mathbf{u}}_i(t + \Delta t/2) = \dot{\mathbf{u}}_i(t - \Delta t/2) + \frac{\mathbf{R}_i(t)}{m_i} \Delta t \tag{3.52}$$

The explicit update of the nodes' velocities and displacements is calculated without the need for a global stiffness matrix. Actually the updated velocity of a node only depends on the previous velocity and residual force acting on it. Therefore it is not influenced by the current ($t + \Delta t/2$) updates of the other nodes. Resulting from the updated nodal locations at time $t + \Delta t$, the residual forces acting on the nodes are updated:

$$\mathbf{R}_i(t + \Delta t) = \mathbf{F}_{i,ext}(t + \Delta t) + \sum \mathbf{F}_{i,int}(t + \Delta t), \tag{3.53}$$

with $\sum \mathbf{F}_{i,int}$ being the sum of all forces acting on node i by elements connected to node i. $\mathbf{F}_{i,ext}$ is the external force acting on node i, e.g. due to pressure.

The solution is found by iterating until the residual forces are smaller than a given tolerance. The iteration scheme can be summarised as follows:

1. Set all nodal velocity components and the respective kinetic energies to zero

2. Compute external forces acting on nodes

3. Compute internal forces acting on nodes

4. Sum external and internal nodal forces to residuals

5. Reset residuals affecting nodal constraints to zero to enforce these contraints

6. Calculate nodal velocities and positions using (3.51) and (3.52). Determine the sum of kinetic energy (KE) for the entire system at $t + \Delta t/2$

7. If current KE is greater then at $t - \Delta t/2$, return to stage 3

8. If current KE is smaller then at $t - \Delta t/2$, compute small corrections to nodal positions to correctly capture the kinetic energy peak

9. Return to stage 1 and repeat entire process until residuals are sufficiently small

At the beginning of the solving process or after reinitialisation the velocities $\dot{\mathbf{u}}_i(-\Delta t/2)$ as required in (3.52) are unknown. Therefore it is assumed that
$\dot{\mathbf{u}}_i(-\Delta t/2) = -\dot{\mathbf{u}}_i(\Delta t/2)$
which is equivalent to $\dot{\mathbf{u}}_i(0) = 0$. This yields:

$$\dot{\mathbf{u}}_i(\Delta t/2) = \frac{\mathbf{R}_i(0)}{2m_i} \Delta t. \tag{3.54}$$

At stage 8 the nodal positions are supposed to be corrected to the time of the kinetic energy peak, t^*. As shown in Figure 3.11, a quadratic approximation can be fitted through the current value of KE and the two preceding ones. From this fit t^* can be determined.

The time offset δt^* as indicated in Figure 3.11 can be computed by

$$\delta t^* = \Delta t \cdot \frac{E}{E - D} = \Delta t \cdot q, \tag{3.55}$$

with $E = B - C$, $D = A - B$ and $q = \frac{E}{E-D}$. The nodal displacements are reset based on the computed nodal velocities of the latest two time levels:

$$\mathbf{u}_i(t^*) = \mathbf{u}_i(t + \Delta t) - \Delta t \cdot \dot{\mathbf{u}}_i(t + \Delta t/2) - \delta t^* \cdot \dot{\mathbf{u}}_i(t - \Delta t/2). \tag{3.56}$$

Substituting (3.51), (3.52) and (3.55) yields:

$$\mathbf{u}_i(t^*) = \mathbf{u}_i(t + \Delta t) - \Delta t(1 + q) \cdot \dot{\mathbf{u}}_i(t + \Delta t/2) + \frac{\Delta t^2}{2} \cdot q \cdot \frac{\mathbf{R}_i(t)}{m_i}. \tag{3.57}$$
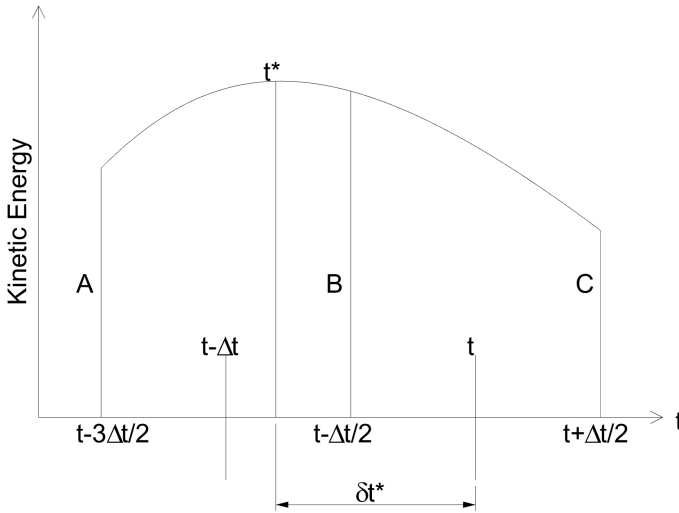
Figure 3.11: Determination of δt^* by quadratic approximation [12]

As a quasi-steady solution is searched for and transient states are of no consequence, selection of timestep length and virtual masses is basically arbitrary. Therefore, these values are set to ensure stability and optimise convergence. As mentioned above, numerically an oscillating system is modelled. Stability of such a system can be guaranteed, if the timestep length is smaller than the smallest eigenperiod of the system. Convergence will be optimal, if the timestep is as large as possible under the stability criterion. A schematic of the shortest eigenperiod is given in Figure 3.12. In this Figure each node, connected by structural links to the adjacent ones, is moving in the opposite direction to both adjacent ones.

Figure 3.12: Motion of adjacent nodes at minimum Eigenperiod [12]

The Eigenfrequency of such a system can easily be determined under the following conditions:

- The direct stiffness S of all links between nodes is the same

- The motion of all nodes is in line with the links, all nodes i are moving in the same direction at velocity $\dot{\mathbf{u}}_i$, all nodes j are moving in the opposite direction at velocity $\dot{\mathbf{u}}_j$

- The virtual mass m of all nodes is identical

From (3.52) the velocity at $t + \Delta t/2$ can be written:

$$\dot{\mathbf{u}}_i(t + \Delta t/2) = \dot{\mathbf{u}}_i(t - \Delta t/2) + \frac{\mathbf{R}_i(t)}{m} \Delta t. \tag{3.58}$$

Similarly for $t + 3\Delta t/2$:

$$\begin{aligned}\dot{\mathbf{u}}_i(t + 3\Delta t/2) =& \dot{\mathbf{u}}_i(t + \Delta t/2) \\ &+ \frac{\Delta t}{m} \left[\mathbf{R}_i(t) - S \cdot \Delta t \left(\dot{\mathbf{u}}_i(t + \Delta t/2) - \dot{\mathbf{u}}_j(t + \Delta t/2) \right) \right].\end{aligned} \tag{3.59}$$

The term in square brackets is equivalent to $\mathbf{R}_i(t + \Delta t)$.

Combining the above equations to eliminate $\mathbf{R}_i(t)$ yields:

$$\begin{aligned}&- \dot{\mathbf{u}}_i(t + 3\Delta t/2) + 2\dot{\mathbf{u}}_i(t + \Delta t/2) - \dot{\mathbf{u}}_i(t - \Delta t/2) \\ &= \frac{\Delta t^2}{m} \cdot S \left(\dot{\mathbf{u}}_i(t + \Delta t/2) - \dot{\mathbf{u}}_j(t + \Delta t/2) \right) \dot{u}.\end{aligned} \tag{3.60}$$

Similarly for nodes j:

$$\begin{aligned}&- \dot{\mathbf{u}}_j(t + 3\Delta t/2) + 2\dot{\mathbf{u}}_j(t + \Delta t/2) - \dot{\mathbf{u}}_j(t - \Delta t/2) \\ &= \frac{\Delta t^2}{m} \cdot S \left(\dot{\mathbf{u}}_j(t + \Delta t/2) - \dot{\mathbf{u}}_i(t + \Delta t/2) \right) \dot{u}.\end{aligned} \tag{3.61}$$

Introducing relative nodal velocities $\dot{\mathbf{u}}_{ij}$ between nodes and subtracting the two above equations yields:

$$- \dot{\mathbf{u}}_{ij}(t + 3\Delta t/2) + 2\dot{\mathbf{u}}_{ij}(t + \Delta t/2) - \dot{\mathbf{u}}_{ij}(t - \Delta t/2) = \frac{\Delta t^2}{m} \cdot S \cdot \dot{\mathbf{u}}_{ij}(t + \Delta t/2) \dot{u}. \tag{3.62}$$

From this equation the critical timestep length can be identified. It occurs when the relative velocity of a node to the adjacent ones at the current timestep is equal and opposite to the velocity at the previous timestep. At larger timesteps increase of total velocity and divergence of the solution may occur. By setting
$\dot{\mathbf{u}}_{ij}(t + 3\Delta t/2) = -\dot{\mathbf{u}}_{ij}(t + \Delta t/2) = \dot{\mathbf{u}}_{ij}(t - \Delta t/2)$,
(3.62) reduces to:

$$\Delta t = \sqrt{\frac{2m}{S}}. \tag{3.63}$$

If the dynamic behaviour of the nodes were of interest and the masses m were realistic masses, (3.63) would give the maximum allowable timestep for the entire system, based on the node with the smallest Δt. As in this case a quasi-static solution is sought and the timestep length and virtual masses are just a means of solution, an arbitrary timestep length Δt is chosen and the individual virtual masses m_i are calculated accordingly by:

$$m_i = \frac{\Delta t^2}{2} \cdot S_i, \tag{3.64}$$

with S_i being the largest direct stiffness node i is subjected to.

3.3. SOLUTION STABILITY AND CONVERGENCE

Commonly, stability of a time dependent discretised system of equations is evaluated according to stability theory, e.g. by *Von Neumann* stability analysis [14] commonly split into analysis of stability of time continuous discretised equations and time integration (see *Westhuis* [15] for example).

In the particular case of the above approach, the system of equation (commonly called *stiffness matrix*) is replaced by pseudo-time integration of equations of motion. Time integration is accomplished by the well-known leapfrog method (see Section 3.2.2). The stability of this method has bee well covered in literature (e.g. by *Birdsall et al.* [16]) where it has been shown that this method is stable for undamped oscillatory motion if the time step Δt is constant and $\Delta t \leq 2/\omega$. Actually, the calculation of the virtual nodal masses (Eqn. 3.64) for a given pseudo-time step is based on these criteria.

The actual stability of the code can be evaluated by numerical experiment: Based on the assumption that a fully converged solution is the exact solution to a particular case, it can be argued that any non-converged state of this case is the exact solution plus a perturbation. If during the progress of the computation (advancement of pseudo time step) this perturbation remains constant or reduce the simulation can be said to be stable. Figure 3.13 gives the RMS of the nodal displacement (solution variable) and the total force residual of the case (perturbation). As can clearly be seen, the RMS displacement converges to a constant value with most of the displacement taking place within the first iterations. Similarly, the force residual reduces strongly at the beginning of the simulation, with further convergence down to the given residual criterion. Obviously, this behavior fulfills the above criteria for stability. A similar pattern has been observed in the large number of simulations carried out using the code.

(a) RMS displacement   (b) Force residual
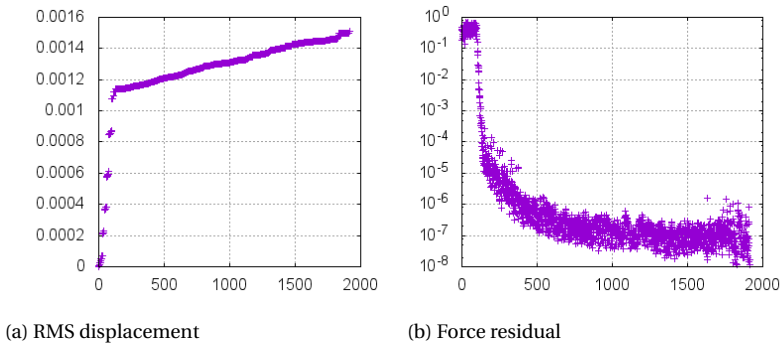
Figure 3.13: Progress of nodal RMS displacement and total force residual over outer iterations

The sole free variable of solver control is the virtual mass factor acting a multiplier to virtual masses computed according to (3.64) with a factor of one corresponding to the critical case given in the derivation of this equation. Theoretically, a factor equal and larger than unity should therefore result in an unconditionally stable system, while a smaller factor might lead to divergence of the solution if the actual Eigenperiod of the oscillation of one node is actually smaller than twice the time step.

In table 3.1 the convergence behaviour of the FE-code on a simple case is shown. On the abscissas the outer iterations are plotted, on the ordinates the RMS of nodal displacement, the total kinetic energy contained within the model and the force residual, respectively. Plots are for added mass factors of 0.8 to 1.8. While theoretically the solution of the system should diverge with a added mass factor smaller than unity, a valid solution is still reached given a factor of 0.8. This can be explained by a conservative assumption during the calculation of the added mass, basing this on the maximum single stiffness relative to opposing nodes a node may encounter. In practice, the system seems to be far more docile, indicating that the maximum stiffness encountered is quite a bit smaller.

Still, the diagrams show a consistent pattern: With increasing added mass factor a decreasing number of outer iterations until convergence (based on max. residual criterion) is required. Further, total kinetic energy as well as force residual show less scatter with increasing added mass factor.Especially with an added mass factor of 0.8 the plots look particularly "noisy".

REFERENCES

[1] O. C. Zienkiewicz, *The finite element method in engineering science <dt.>* (Hanser, 1971).

[2] V. F. Arcaro, *Finite element analysis of 3d orthotropic membrane structures,* Web.

[3] P. Heppel, *Accuracy in sail simulation: Wrinkling and growing fast sails,* in *1st High Performance Yacht Design Conference* (2002).

[4] J. Pitkäranta, *The problem of membrane locking in finite element analysis of cylindrical shells,* Numerische Mathematik **61**, 523 (1992).

[5] Y. W. Wong and S. Pellegrino, *Wrinkled membranes part iii: Numerical simulations,* Journal of Mechanics of Materials and Structures **1**, 63 (2006).

[6] R. K. Miller and J. M. Hedgepeth, *An algorithm for finite element analysis of partially wrinkled membranes,* AIAA Technical Notes **82**, 1761 (1982).

[7] S. Kang and S. Im, *Finite element analysis of wrinkling membranes,* Journal of Applied Mechanics **64**, 263 (1997).

[8] K. Lu, M. Accorsi, and J. Leonard, *Finite element analysis of membrane wrinkling,* International Journal for Numerical Methods in Engineering **50**, 1017 (2001).

[9] X. Liu, C. H. Jenkins, and W. W. Schur, *Large deflection analysis of pneumatic envelopes using a penalty parameter modified material model,* Finite Elements in Analysis and Design **37**, 233 (2001).

[10] W. H. Press, S. A. Teukolsky, W. T. Vetterling, and B. P. Flannery, *Numerical Recipes in Fortran 77, The Art of Scientific Computing*, 2nd ed., Vol. 1 (Cambridge University Press, 1992).

[11] W. H. Press, S. A. Teukolsky, W. T. Vetterling, and B. P. Flannery, *Numerical Recipes in Fortran 90, THE Art of PARALLEL Scientific Computing*, 2nd ed., Vol. 2 (Cambridge University Press, 1996).

[12] M. R. Barnes, *Form finding and analysis of tension structures by dynamic relaxation,* International Journal of Space Structures **14**, 89 (1999).

[13] V. G. Chapin, N. de Carlan, and P. Heppel, *Performance optimization of interacting sails through fluid structure coupling,* in *The Second Interantional Conference on Innovation in High Performance Sailing Yachts* (2010).

[14] J. Charney, R. Fjörtoft, and J. Neumann, *Numerical integration of the barotropic vorticity equation,* Tellus A **2** (2011).

[15] J.-H. Westhuis, *The Numerical Simulation of Nonlinear Waves in a Hydrodynamic Model Test Basin*, Ph.D. thesis, Universiteit Twente (2001).

[16] C. Birdsall and A. Langdon, *Plasma Physics via Computer Simulation*, Series in Plasma Physics and Fluid Dynamics (Taylor & Francis, 2004).

3

3
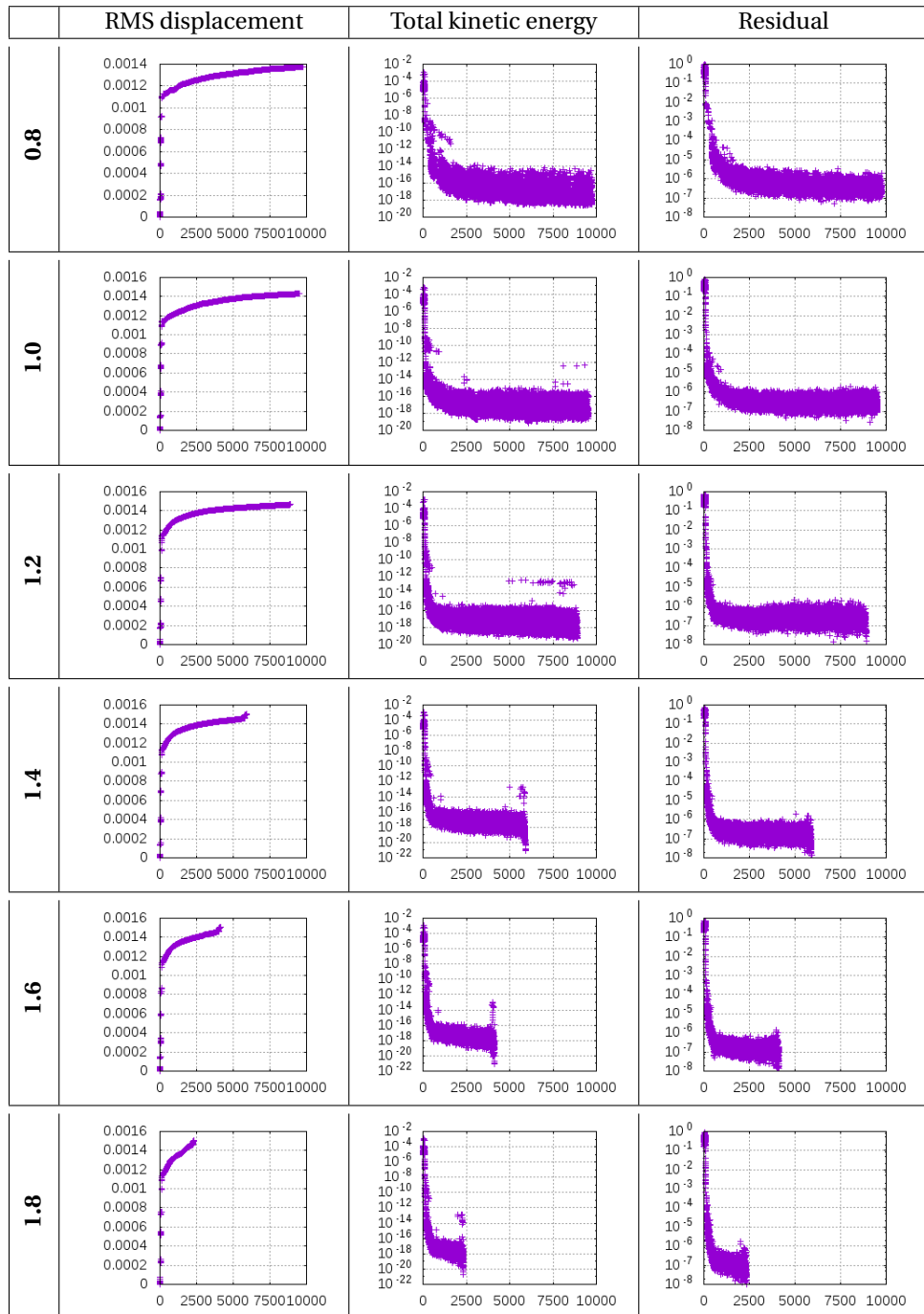
Table 3.1: Convergence behaviour of FE-code depending on virtual mass factor (left column) plotted over outer iterations.

4

FLUID-STRUCTURE-INTERACTION

Generally, the interaction between fluid flow around and structural behaviour of a body takes place at the interface between fluid and solid (see 4.1).

For numerical implementation and analogue to the CFD and FEA methods described in the previous chapters the coupling needs to be discretised in space and time. As the interface is infinitely thin, this results in surface elements with known location of the elements' centres or corners at the completed time steps.

Based on these discretisations the fluid-structure-interaction problem can either be solved using a monolithic approach with fluid and solid domain simulated in one single solver or in a segregated approach by splitting the problem at the interface between fluid and solid into two sub-problems solved by appropriate programs (e.g. CFD and FEA).

By splitting into two sub-problems the need arises for the two solvers to communicate in an organised fashion. Usually this means both solvers work sequentially, transferring only the required data at the interface to the other solver. The coupling of both domains needs to be ensured by appropriate boundary conditions at the interface (see Section 4.1.1).

Given the typical implementation of simulation codes for transient behaviour, consisting of a time-loop containing an "outer" loop (e.g. SIMPLE-loop in a RANS code) within which the linearised system of equations is solved repeatedly, three different levels of coupling between flow and structural simulation are described in literature (e.g. *Hou et al.* [1]).

At the closest coupling level, commonly called "monolithic", the equations describing the linearised behaviour of the flow and those describing the linearised behaviour of the structure are part of a single system of equations and are solved together. Therefore, the actual coupling step - an interface between a flow and a structural simulation code - is unnecessary in this kind of implementation.

Hou et al. [1] describe the inherently implicit coupling and guarantee of fulfilling the interface conditions described in Section 4.1.1 as the main advantages of the monolithic coupling approach. The need to develop a bespoke FSI code instead of being able to re-use existing CFD and FEA solvers is given as the main disadvantage.

A segregated coupling approach, using separate CFD and FEA solvers, allows re-using existing solutions by using a bespoke interface implementation. Obviously, the separation of the solution into two domains requires iterations to ensure a valid state of the interface due to non-linearities not accounted for (see *Förster et al.* [2]) in the data exchange and solvers. Given a segregated coupling approach where separate solutions for flow and structural behaviour are coupled by an interface, two coupling levels are described:

At the tightest of these two coupling levels the coupling between the two codes is located within the "outer" loop, typically at the beginning, allowing an update of the interface (the boundary) for each "outer" iteration. In principle, this yields a fully converged coupled system per time step. This kind of coupling is commonly called "strong" or "semi-implicit".

The loosest of these two coupling levels the coupling is located within the time-loop, typically at the beginning. This results in an update of the interface once per time step. Obviously, the update in this kind of coupling is only an extrapolation of the previous timestep's result, therefore it can only describe a valid transient result if the effects of the interaction are limited (a "weak" interaction) and linearisation is a valid approximation. This kind of coupling is commonly called "weak".

If we consider the flow to be almost steady, a (quasi-)static approach can be considered. Essentially, this is a weak coupling in which the time derivative is disregarded and only the final result is of interest. This can for example be achieved by alternating calling steady flow and structural solutions with the interface updated in between or a weak coupling where the interface is updated only every n-th time step.

In the following, this thesis will focus on the sequential approach.

4.1. THEORY

4.1.1. INTERFACE CONDITION

In any fluid-structure-interaction simulation, regardless of the coupling approach, the interaction of fluid and solid domain takes place only at the interface between those two. Based on this assumption, these two domains can be coupled by an appropriate description of boundary conditions. Assuming balance of stresses and equality of velocities, as argued by *Wall et al.* [3], these can be written as dynamic and kinematic boundary conditions:

$$\boldsymbol{\sigma}_s \cdot \mathbf{n} = -\boldsymbol{\sigma}_f \cdot \mathbf{n}, \tag{4.1}$$

$$\dot{\mathbf{x}}_s = \dot{\mathbf{x}}_f, \tag{4.2}$$

with $\boldsymbol{\sigma}$ being a stress tensor acting on the interface at a location $\mathbf{x}$, $\mathbf{n}$ the interface normal at this location and subscript s denoting structural and subscript f denoting fluid domain quantities.

The dynamic boundary condition as given in (4.1) represents a Neumann condition of transferring stresses acting on the interface from fluid to structural domain containing steady (e.g. due to shape of geometry) as well as transient (e.g. due to motion of geometry) components. The kinematic boundary condition as given in (4.2) is a Dirichlet condition transferring surface velocities from structural to fluid domain, ensuring a *no-slip* condition of the fluid side of the interface.

4.1.2. SEQUENTIAL COUPLING

In a sequential coupling approach it is assumed that each code, CFD as well as FEA, is only connected to the other one by the boundary conditions at the interface, as described above. The individual codes do not have (or need) any information about the other beyond this boundary condition. Therefore, the coupling algorithm handling the data exchange at the interface is responsible for ensuring the validity and stability of the solution at this interface. Due to the nature of this coupling, with each code requiring boundary data from the other, the codes have to solve their respective system of equations in turn, while iteratively approaching a converged common solution. A flow chart of this coupling is given in Figure 4.1.
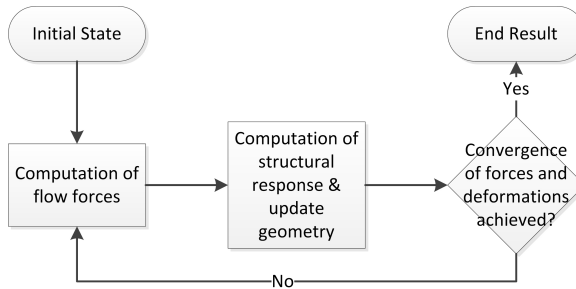
Figure 4.1: Generalised flow chart of sequential FSI coupling

Without advancing time from one iteration to the other this coupling results in a converged steady solution. When advancing simulated time from one iteration to the next it results in an explicit or weak transient coupling. In this case, the domain first solved in the time/iteration loop (CFD in Figure 4.1) is always reacting on an explicitly extrapolated solution of the other domain from the previous time step. Due to lack of corrector loops, time accuracy of the coupling is lost when using this approach as soon as non-linear behaviour in time is present at one or both sides of the interface.

If time accuracy is required for such a problem, it requires strong or (semi-)implicit coupling. The iteration loop - at constant time - has to be included in an outer time advancing loop with convergence of the iteration loop achieved at each time step. Such an approach is depicted in Figure 4.2.

Even in this approach an explicit component is always present, leading to particular issues as described below.

4.1.3. SOLUTION STABILITY

Due to the separation into two codes calculating in turn with input data from the previous results of the other code a significant explicit component is introduced (see *Förster et al.* [2]). This separation introduces an effect called "artificial added mass". This "artificial added mass" manifests itself in a significant flow force acting in opposite direction to the preceding boundary displacement. The artificiality of the added mass will be explained below.

The effect of this added mass can actually be compared to physical added mass imposed on a geometry being accelerated through a fluid and, for a given acceleration, is
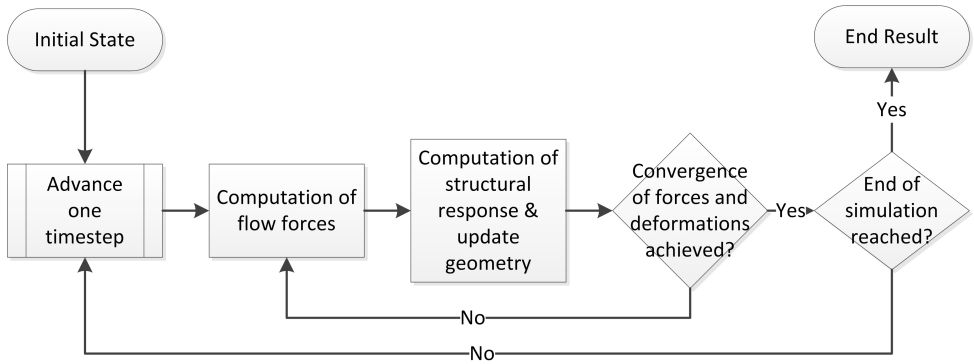
Figure 4.2: Generalised flow chart of (semi-)implicit sequential FSI coupling

of similar magnitude as this actual physical added mass. Due to the explicit component the boundary displacement (and corresponding acceleration) of the non-converged solution is often significantly larger than of the converged solution. Therefore the added mass and resulting forces are significantly larger than for the converged solution.

Whilst the impact of this effect is small as long as the structure has significant physical mass, keeping the ratio between added and body mass significantly below unity, it can fully destabilise the solution if the structure is light enough for the mass ratio to be equal or larger than unity. Looking at membrane structures, respectively sails in particular, the mass ratio can reach 40 and larger.

Stabilisation of the solution can be achieved in the most basic way by under-relaxation of velocities within the time step. Proof given by *Xing* [4] for rigid body motion shows that this kind of relaxation effectively introduces an added mass into the computation of accelerations of body mass divided by relaxation factor.

For a single node of a discretised flexible structure this can be derived in similar fashion with the equation of motion of the node given as:

$$\ddot{\mathbf{x}} = \frac{\mathbf{f}}{m}, \tag{4.3}$$

with **f** containing internal (structural) as well as external (flow) forces and m being the mass of the associated part of the structure.

Applying an implicit trapezoidal time integration scheme yields for the motion of this node at iteration $i+1$ of time step $t+1$:

$$
\begin{aligned}
\dot{\mathbf{x}}_{t+1}^{i+1} &= \dot{\mathbf{x}}_t + \frac{\mathbf{f}_t + \mathbf{f}_{t+1}^{i+1}}{2m} \Delta t \\
&= \dot{\mathbf{x}}_t + \frac{\mathbf{f}_t}{m} \Delta t + \frac{\mathbf{f}_{t+1}^{i+1} - \mathbf{f}_t}{2m} \Delta t,
\end{aligned}
\tag{4.4}
$$

with $\dot{\mathbf{x}}_t$ and $\mathbf{f}_t$ being the velocity and total force at the end of the converged time step t.

Introducing under-relaxation by factor β against the result of iteration i yields:

$$\dot{\mathbf{x}}_{t+1}^{i+1} = \beta \left[\dot{\mathbf{x}}_t + \left(\frac{\mathbf{f}_t + \mathbf{f}_{t+1}^{i+1}}{m} \right) \left(\frac{\Delta t}{2} \right) \right] + (1 - \beta) \dot{\mathbf{x}}_{t+1}^i$$
$$= \dot{\mathbf{x}}_t + \frac{\beta \Delta t}{2m} \left(\mathbf{f}_t + \mathbf{f}_{t+1}^{i+1} \right) + (1 - \beta) \left(\dot{\mathbf{x}}_{t+1}^i - \dot{\mathbf{x}}_t \right). \tag{4.5}$$

Adding an added mass term m_{add} to (4.3) the equation of motion becomes:

$$(m + m_{add}) \ddot{\mathbf{x}} = \mathbf{f} + m_{add} \ddot{\mathbf{x}}. \tag{4.6}$$

Again applying implicit trapezoidal integration, it can be obtained that:

$$\dot{\mathbf{x}}_{t+1}^{i+1} = \dot{\mathbf{x}}_t + \frac{\Delta t}{m + m_{add}} \left(\frac{\mathbf{f}_t + \mathbf{f}_{t+1}^{i+1}}{2} + m_{add} \frac{\dot{\mathbf{x}}_{t+1}^i - \dot{\mathbf{x}}_t}{\Delta t} \right)$$
$$= \dot{\mathbf{x}}_t + \frac{\Delta t}{2(m + m_{add})} \left(\mathbf{f}_t + \mathbf{f}_{t+1}^{i+1} \right) + \frac{m_{add}}{m + m_{add}} \left(\dot{\mathbf{x}}_{t+1}^i - \dot{\mathbf{x}}_t \right). \tag{4.7}$$

Comparing (4.5) and (4.7) it becomes apparent that

$$\frac{\beta \Delta t}{2m} = \frac{\Delta t}{2(m + m_{add})} \quad \text{or} \quad 1 - \beta = \frac{m_{add}}{m + m_{add}} \quad \Rightarrow \quad \beta = \frac{m}{m + m_{add}}. \tag{4.8}$$

As argued by *Xing* [4] and *Soeding* [5], the relaxation factor β needs to be chosen smaller than the ratio of body mass and the sum of body and added mass (see (4.8)). For very light structures, like membranes, this results in very small relaxation factors (e.g. ≤ 0.025 for a ratio of e.g. 40), requiring large numbers of iterations per time step until convergence with the associated computational effort.

Looking at the last two term of (4.7) and considering

$$\frac{\left(\mathbf{f}_t + \mathbf{f}_{t+1}^{i+1} \right)}{2m} \quad \text{as} \quad \frac{\left(\dot{\mathbf{x}}_{t+1}^{i+1} - \dot{\mathbf{x}}_t \right)}{\Delta t}, \tag{4.9}$$

the average acceleration during the time step from solution $i+1$, it becomes apparent that the effect of the added mass vanishes when convergence is reached and $\dot{\mathbf{x}}_{t+1}^{i+1} = \dot{\mathbf{x}}_{t+1}^i$. Therefore m_{add} can be considered as artificial as it is introduced into the computation of the motion to counter the solution-method induced instability. In the converged state the effect of the physical added mass is included in the forces resulting from the computation of the flow.

4.1.4. BOUNDARY INTERPOLATION

When using two separate simulation codes (as in sequential coupling) various data have to be transferred at the interface. These data are not present as continuous field functions but discretised in space depending on the respective simulation grids for each domain. These simulation grids can either be *conforming* or *non-conforming* (see *Hou et al.* [1]) meaning, having common nodes at the interface or being entirely different. This is further complicated by CFD and FEA codes usually having a different use of the grid with CFD-codes mostly being finite volume based (see Appendix B) and structural

simulations mostly based on finite elements (see Section 3.1). While the CFD-code uses cell-centered data, valid for the entire cell, the FEA-code uses node-centered data with element values in between calculated by a shape function (e.g. linear interpolation). This discrepancy usually results in the need for interpolation of data from one boundary grid to the other, while requiring conservativity of stresses and velocities (see above).

In the particular coupling discussed in this thesis, some peculiarities of the codes involved can be used to simplify the coupling significantly. Except for beam elements not accounted for in the CFD simulation, the FEA-code is based entirely on triangular elements with external forces and resulting displacements only given at the nodes. The CFD code uses the dual of the volume mesh (see Figure B.1) for computation of volume integrals, resulting in triangular surface elements with data stored at the nodes when used in combination with a tetrahedron-based mesh.

As the CFD-code returns the surface stresses at the nodes, not the forces, some inter-polation is required here. To this end the normal stresses (= pressure) acting on each tri-angular element are computed by averaging the stresses given at the three nodes defin-ing this element (4.10), the forces on the nodes are computed by distributing the forces on the element resulting from these stresses to the nodes again (4.11):

$$P_{element} = \frac{1}{3} \sum_{nodes} P_{node}, \tag{4.10}$$

considering only the three nodes defining the particular element and

$$\mathbf{F}_{node} = \frac{1}{3} \sum_{elements} P_{element} \mathbf{n}_{element} A_{element}, \tag{4.11}$$

considering all elements attached to the particular node, with $\mathbf{n}_{element}$ being the ele-ment normal and $A_{element}$ its area.

4.2. STEADY STATE IMPLEMENTATION

As stated before, due to the requirement for short computational times and reliable con-vergence, in this work only the converged steady state result is of interest. This reduces the kinematic boundary condition of the interface (4.2) to continuity of displacements

$$\mathbf{x}_s = \mathbf{x}_f. \tag{4.12}$$

Similarly, first and second order time-dependent components of (4.1) are supposed to vanish, meaning that $\boldsymbol{\sigma}_s$ and σ_f should contain only deformation respectively shape dependent components.

In principle, due to this simplification, the time loop could be omitted from the cou-pling (see Section 4.1.2). In this case transient behaviour would not be of interest in the CFD or FEA codes. While this assumption is used to simplify the FE code, solving only for a steady state result per FSI-iteration (see Section 3), the peculiarities of the employed CFD code require using a pseudo-transient CFD simulation, with an arbitrary time step length as required for a stable CFD-solution, to enable mesh deformation. Obviously, on the CFD side this re-introduces the first and second order time dependent components

in (4.1) and (4.2), with $\dot{\mathbf{x}}_f$ computed within the CFD code, requiring under-relaxation of deformations according to (4.8).

In practice, on the CFD side the coupling is only included every n-th CFD time step (e.g. every 5th) to allow dynamic effects in the CFD solution to subside. The nodal displacement calculated by the FE-code is strongly under-relaxed to ensure solution stability (see Section 4.1.3). This results in a weakly coupled FSI-approach disregarding any time-accuracy but giving quick convergence towards a stable result (see above).

The typical convergence behaviour is shown in Figure 4.3 with one iteration being one pseudo-time step. As can be clearly seen, the majority of the boundary displacement takes place within the first 100 CFD iterations (20 FE iterations). Beyond that, the RMS of the displacement as well as the forces are quite constant with an oscillation about every 80th CFD iteration, probably induced by instationary flow behaviour in the CFD solution.
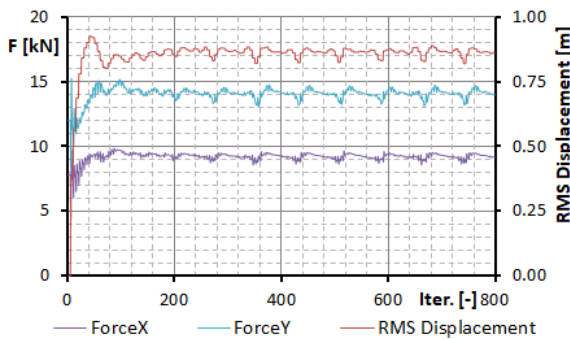
Figure 4.3: Typical convergence behaviour of the weakly coupled FSI simulation

REFERENCES

[1] G. Hou, J. Wang, and A. Layton, *Numerical methods for fluid-structure interaction - a review,* Communications in Computational Physics **12**, 337 (2012).

[2] C. Förster, W. A. Wall, and E. Ramm, *Artificial added mass instabilities in sequential staggered coupling of nonlinear structures and incompressible viscous flows,* Computational Methods in Applied Mechanics and Engineering **196**, 1278 (2007).

[3] W. A. Wall, S. Genkinger, and E. Ramm, *A strong coupling partitioned approach for fluid-structure interaction with free surfaces,* Computers & Fluids **36**, 169 (2007).

[4] Y. Xing-Kaeding, *Unified Approach to Ship Seakeeping and Maneuvering by a RANSE Method,* Ph.D. thesis, Technische Universität Hamburg-Harburg (2006).

[5] H. Soeding, *How to integrate free motions of solids in fluids,* in *4th Numerical Towing Tank Symposium,* edited by V. Bertram (2001).

5

VERIFICATION AND VALIDATION

As any simulation method based on spatial and temporal discretisation is only an approximation modelling the physical reality, the errors and sensitivities due to modelling and discretisation as well as the accuracy compared to the physical reality have to be assessed and quantified. This is done by *verification* and *validation*. During verification, the sensitivity to temporal and spatial discretisation is evaluated. During validation the verified models are compared to physical reality to assess the impact of simplifications in describing the complex physical reality by mathematical models. This results in guidance on model-selection as well as a measure for achievable accuracy. Successful verification and validation of models and computational setup allows to confidently simulate cases without the existence of experimental data, if the case is similar enough to the verified and validated case.

To quantify the accuracy and reliability of a simulation several measures have to be defined (see *Stern et al.* [1]):

- The simulation error δ_S as difference between simulation result S and the truth T (objective reality):

$$\delta_S = S - T = \delta_{SM} + \delta_{SN},\tag{5.1}$$

  where δ_{SM} and δ_{SN} are the additive modelling and the numerical error, respectively

- The simulation uncertainty

$$U_S^2 = U_{SM}^2 + U_{SN}^2\tag{5.2}$$

- Under certain conditions, for simulations it it possible to estimate the numerical error both in sign and magnitude δ_{SN}^*:

$$\delta_{SN} = \delta_{SN}^* + \varepsilon_{SN},\tag{5.3}$$

  where ε_{SN} is the error in the estimate

47

- From this the corrected simulation value $S_C = S - \delta^*_{SN}$ is calculated as numerical benchmark, leading to the corrected simulation error and uncertainty equations:

$$\delta_{S_C} = S_C - T = \delta_{SM} + \varepsilon_{SN}, \tag{5.4}$$

$$U^2_{S_C} = U^2_{SM} + U^2_{S_CN}, \tag{5.5}$$

with U_{S_CN} being the uncertainty estimate for ε_{SN}

Within this section, first wind tunnel tests conducted to provide a validation database are described. Further, the implemented models and setups are verified and validated by appropriate methods (e.g. *Method of Manufactured Solution (MMS)* for models or *Convergence Studies* for the assessment of discretisation sensitivities) and comparison against experimental, or where appropriate, analytical data. Model selection is evaluated and discussed and accuracy measures are given.

A detailed description of published experiments and analytical models used for verification and validation is given in Appendix A.

5.1. WIND TUNNEL EXPERIMENT ON SPINNAKER

As little quantitative experimental data on downwind sail aerodynamics and structural behaviour is available, testing of a setup of spinnaker and mainsail was conducted at the *Yacht Research Unit Kiel* twisted flow wind tunnel. For these measurements an aerodynamic model of a generic 40' yacht was fixed to a 6-DOF balance situated on a turntable. The yacht was fitted with mainsail and spinnaker. The sails have kindly been provided by *Segelmacherei Holm, Schleswig,Germany*. Table 5.1 gives the main particulars of wind tunnel and model.

TFWT measurement section width	3500m
TFWT boundary layer section height	2400mm
TFWT, distance BL-section - model	1800mm
TFWT reference velocity	5m/s
Model height	1800mm
Model length	1200mm
Model freeboard	105mm
Model fore triangle base (J)	460mm
Model fore triangle height (I)	1440mm
Model main sail area	0.49m^2
Model spinnaker area	0.91m^2
Model spinnaker leech lengths	1430mm

Table 5.1: Main particulars of TFWT and model

The general layout of the wind tunnel and an impression of the measurement setup is given in figure 5.1.

Incident flow in the wind tunnel is conditioned to resemble in velocity and direction the apparent wind profile encountered by a sailing yacht. The wind profile without
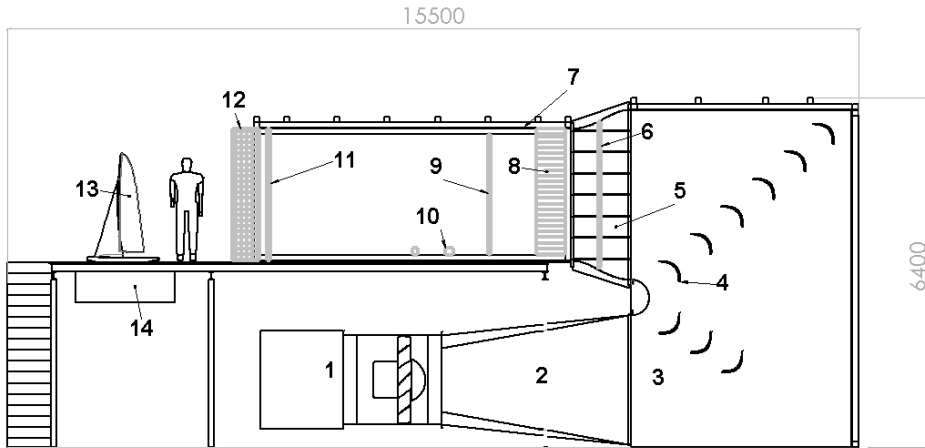
Figure 5.1: Layout oft the YRU-Kiel TFWT

model has been measured using 3-D hot wire anemometry. Concurrent flow velocity measurements upwind of the masthead during sail testing was conducted using a 1-D hot wire anemometer. During the measurements the sails shapes were recorded using photogrammetry after optimal trim for a given apparent wind angle had been established.

For automated image detection model and sails were fitted with coded targets. The photos were taken by four simultaneously triggered cameras of type *Canon EOS 350D* placed around the model. Processing of the photos was done using the *Photo Modeler Pro, EOS Systems Inc., Canada* software. The detected targets were exported as point clouds, NURBS surfaces were generated using *Rhinoceros 4.0, Robert McNeel and Associates* CAD software.

Tests were conducted over an AWA range of 67.5 to 180° in steps of 7.5°. In figure 5.2 driving and side force areas over AWA resulting from the TFWT tests are shown. The jump of force areas between 120° and 127.5° AWA is quite conspicuous, it can probably be explained by a change from a regime of mostly attached flow to one of detached flow.

The experimental setup is exemplarily shown in figure 5.3, a comparison of design and flying shape is given in figure 5.4

Due to the presence of twisted flow the actual flow field can not be assumed to follow a prescribed mathematical distribution of velocity and direction but has to be measured for use in simulations. Figures 5.5 a to c indicate the measured flow quantities.

For the purpose of validating the fluid structure interaction model, additionally the settings of all adjustable sail trim variables were recorded, these being:

- spinnaker sheet

- spinnaker aftguy

- spinnaker downhaul

- spinnaker sheet lead

- main sheet

- main vang
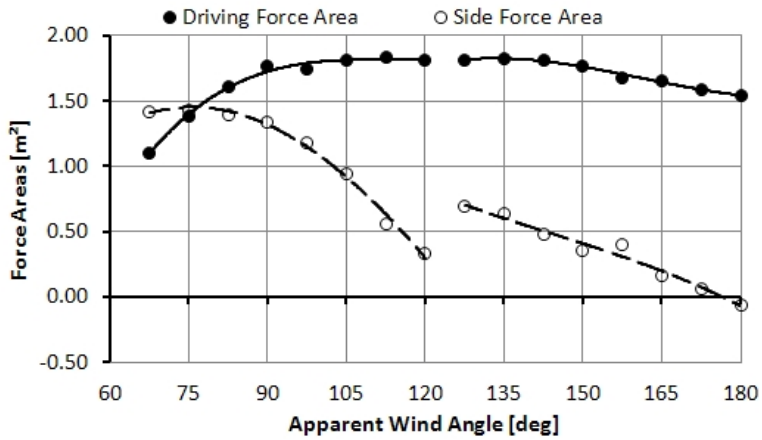
Figure 5.2: Driving and side force areas over AWA as measured in the twisted flow wind tunnel.
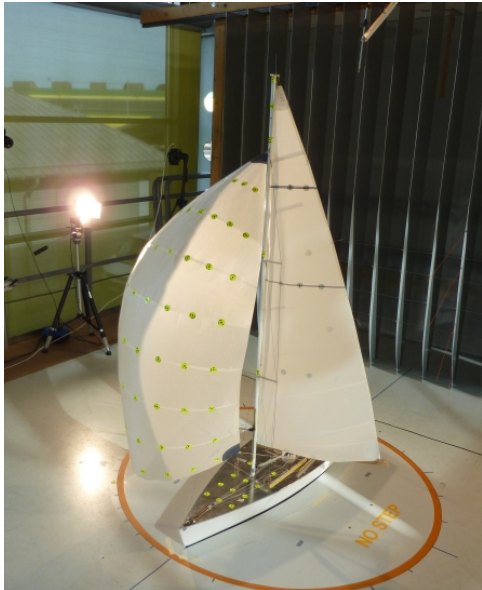
Figure 5.3: Measurement setup in the twisted flow wind tunnel.
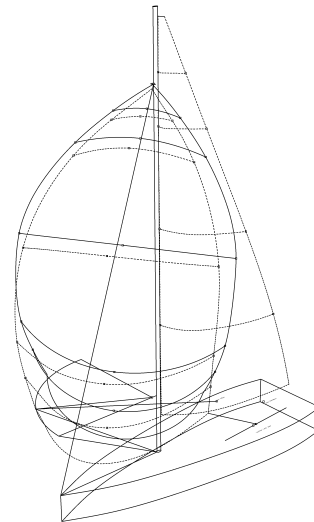
Figure 5.4: Comparison of design and flying shape.
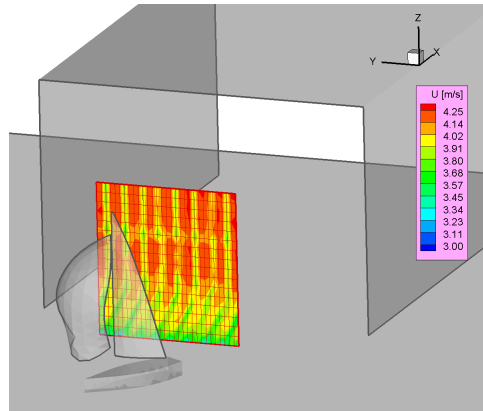
(a) Wind speed
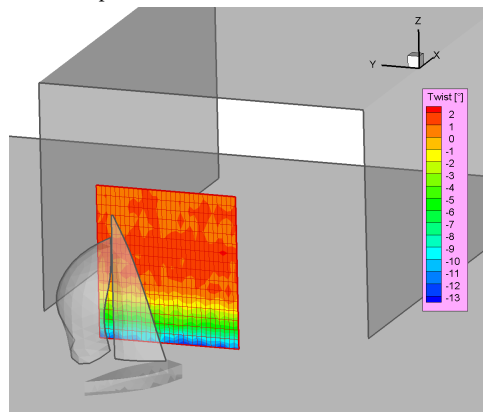
(b) Twist angle
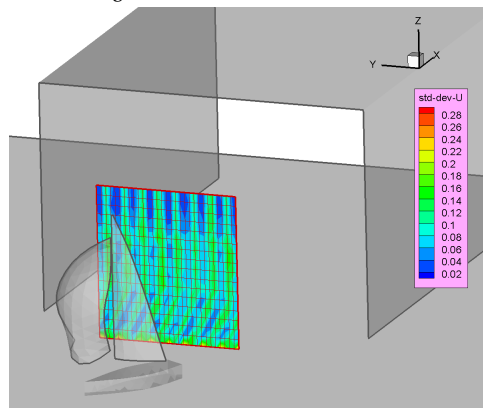
(c) Wind speed deviation

Figure 5.5: Measured Flow conditions in YRU-Kiel twisted flow wind tunnel

5.2. VERIFICATION

5.2.1. VERIFICATION METHODS

As in any CFD or FEA simulation spatial and temporal physical reality have to be approximated by discretisation, the errors introduced by this have to be evaluated, depending on step size. To this end convergence studies are carried out. As time step and grid size cannot be made infinitesimally small, the basic idea of this convergence studies is to compute a control variable as function of step size and extrapolate this to a step size of zero. This is then taken as grid invariant solution. Based on this result the errors introduced by the discretisation are evaluated.

Various methods have been published for the verification of numerical simulations. Two of the most widely accepted are presented and used in the following sections.

CONVERGENCE STUDY

By *Convergence Studies* (see *Stern et al.* [1]) the magnitude of discretisation errors in numerical simulations is determined. To this end the kth input parameter Δ_{x_k} (e.g. element size or time step length) is systematically varied, typically by a factor of $\sqrt{2}$ or 2, while keeping all other input parameters fixed at the finest level. Based on changes of a selected solution variable for medium to fine parameter $\varepsilon_{k_{21}} = \hat{S}_{k_2} - \hat{S}_{k_1}$ and coarse to medium parameter $\varepsilon_{k_{32}} = \hat{S}_{k_3} - \hat{S}_{k_2}$ the convergence ratio for three refinement steps is defined:

$$R_k = \frac{\varepsilon_{k_{21}}}{\varepsilon_{k_{32}}}, \tag{5.6}$$

where $\hat{S}_{k_1}$, $\hat{S}_{k_2}$ and $\hat{S}_{k_3}$ correspond to the selected result with fine, medium and coarse input parameter. From this convergence ratio the convergence condition is determined:

- Monotonic convergence: $0 < R_k < 1$

- Oscillatory convergence: $R_k < 0; |R_k| < 1$

- Monotonic divergence: $R_k > 1$

- Oscillatory divergence: $R_k < 0; |R_k| > 1$

In case of monotonic convergence a *generalised Richardson extrapolation* (see below) is used to estimate the uncorrected and corrected convergence uncertainties U_k and U_{k_c} as well as the sign and magnitude of the convergence error δ^*. In case of oscillatory convergence, given that the mean value of results is not drifting as a function of input parameter size, the uncertainty is determined based on oscillation minimums S_L and maximums S_U:

$$U_k = \frac{1}{2}(S_U - S_L). \tag{5.7}$$

To obtain an accurate estimate, observed values need to occur near minimums/maximums of the oscillation, therefore it might be necessary to compute more than three samples. For diverging conditions, errors and uncertainties cannot be estimated.

The *Generalised Richardson Extrapolation* is used in the case of monotonic convergence to estimate the error δ_k^* and order-of-accuracy p_k due to the selection of the kth input parameter. With $m = 3$ solutions (as typically used) only the leading term of the

error and order of accuracy for the finest input parameter k_1 can be evaluated, leading to one-term estimates:

$$\delta^*_{RE_{k_1}} = \frac{\varepsilon_{k_{21}}}{r_k^{p_k} - 1}, \tag{5.8}$$

$$p_k = \frac{ln(\varepsilon_{k_{32}}/\varepsilon_{k_{21}})}{ln(r_k)}, \tag{5.9}$$

with the uniform parameter refinement ratio r_k. Unless the solution is in the asymptotic range ($p_k > 1$) (5.8) only gives a poor estimate of the rate of convergence.

To improve the estimate of $\delta^*_{RE_{k_1}}$ and estimate the numerical error and uncertainty δ_{SN} and U_{SN} (see (5.1) and (5.2)) the correction factor C_k is calculated based on (5.8) and (5.9). To this end the numerical error is defined as

$$\delta^*_{k_1} = C_k \delta^*_{RE_{k_1}} = C_k \frac{\varepsilon_{k_{21}}}{r_k^{p_k} - 1}, \tag{5.10}$$

where C_k is calculated from (5.10) with $\delta^*_{RE_{k_1}}$ based on (5.8), but replacing observed p_k with an improved estimate $p_{k_{est}}$:

$$C_k = \frac{r_k^{p_k} - 1}{r_k^{p_{k_{est}}} - 1}. \tag{5.11}$$

Here $p_{k_{est}}$ is an estimate for the limiting order-of-accuracy of the first term (see above) as Δ_{x_k} goes to zero and the asymptotic range is reached ($C_k \rightarrow 1$). (5.11) gives a rough estimate of higher order terms by replacing p_k with $p_{k_{est}}$ in (5.10) for an improved single-term estimate:

$$\delta^*_{k_1} = \frac{\varepsilon_{k_{21}}}{r_k^{p_{k_{est}}} - 1}. \tag{5.12}$$

As only $\varepsilon_{k_{21}}$ is present in (5.12) only two solutions are evaluated, however all three solutions are considered in the evaluation of U_k since C_k is part of its definition. The uncorrected and corrected uncertainty estimates U_k and U_{k_c} are computed according to *Stern et al.* [1], depending on C_k, by:

$$U_k = \begin{cases} [9.6(1-C_k)^2 + 1.1]|\delta^*_{RE_{k_1}}| & |1-C_k| < 0.125 \\ [2|1-C_k|+1]|\delta^*_{RE_{k_1}}| & |1-C_k| \geqslant 0.125, \end{cases} \tag{5.13}$$

$$U_{k_c} = \begin{cases} [2.4(1-C_k)^2 + 0.1]|\delta^*_{RE_{k_1}}| & |1-C_k| < 0.25 \\ [|1-C_k|]|\delta^*_{RE_{k_1}}| & |1-C_k| \geqslant 0.25. \end{cases} \tag{5.14}$$

For both estimates formulae are given for C_k-values sufficiently close to one (i.e. nearly input parameter-independent) as well as for C_k-values farther away from one, resulting in an increased factor of safety. The uncorrected uncertainty estimate U_k (5.13) is based on the absolute value of the corrector estimate plus the amount of the correction. The uncertainty estimate for a corrected solution (i.e. a numerical benchmark $S_c = S - C_k \delta^*_{RE_{k_1}}$) U_{k_c} (5.14) is based on the absolute value of the amount of the correction.

Method of Manufactured Solution

The idea behind the *Method of Manufactured Solution* is to provide a possibility to track the individual error sources (e.g. discretisation or iteration) during the verification process by imprinting a continuous, mathematically defined starting solution of a generic flow variable ϕ, ϕ_{exact}, on the discretised model and compare the result of the discretisation process ϕ_i to this continuous solution (see *Eça et al.* [2]).

The normalised error e is defined as

$$e = \frac{\phi_i - \phi_{exact}}{\phi_{exact}} . \tag{5.15}$$

To assess the error induced by spatial discretisation, for example, usually the RMS of the nodal errors of all grid cells or elements is evaluated:

$$RMS(\phi) = \sqrt{\frac{\sum_{i=1}^{n_{nodes}} (\phi_i - \phi_{exact})^2}{n_{nodes}}} . \tag{5.16}$$

This approach allows to quantify an error without the need to calculate an integral result as used in Section 5.2.1.

5.2.2. Structural Model

Verification case

For verification of the structural model a simple case is considered at various systematically varied grid resolutions. The results are evaluated by Generalised Richardson Extrapolation, if applicable (see Section 5.2.1), and the discretisation error determined. In this evaluation the planar bending of a pre-tensioned beam-like membrane as described by *Stein et al.* [3] (see Appendix A.1) is chosen:

A rectangular membrane is pre-tensioned by forces applied to its left and right edges. Then equal and opposite moments are applied to these edges to induce bending. If the moments are applied as depicted in Figure 5.6, wrinkles start to form at the lower edge when negative horizontal stresses due to the moment cancel out the pretension. The comparison to analytically determined results is given in Section 5.3.1
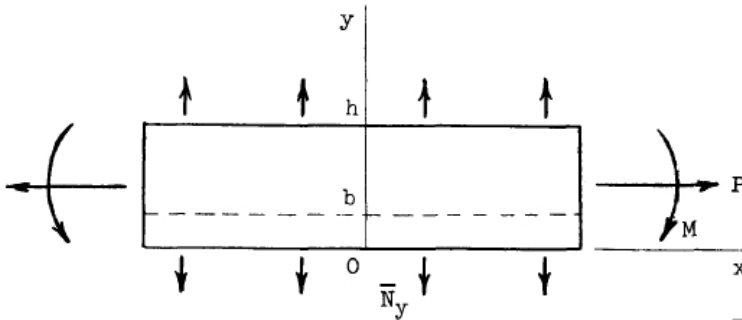
Figure 5.6: Topology and applied forces and moments [3]

To assess grid dependence of the structural simulation method the same case was simulated on three systematically refined grids and with as well as without wrinkling model. The results are evaluated by generalised Richardson extrapolation according to the publication by *Stern et al.* [1]. The cases used for verification are described in Table 5.2. The medium grid is shown in Figure 5.7, the finer grids are systematically generated by halving all edge length from one grid to the next.

For a description of the variables, please see Appendix A.1.

Width of membrane	1000	mm
Height of Membrane	200	mm
E*t	100	N/mm
Applied stretch	0.5	mm
Applied rotation	0.01	rad
No. of elements, coarse	160	-
No. of elements, medium	640	-
No. of elements, fine	2560	-

Table 5.2: Cases for verification of structural simulation method
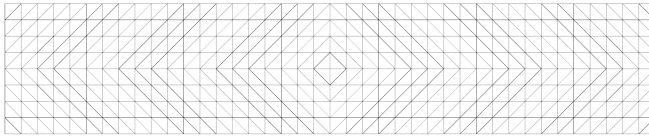
Figure 5.7: Medium grid used for verification of structural code

RESULTS

The computed control parameter (normalised bending moment)

$$\frac{2M}{Ph},\tag{5.17}$$

with M being the applied moment for a given rotation of the ends of a membrane of height h under pre-tension P is evaluated as function of grid refinement according to the procedure given in Section 5.2.1. The results are given in Table 5.3 and Figure 5.8. As can be seen, monotonic convergence is achieved with as well as without wrinkling model.

CONCLUSION

In the cases described above, the effect of grid resolution on the computed results in simulations with and without wrinkling model is investigated. In both cases the results indicate monotonic convergence in the asymptotic range. For the results on the finest grid an uncertainty of 1.3% is estimated with a discretisation error of 0.3% respectively 0.5% and nearly second-order convergence. Based on these results, the solution on the finest grid can be considered as verified.

		Unwrinkled	Wrinkled
Parameter ratio	r_{12}	2.0	2.0
Parameter ratio	r_{23}	2.0	2.0
Normalised moment delta	ε_{12}	0.014	0.007
Normalised moment delta	ε_{23}	0.054	0.023
Convergence ratio	R	0.251	0.301
Error	$\delta^\star$	0.005	0.003
Order of accuracy	p	1.992	1.732
Uncertainty	U_{12}	0.013	0.013
Uncertainty	U_{23}	0.051	0.041

Table 5.3: Convergence parameters of grid dependence study, wrinkled and unwrinkled

5.2.3. FLOW SIMULATION

Verification of the flow model by systematic grid variation is carried out for two- as well as three-dimensional flow. The effect of grid resolution on forces acting on the respective geometries is evaluated as described in Section 5.2.1.

VERIFICATION OF FLOW MODEL FOR TWO-DIMENSIONAL FLOW

The verification of the flow model for two-dimensional flow is based on the geometry used by *Wilkinson* in his PhD-Thesis [4] (see Appendix A.3). For the purpose of verification, the flow forces acting on this geometry (not measured in the experiment) are evaluated as function of grid resolution and time step length.

The geometry consists of a section mimicking a horizontal cut through a mast and main-sail combination. To assess the effect of grid resolution (given by triangular element edge length T respectively by T normalised by chord length C (700mm)) on these flow forces the grid is systematically refined while keeping all other solution parameters fixed. Similarly, the time step size Δt is varied while keeping all other parameters fixed. Table 5.4 gives the parameters used in this study. These are the element size T, respectively element size normalised by chord length T/C, the time step length Δt and resulting from these the average and maximum Courant numbers Co_{avg} and Co_{max}. In all cases used for this verification study 2$^{\text{nd}}$ order spatial interpolation and time integration methods, the SST-turbulence model and an incident turbulence level of 5% are used.

The results of a formal analysis of grid dependence for edge lengths 4mm, 8mm and 16mm (grid 1, 2 & 3) and time step sizes of 0.00375s, 0.0075s and 0.015s (time steps 1, 2 and 3) following the method by *Stern et al.* [1], are given in Table 5.5. In this tabel lift and drag forces depending on grid resolution respectively time step length are given, further the resulting convergence parameters, corrected solution and uncertainty estimates.

The convergence ratios R paint a mixed picture. While harmonic convergence is indicated depending on time step size for lift as well as drag and grid convergence is present for lift, oscillatory divergence is indicated for drag depending on grid resolution. Still, even the larger force delta ε_{12} is less than 2% of of the actual solutions, indicating dependency on flow effects not harmonically dependent on grid resolution. A closer look at the
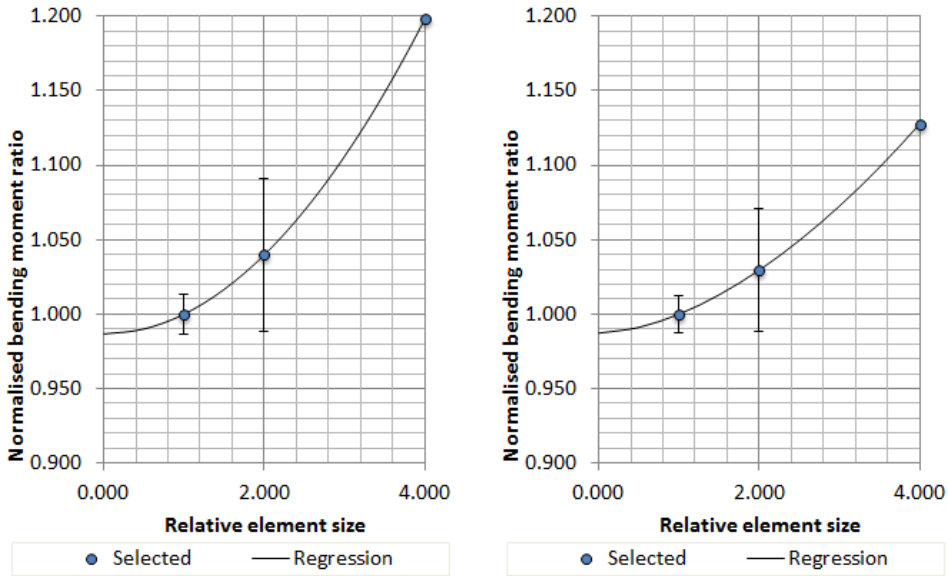
(a) Without Wrinkling

(b) With Wrinkling

Figure 5.8: Grid convergence of bending membrane verification case

flow patterns present around the geometry (see Figure 5.9) indicates significant areas of separated flow, probably unsteady, which may have this effect. A representation of the results is given in Figure 5.10. The *Relative step size* is in each case the varied parameter normalised by the finest variation, the *Control parameter ratio* is the result depending on the *Relative step size* normalised by the solution for the finest variation. Solutions 1 to 3 as well as the corrected solution S_c, if applicable, are shown.
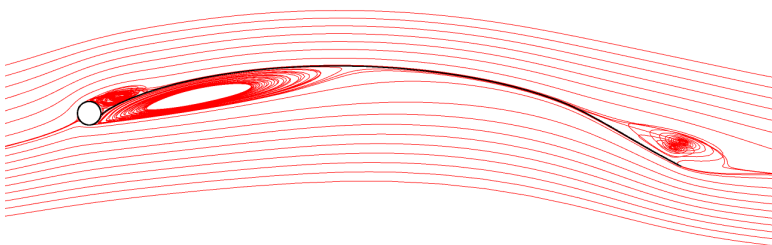
Figure 5.9: Flow pattern around mast and sail.

VERIFICATION OF FLOW MODEL FOR THREE-DIMENSIONAL FLOW

Similar to the above validation exercise the simulation of the three-dimensional flow around a boat-like geometry consisting of hull, main sail and spinnaker is verified. The grid parameters are given in Table 5.6, cell size T is normalised by the spinnaker's mid

5

(a) Normalised lift over grid resolution

(b) Normalised drag over grid resolution

(c) Normalised lift over time step

(d) Normalised drag over time step
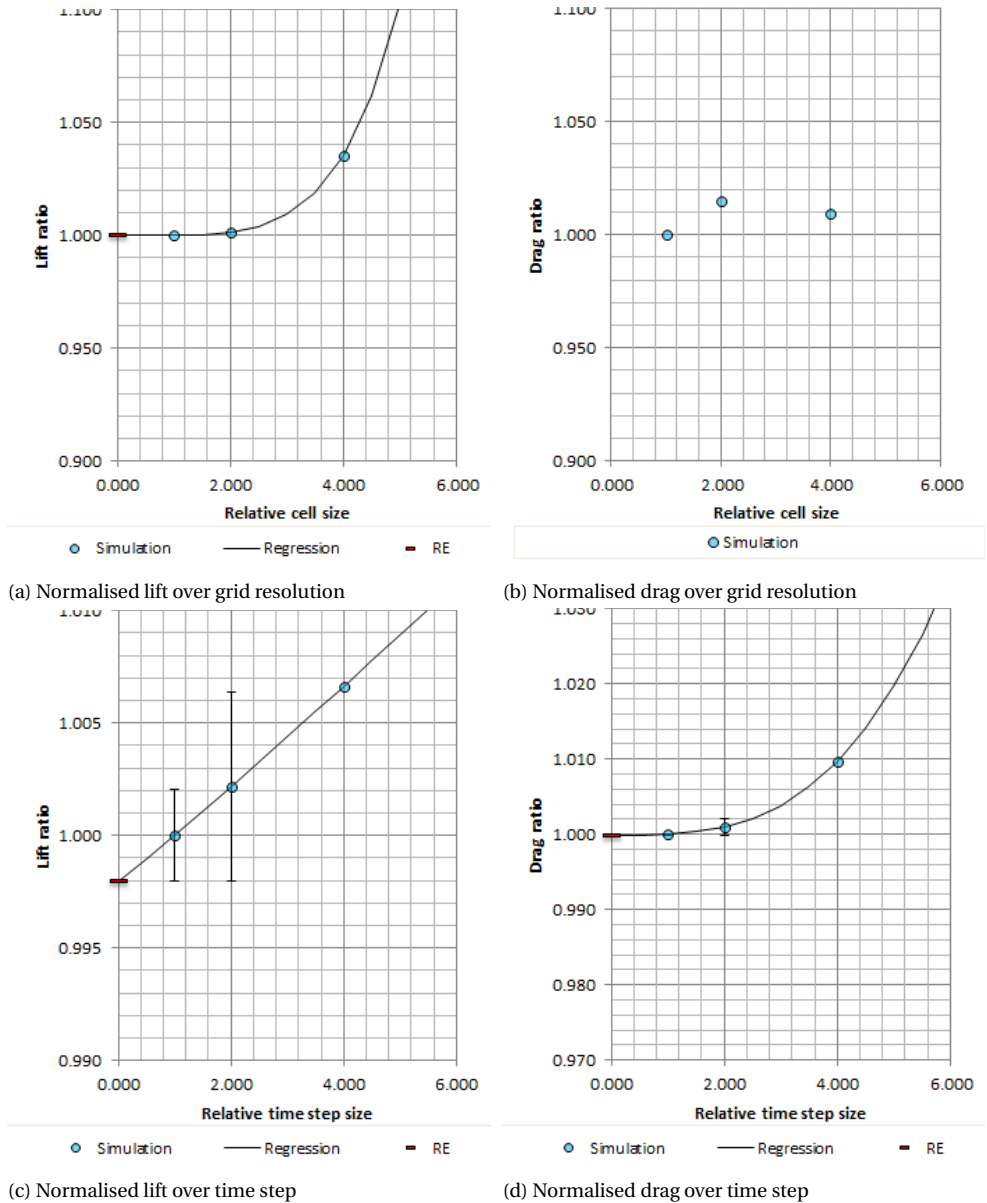
Figure 5.10: Convergence plots for verification of two-dimensional flow simulation model

Setup	T	T/C	Δt	Co_{avg}	Co_{max}
[-]	[mm]	[-]	[s]	[-]	[-]
1	16	2.29e-02	0.015	78.99	526.8
2	16	2.29e-02	0.0075	39.45	262.3
3	16	2.29e-02	0.00375	19.70	130.0
4	8	1.14e-02	0.00375	31.60	304.3
5	4	5.71e-03	0.00375	26.10	513.4

Table 5.4: Parameter variation for two-dimensional flow verification

Control Parameter	:	Lift(Grid)	Drag(Grid)	Lift(TS)	Drag(TS)
Solution 1	S_1	38.462	1.549	39.831	1.564
Solution 2	S_2	38.512	1.572	39.918	1.565
Solution 3	S_3	39.831	1.564	40.096	1.579
Parameter ratio	r_{12}	2.0	2.0	2.0	2.0
Parameter ratio	r_{23}	2.0	2.0	2.0	2.0
Force delta	ε_{12}	0.050	0.023	0.087	0.002
Force delta	ε_{23}	1.319	-0.009	0.178	0.014
Convergence ratio	R	0.038	-2.676	0.486	0.111
Error	$\delta^\star$	1.98E-03	-	0.082	0.000
Corrected Solution	S_c	38.460	-	39.749	1.564
Order of accuracy	p	4.718	-	1.041	3.167
Uncertainty	U_{12}	5.15E-05	-	2.06E-03	1.21E-04
Uncertainty	U_{23}	5.15E-05	-	4.22E-03	1.08E-03

Table 5.5: Results of grid and time step dependence study, two-dimensional flow

girth C of 768mm. Further, element counts of the surface meshes on the individual parts of the geometry are given. Inflation layers on the surfaces are designed for an estimated y^+ value of one. Simulations are performed at time step lengths of 0.025, 0.05 and 0.1s. The corresponding average and maximum Courant numbers for each grid are given in Table 5.7.

The results of a formal investigation of grid and time step sensitivity following the method by *Stern et al.* [1] are given in Figure 5.11. Interestingly, the results indicate harmonic divergence for lift depending on grid resolution, but harmonic convergence for all other cases. For time step dependence the asymptotic region has been reached. Still, computed and extrapolated force values depending on grid convergence lie within 5% of the finest grid's results. Deviation from the smallest time step's lift value is significantly larger for the large time step at 10% with drag values deviating by only 1% for the large time step. These results indicate strong unsteady effects affecting the lift force results. The convergence parameters for this study are given in Table 5.8
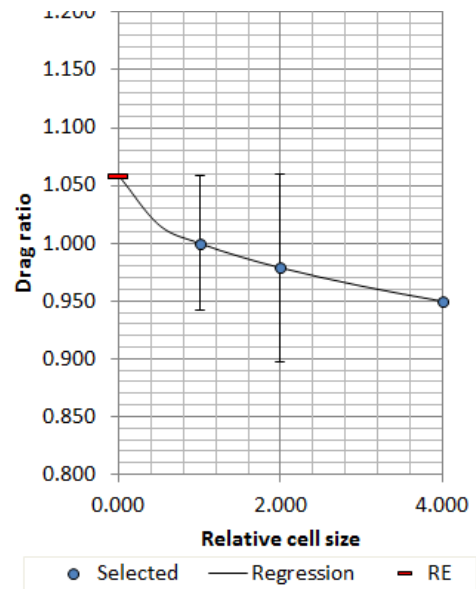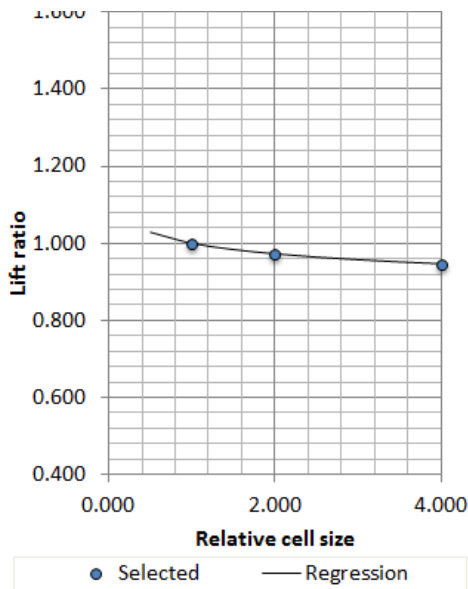
(a) Normalised lift over grid resolution
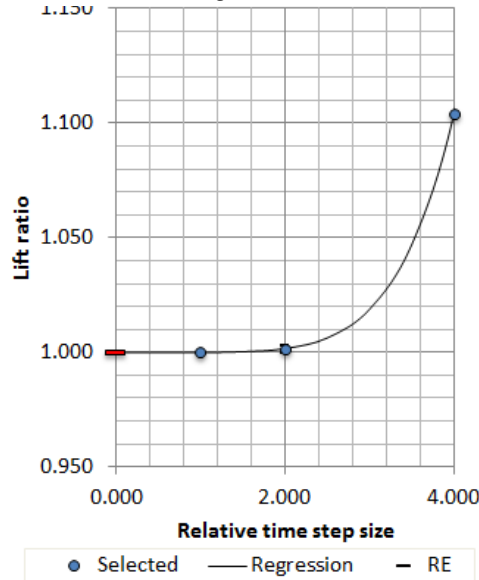
(b) Normalised drag over grid resolution
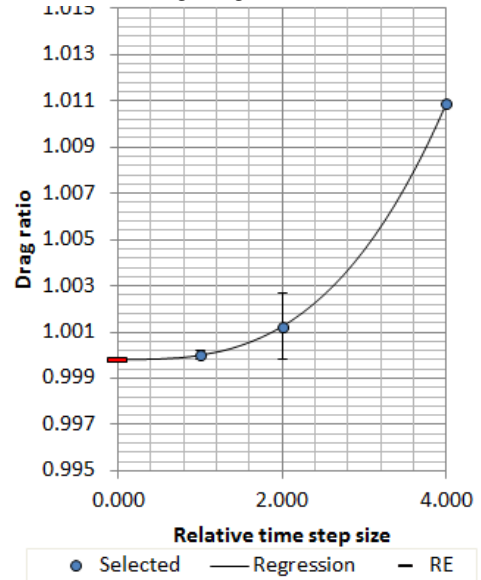
(c) Normalised lift over time step

(d) Normalised drag over time step

Figure 5.11: Convergence plots for verification of three-dimensional flow simulation model

Grid No.	T	T/C	$n_{Tri,Spi}$	$n_{Tri,Main}$	$n_{Tri,Hull}$
[-]	[mm]	[-]	[-]	[-]	[-]
1	16	2.08E-02	3.32E+04	1.66E+04	1.71E+04
2	32	4.17E-02	1.02E+04	4.88E+03	4.58E+03
3	64	8.33E-02	5.20E+03	2.30E+03	1.87E+03

Table 5.6: Base parameters for 3-D flow validation

Grid No.	Time Step	Co_{avg}	Co_{max}
[-]	[s]	[-]	[-]
1	0.1	77.67	2490
1	0.05	37.26	1274
1	0.025	18.63	636.9
2	0.1	64.98	2854
2	0.05	32.47	1425
2	0.025	16.23	712.2
3	0.1	75.42	7015
3	0.05	37.72	3508
3	0.025	18.87	1754

Table 5.7: Time step lengths and corresponding Courant nos.

CONCLUSION

From the verification exercises on the simulation of two- and three-dimensional flow issues with convergence of forces depending on grid resolution are obvious. Looking at the details of the flow it becomes apparent that in both cases the flow pattern is dominated by separation phenomena. Various studies (e.g. *Rodi* [5]) indicate that these separation phenomena are particularly difficult to simulate correctly and reliably using methods based on Reynolds-averaging of turbulent phenomena ((U)RANS) and that the assumption of monotonous convergence towards grid or time step insensitive resolution does not necessarily hold in these cases (*Eça* [2]).

5.2.4. FLUID-STRUCTURE-INTERACTION

VERIFICATION APPROACH

The verification of the coupling algorithm - after removal of any effects induces by the CFD or FE solution - reduces to the evaluation of the transfer of an arbitrary scalar or vectorial variable between the two codes. As the coupling algorithm contains no time-dependent functions, this verification reduces to the evaluation of grid dependency.

To this end an approach similar to *Method of Manufactured Solution* as described in Section 5.2.1 is used. Due to the significantly reduced complexity of the present case as compared to the papers by e.g. *Eça et al.* [2], the evaluation reduces to the RMS error of the transferred variable.

To mimic the pressure field as usually calculated by the CFD code and transferred to

Control parameter	:	Lift(Grid)	Drag(Grid)	Lift(TS)	Drag(TS)
Solution 1	S_1	23.730	19.159	23.730	19.159
Solution 2	S_2	23.084	18.753	23.770	19.183
Solution 3	S_3	22.470	18.198	26.201	19.367
Parameter ratio	r_{12}	2.0	2.0	2.0	2.0
Parameter ratio	r_{23}	2.0	2.0	2.0	2.0
Force delta	ε_{12}	-0.646	-0.407	0.039	0.024
Force delta	ε_{23}	-0.614	-0.554	2.431	0.184
Convergence ratio	R	1.051	0.734	1.61E-02	0.129
Error	$\delta^\star$	-	-1.121	6.42E-04	3.54E-03
Corrected Solution	S_c	-	20.280	23.730	19.156
Order of accuracy	p	-	0.447	5.955	2.951
Uncertainty	U_{12}	-	-5.85E-02	2.71E-05	1.85E-04
Uncertainty	U_{23}	-	-8.15E-02	1.68E-03	1.43E-03

Table 5.8: Results of grid and time step dependence study, three-dimensional flow

the FE code, a scalar variable is calculated by

$$\phi = x \cdot (x^2 + y^2 + z^2) \tag{5.18}$$

on part of a sphere oriented and sized as follows, here shown by the coarse grid:

    Due to the particular CFD and FE codes used, the variable is calculated at each node of the grid on the CFD side and interpolated to element-based variables on the FE side (see Section 4.1.4). As described above (see Section 4.1.4) the interpolation is based on the way the dual mesh is generated in the CFD code. To evaluate the effect this particular coupling including interpolation has on the variable respective simulations were carried out on three grids with a refinement factor of two in between.

RESULTS

The variables calculated at the element centres (exact solution) ϕ_{exact} and interpolated to the element centres ϕ_i as well as the error $e(\phi) = \frac{\phi_i - \phi_{exact}}{\phi_{exact}}$ is given for all three grids in Figure 5.13. While the decrease of the local interpolation error is already clearly visible from the plots, the global RMS of the error is calculated and further the conservativity is defined by

$$\mathbf{C}(\phi) = \sum_{i=1} n_{nodes}(\phi_i - \phi_{exact})\mathbf{n}_i \tag{5.19}$$

for elements i with $\mathbf{n}_i$ being the element normal. As $\sum \phi n_x$ and $\sum \phi n_y$ are are four to six orders smaller than $\sum \phi n_z$ (as they should be, due to symmetry), only $C_z(\phi)$ is evaluated. The results are given in Table 5.9. The decay of the error with increasing grid refinement can nicely be seen with the error decreasing by a factor of almost ten for a refinement of factor four. The decrease of the conservativity error is even more pronounced, reducing from 0.39% to 0.02% by refinement of factor four.

    Transferring a vectorial variable mimicking the displacement field in the reverse direction (FE to CFD) yields exactly the same displacement at the CFD side as entered at
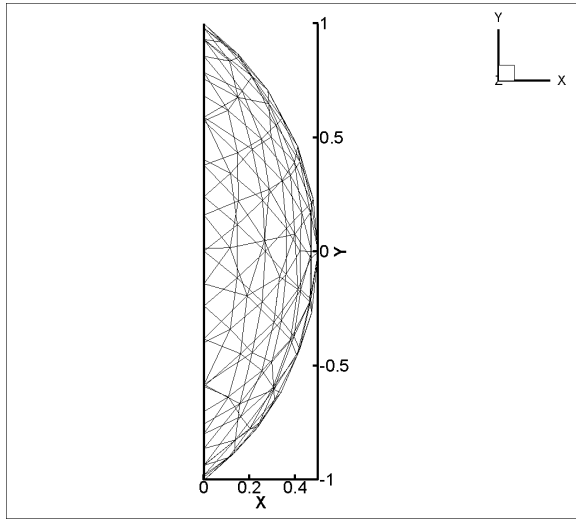
Figure 5.12: Geometry used for verification of coupling, coarse grid
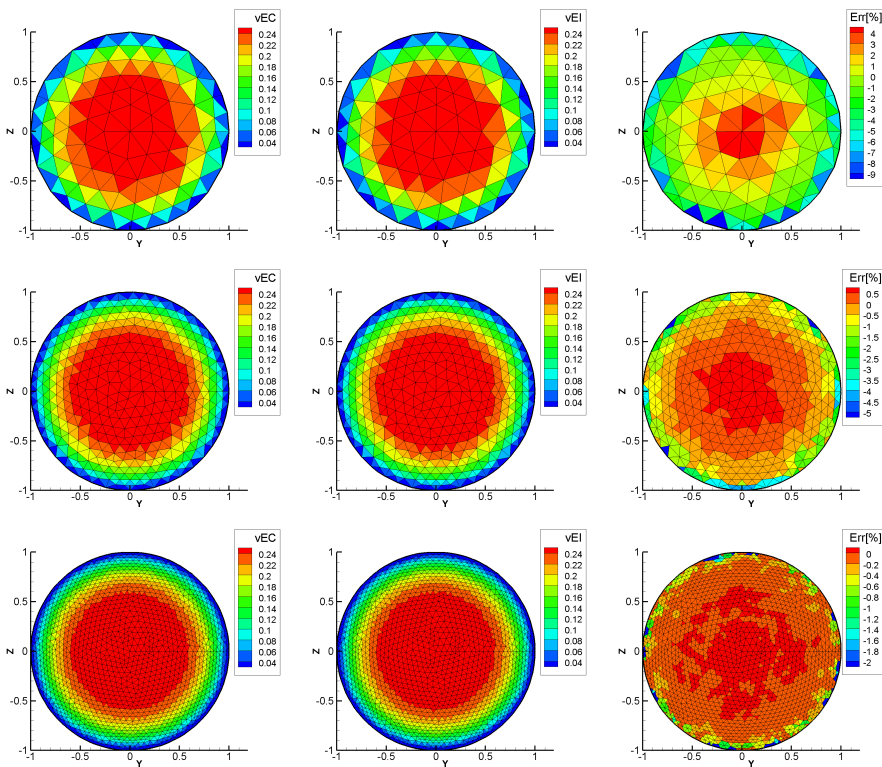
Figure 5.13: Calculated and interpolated variable values and interpolation error on all three grids; errors are at different scales, depending on actual value range.

Grid	Grid size factor	RMS(ϕ)	RMS(ϕ) error factor	$C_z(\phi)$	$C_z(\phi)$ error
1 (coarse)	4	3.57E-03	9.47	4.42E-03	0.39%
2 (medium)	2	9.54E-04	2.53	1.09E-03	0.09%
3 (fine)	1	3.77E-04	1.00	2.61E-04	0.02%

Table 5.9: Grid dependency of interpolation error

the FE side. This is due to this direction of the coupling being fully explicit and entirely node-based without any interpolation.

CONCLUSION
The accuracy and conservativity of the coupling algorithm depending on grid resolution are successfully shown by a demonstration case isolating coupling effects. The decay of interpolation as well as conservativity errors with increasing grid resolution is clearly evident, reducing to negligible values (0.02%).

5.3. VALIDATION
After the errors introduced by discretisation have been quantified in the verification process, the computed results have to be validated against reality, i.e. physical measurements. Comparing a discrete computed variable (e.g. a force) against measurements, the simulation error can be quantified, comparison of global behaviour of different setup choices against measurement aid in the selection of the correct setup.

5.3.1. STRUCTURAL MODEL
To validate the Finite Element code and assess its capabilities and accuracy two cases well documented in literature are chosen:

- Planar bending of a pre-tensioned beam-like membrane (*Stein et al., Lu et al.* [3, 6]).

- Bending of a pressurised membrane cylinder (*Stein et al.* [3]).

PLANAR BENDING OF A PRE-TENSIONED BEAM-LIKE MEMBRANE
For this validation exercise the same geometry and material properties as used in the verification exercise for the structural code (Section 5.2.2) are chosen. To assess the accuracy of the simulations on the finest grid used in Section 5.2.2 in comparison to the analytical results, several cases with different combinations of pretension and bending moment are evaluated, both with and without wrinkling model. To this end the ends of a membrane "beam" of 0.2m height, pretensioned by 50 N/m (10 N pull) are rotated by prescribed angles while keeping the total force between the ends constant (see Table 5.10).

The computed and analytical results are given in Figure 5.14, the deviation between these is shown in Figure 5.15. Typically, a deviation of two to four percent can be found,

case	end rotation
[-]	[rad]
1	0.00E+00
2	2.50E-03
3	6.25E-03
4	1.00E-02
5	1.50E-02

Table 5.10: Parameter variation for beam like planar bending of membrane

indicating satisfactory agreement. Figure 5.16 shows the stresses within the material. While in case 2 , just still in the unwrinkled range, the results are extremely similar, significant deviation can be found near the lower edges of case 5. Here a significant negative stress is present without wrinkling model, while, with wrinkling model, the stresses are always larger than 0.
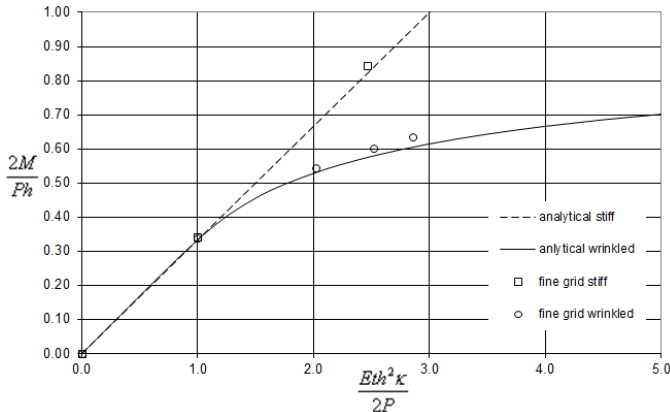
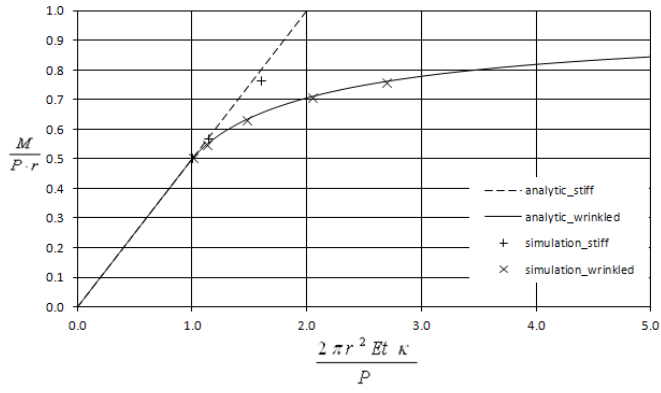
Figure 5.14: Analytical and computed results with and without wrinkling model

BENDING OF A PRESSURISED MEMBRANE CYLINDER

Similar to the case discussed above, *Stein et al.* [3] (pp. 13 - 18) give an analytical solution and experimental data for the bending moment and wrinkling behaviour of a pressurised membrane tube, as depicted in Figure 5.17 (see Appendix A.2).

Simulations are performed on a membrane cylinder of 1000mm length, 100mm radius, 0.0001mm wall thickness and $1.00E+11 N/mm^2$ Young's modulus. Similar to the beam like membrane, the cylinder is pre-tensioned and edge displacements are applied to give specific amounts of wrinkling, described by the ratio of circumference of the wrinkled region and radius of the cylinder b/r (see Figure 5.17). Additionally internal pressure of 1Pa is applied. The following table gives the particulars of the simulation cases.
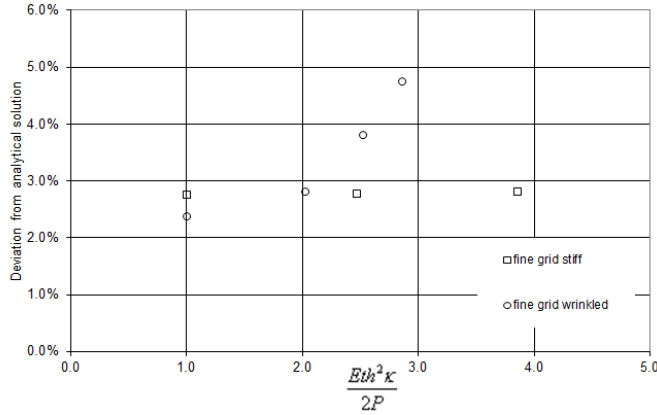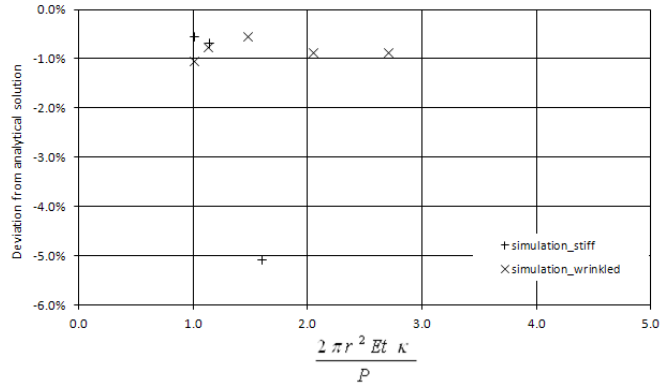
Figure 5.15: Deviation of normalised computed bending moments from analytical results with and without wrinkling model (from Figure 5.14

Case	b/r	P	M
[-]	[-]	[N]	[Nm]
1	0.0	628.32	31.42
2	$1/6\pi$	553.45	30.51
3	$1/3\pi$	382.64	25.27
4	$1/2\pi$	200.00	15.71
5	$2/3\pi$	68.49	6.14

Analytical and simulated results are given in Figure 5.18, the deviation of simulated from analytical results in Figure 5.19. The computed results for cases one and five are given in Figure 5.20.

While, with wrinkling model the results show a deviation between computed and analytical bending moments in the range of one percent for all cases, the errors without wrinkling model are off the chart for cases four and five. This can be explained by an effect called "grid-locking". Basically this means that the structure behaves like it is constructed out of stiff triangles (which it numerically is) whose corners may displace significantly out of the initial geometry. While this initially relieves the compressive stresses in longitudinal direction, like wrinkling does, significant circumferential compressive stresses occur which limit the nodal displacements. This effect can be seen in Figures 5.20c to 5.20f. While in case 1 (Figure 5.20c) the computation results are similar, in case 5 strong compressive stresses on longitudinal lines can be observed (Figure 5.20d). Similarly, strong compressive circumferential stresses can be observed in case 5 without wrinkling model (Figure 5.20e). The surface deflection pattern shown in Figure 5.20f corresponds to this observation.
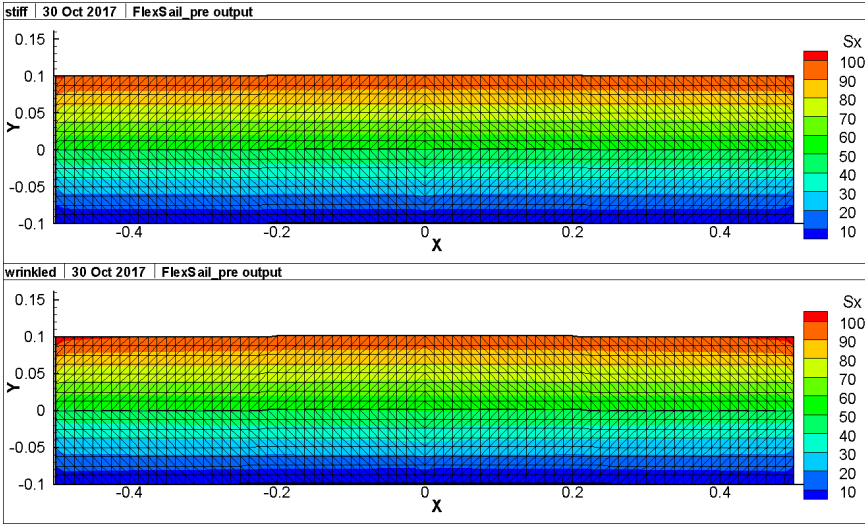
(a) Case 2
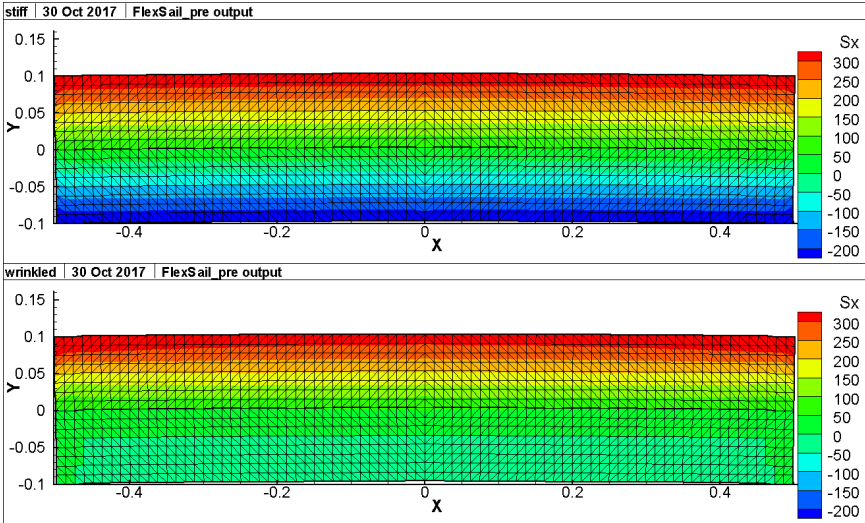
(b) Case 5

Figure 5.16: Longitudinal stresses in bending membrane
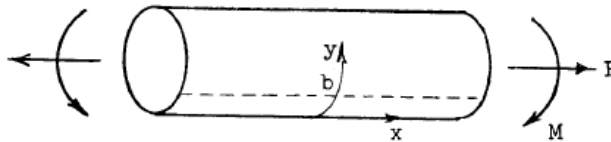
Figure 5.17: Topology and applied forces and moments [3]

Figure 5.18: Analytical and computed results with and without wrinkling model

Figure 5.19: Deviation of normalised computed bending moments from analytical results with and without wrinkling model
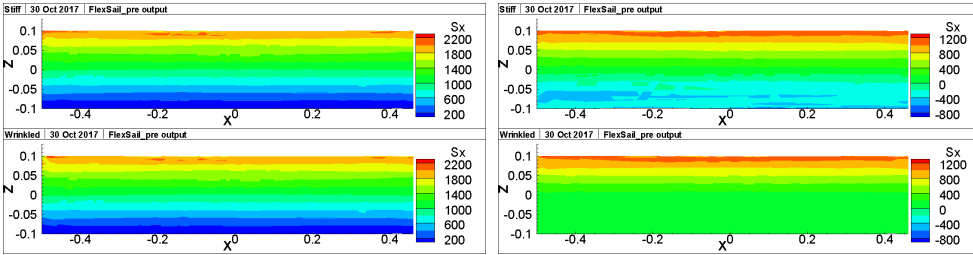
(a) Longitudinal stresses in tube, case 1.

(b) Longitudinal stresses in tube, case 5.
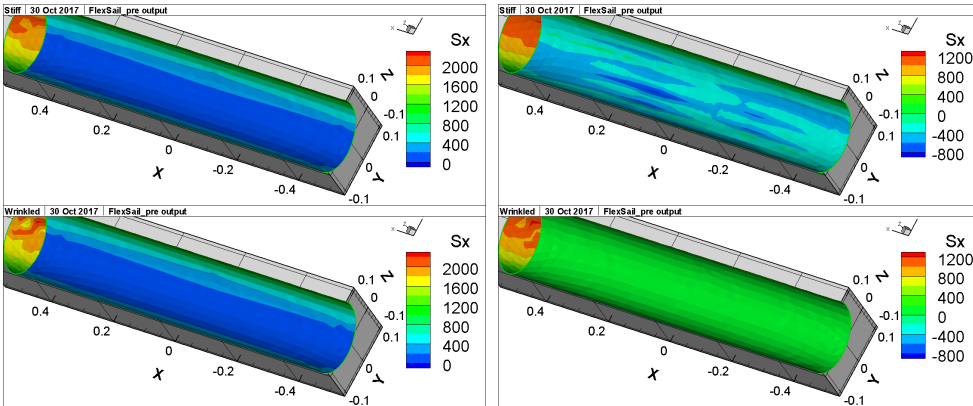
(c) Longitudinal stresses in compressed side of tube, case 1.

(d) Longitudinal stresses in compressed side of tube, case 5.
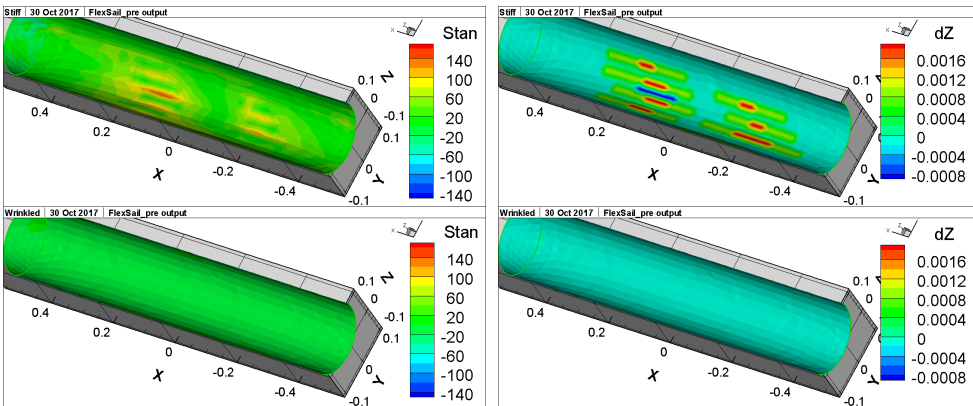
(e) Circumferential stresses in compressed side of tube, case 5.

(f) Deflection of compressed side of tube, normal to compressive stress, case 5.

Figure 5.20: Computed stresses and surface deflections of bending tube case without (each upper Figure) and with wrinkling model (each lower Figure).

Conclusion

Good agreement between analytical and simulated data is achieved for various testcases when using the membrane model with wrinkling model. Simulation results calculated without wrinkling model display large differences to analytical results; an issue arising due to shortcomings of the element model has been identified as the cause and is in fact rectified by the usage of the wrinkling model. The computed results indicate no relevant grid-dependency for the investigated cases.

As can bee seen from above validation cases, simulations with and without wrinkling model can be correct as long as the assumption of presence or lack of wrinkling is physically correct in the respective case (see Section 5.3.1). As soon as wrinkling is present in reality (bending beam without limitation to purely two-dimensional behaviour or fully three dimensional case (see Section 5.3.1)) the inclusion of a wrinkling model is of utmost importance for the correct prediction of nodal displacements and material stresses. Even more importantly, as shown on the pressurised tube, lack of a wrinkling model can lead to unphysical stiffening of the structure, resulting in erroneous local and global behaviour (see *Pitkäranta* [7] as well).

5.3.2. Flow Simulation Method

Validation of the flow simulation method is carried out in two stages. Simulation results of essentially two-dimensional flow are compared to published wind tunnel measurements, including detailed local pressure and flow velocity measurements. Flow forces calculated by simulation of three-dimensional flow are compared to wind tunnel measurements carried out especially for this purpose.

Data of two-dimensional flow around a sail-like section shape from wind tunnel experiments is available from *Wilkinson* [4]. Despite lacking force measurements, detailed pressure profiles indicating flow separation and reattachment areas as well as boundary layer velocity profiles are given.

Validation of three-dimensional flow around a spinnaker is based on data from a measurement campaign conducted within the scope of this thesis at the *Yacht Research Unit Kiel* (YRU-Kiel) Twisted Flow Wind Tunnel as described in Section 5.1.

Two-dimensional flow around sail-like section

As part of the research for his PhD-Thesis *Stuart Wilkinson* extensively tested a sail-section-like geometry at the University of Southampton wind tunnel at various Reynolds numbers and angles of attack (see Appendix A.3). During these tests the pressure distribution on the geometry's surface as well as boundary layer velocities (see Figure 5.22) were measured. These measurements resulted in a zonal model to describe the flow around the sail-like section (see Figure 5.21).

These zones are listed as:

I : Upper mast attached flow

II : Upper separation bubble

III : Upper reattachment

IV : Upper airfoil attached flow

V : Trailing edge separation

VI : Lower mast attached flow

VII : Lower separation bubble

VIII: Lower reattachment
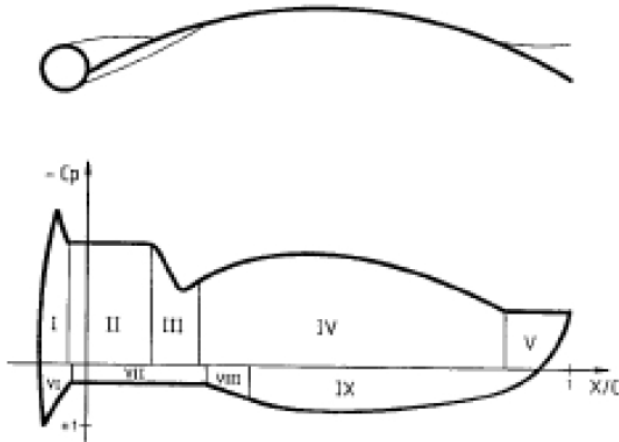
IX : Lower airfoil attached

Figure 5.21: Nine zones of flow around mast-sail combination as characterised by *Wilkinson* [4].
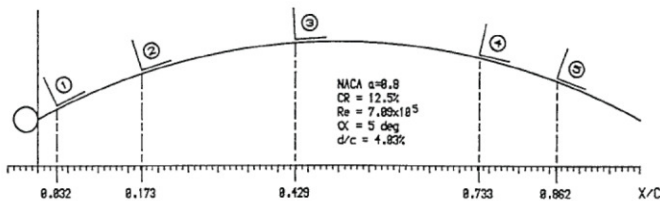

Figure 5.22: Locations for velocity measurements [4]

Of particular interest for the validation of the flow around spinnakers are the separation and reattachment zones on the upper (suction) side(III and V). The flow separation on the lower (pressure) side is dominated by the presence of the mast at the leading edge and is therefore not applicable to the flow around spinnakers

The flow around the sail section is simulated using the commercial RANS solver ANSYS-CFX12.1. The domain size mimics the size of the high speed section of the Southampton University No. 1 wind tunnel of 2.10m length and 1.50m height normal to span. Domain size in spanwise direction is set at 0.256m, assuming fully two-dimensional flow.

Grid resolution and time step length is based on the findings described in Section 5.2.3 (4 mm resp. 0.00375s). Particular care is taken during grid generation to keep the prognosticised dimensionless wall scale (y^+) below 2.0 and ensure a smooth transition from prism to tetra volumes. A cut through a typical grid near mast and sail is shown in Figure 5.23. Particular note should be paid to the highly refined grid in the area of strong curvature around the mast. This refinement is deemed to be necessary to correctly capture the flow - attached and detached - in this region.
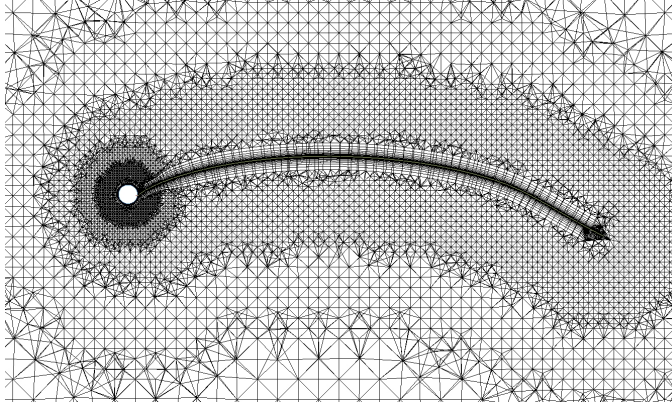
Figure 5.23: Slice through volume discretisation near mast and sail.

The base setup is based on second order modelling of temporal and spatial discretisation and the *Shear Stress Transport* (SST) turbulence model (see Appendix B.2.1) with 5% incident turbulence. To assess the effect on the quantitative results, a first order advection scheme as well as a Reynolds stress based turbulence model and a lower turbulence level are evaluated. Guidance for the choice of turbulence models is taken from the work by *Collie et al.* [8]. The investigated setups are given in Table 5.11

Setup	Turb. Int.	Discret.	Turb. Mod.	$Co_{Avg.}$	$Co_{Max.}$
[-]	[-]	[Order]	[-]	[-]	[-]
1	5%	2nd	SST	26.10	513.4
2	5%	1st	SST	28.28	483.1
3	1%	2nd	SST	26.02	512.5
4	5%	2nd	BSL EARSM	25.30	519.1

Table 5.11: Parameter variation for 2-D flow validation

In Figures 5.24 and 5.25 the results of this investigation are given. While generally all results capture the major quantitative trends of the measured data, some differences are observable. Interestingly, all setups under-predict the amount of separation, respectively recirculating flow, in Wilkinson's zone II and indicate a further forward location of zone III than measured. Considering this, it is remarkable that the onset location and

extent of separation in zone V is captured quite well by most setups, the most notable difference being setup 2.

Judging from Figures 5.24 and 5.25, the largest single impact on results is due to the choice of order of advection scheme (1st order for setup 2 versus 2nd order for all other cases). Compared to the other setups, pressure in zones I and IV (attached flow regime) is captured best in setup 2 while separation effects (zones II, III and V) are largely lost and pressure on the lower side is generally over-predicted in setup 2. Further the boundary layer appears to be significantly thinner in the results of setup 2.

The results for zone IV computed using setups 1, 3 and 4 are similar to each other, pressure is slightly under predicted while the velocity cuts show satisfactory agreement to measurements. Pressure as well as recirculation are under-predicted in zones I to III (even though less than with setup 2), indicating insufficient prediction of the separation zone. Interestingly the pressure in zone V is under-predicted again, while the velocity cuts indicate an over-prediction of recirculation. The most notable effect of turbulence modeling (model as well as level) can be found in the velocity cuts in the separation areas (profiles 1 and 5).

Comparing setups 1 and 3 the most notable difference can be seen on velocity cut 5 with the reduced turbulence level (setup 3) apparently resulting in an increase of recirculation, which is already over-predicted with setup 1. Changing the turbulence model from SST to the *Boundary Shear Layer Explicit Algebraic Reynolds Stress* (BSL EARSM) model (setup 4) - which is supposed to give better prediction of near wall (partially) separated flow due to computation of the anisotropic Reynolds stresses (see Appendix B.2.2) - results in changes to the velocity profile on cuts 1 and 5. Comparing the velocities, the reduction of recirculation in the near wall region on cut 1 as well as the increase of recirculation on cut 5 due to using the BSL EARSM model are evident. While no measurement data are available for comparison for this part of cut 1, the velocities computed using setup 1 are closer to the measured velocities than those computed with setup 4.

Calculations on the same experimental testcase were carried out by *Paton* [9] as well as *Trimarchi* [10]. While *Paton* used an unstructured tetrahedral-prism grid as well, *Trimarchi* used a block-structured hexahedral grid with C-shape topology. The following diagrams show the results of setup 1 overlayed on diagrams taken from *Paton* [9].

Looking at Figure 5.26, while the basic patterns of measured and both computed pressure distributions are very similar, the most obvious difference between the computed results is an almost constant offset on the upper side. While the pressure distribution computed by *Paton* agreed with the measured one between 40 and 80% chord and has an c_P offset of about 0.2 for most of the remainder, the distribution computed using setup 1 is offset by that value for the majority of the chord length. Major differences appear in both computations in front of 15% chord length (Wilkinson's regions II and III). Actually these, and the trailing edge, are the regions where spontaneous separations occur. These separations are notoriously hard to predict by CFD and can be highly dependent on geometry imperfections, flow disturbances and turbulence in experiments (*Paton* [9]). A possible reason for the constant c_P offset occuring on the upper side in setup 1 might be the domain size, which is larger by 30% than the actual wind-tunnel used for the measurements. This reduces blockage effects, in turn reducing local velocity and increasing pressure. On the lower side good agreement to measured values
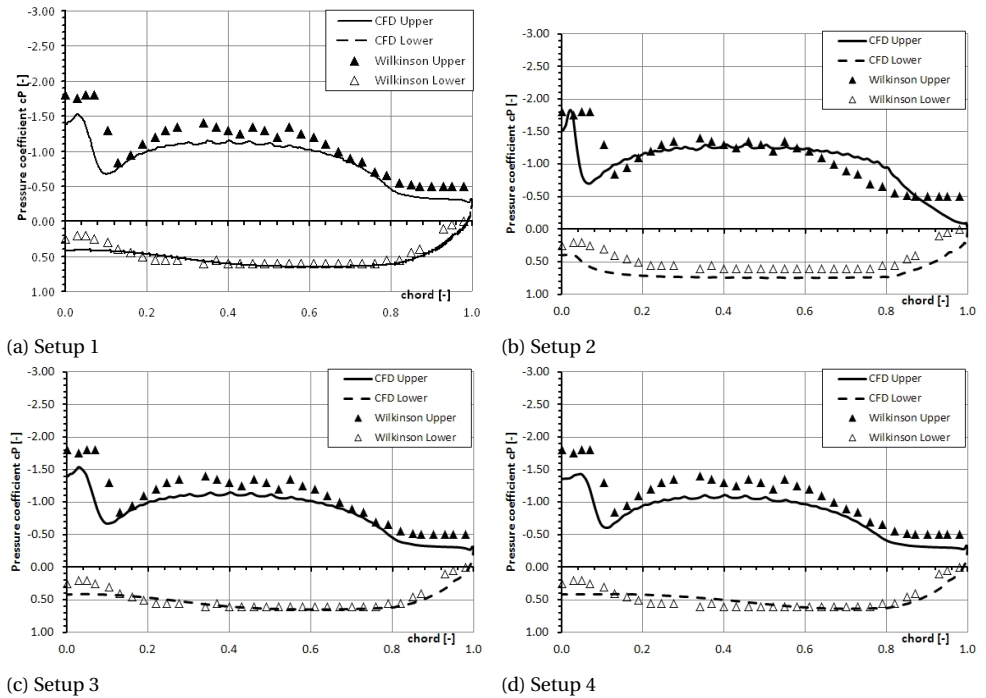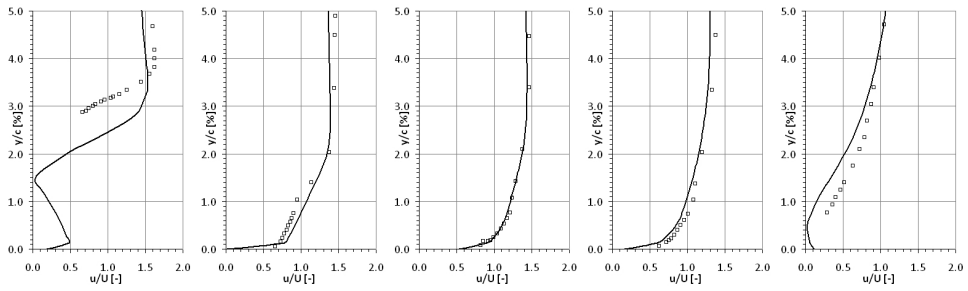
(a) Setup 1

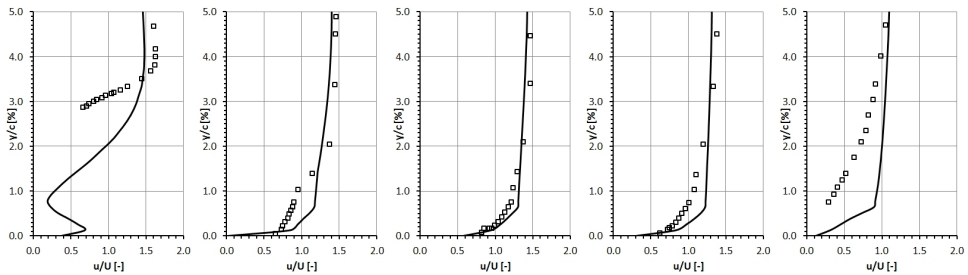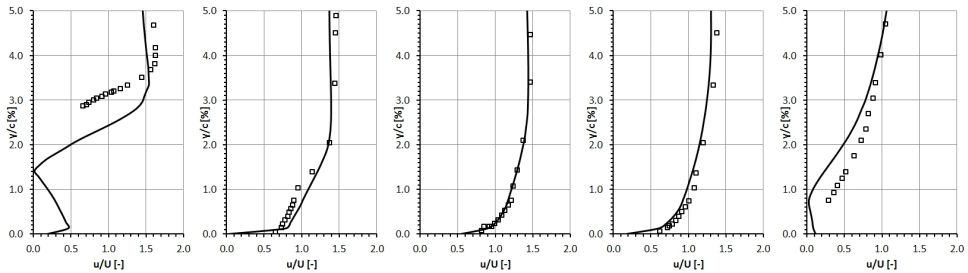(b) Setup 2

(c) Setup 3

(d) Setup 4

Figure 5.24: Measured and computed pressure coefficients for Wilkinson testcase
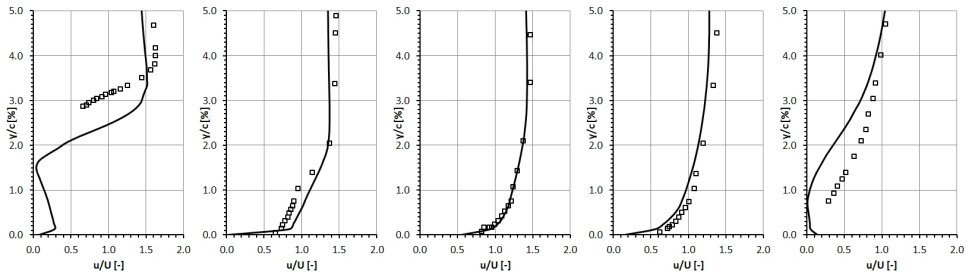
(a) Setup 1

(b) Setup 2

(c) Setup 3

(d) Setup 4

Figure 5.25: Measured and computed relative velocities at five cuts near the sail's surface, leading edge left. Normalised velocities are given on the abscissae, normalised wall distance on the ordinates.
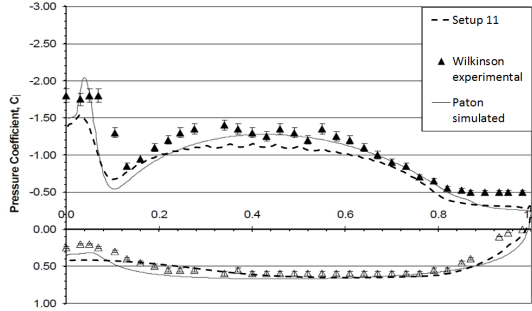
Figure 5.26: Comparison of pressure coefficient as measured (triangles), as computed by *Paton* (continuous) and as computed using setup 1 (dashed).
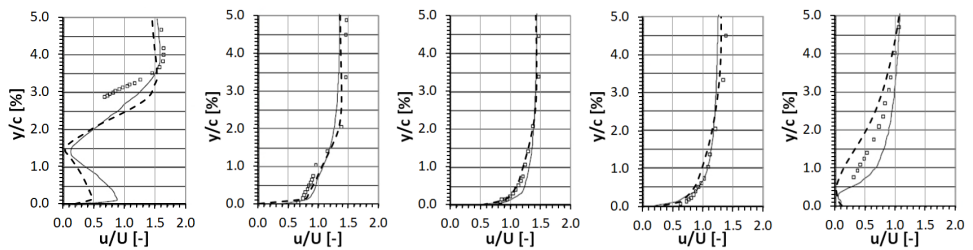
Figure 5.27: Comparison of relative velocity as measured (squares), as computed by *Paton* (continuous) and as computed using setup 1 (dashed) at five lines near the surface, leading edge left.

can be observed for both computations, with resulting values from setup 1 being slightly closer to measurements for the majority of the chord length.

The boundary layer velocity cuts (Figure 5.27) show close agreement with measurements for both computations in the region of attached flow (cuts 2 to 4). Near the leading edge (cut 1) *Paton's* results show better quantitative agreement in the outer regions ($y/c > 0.035$) while the trend is captured better by the computation using setup 1. Near the trailing edge (cut 5) *Paton's* results show too little flow separation, while it is over-estimated by the computations using setup 1.

The difficulties in predicting spontaneous flow separation on a curved surface using RANS methods are well documented in literature and an ongoing topic of research (see e.g. *Iaccarino et al.* [11] or *Xiao et al.* [12]). Judging from the results given in literature it seems that the main reason is the simplification of not resolving turbulent structures inherent to all RANS methods. This effect does not seem to be limited to turbulence models based on the Boussinesq approximation of isotropic turbulence but affects models calculating anisotropic turbulent viscosity as well. A possible remedy might be found in using models belonging to the *Large Eddy* (LES) family aimed at actually resolving the turbulent structures. Such models were not investigated here due to currently not being of practical interest to sail design due to excessively long computational times.

The above results indicate that, while still not perfect, the best results can be achieved using second order discretisation of the advective term, the SST-turbulence model and 5% turbulence level. These findings are used for the validation of three-dimensional flow simulation below.

FLOW AROUND RIGID THREE-DIMENSIONAL SAIL

To assess the accuracy of simulation of partially separated flow around an arbitrarily shaped three-dimensional body, results of simulations of the flow around a setup of a boat with mainsail and spinnaker at an apparent wind angle (*AWA*) of 90° are compared to those from wind tunnel tests. Similarity of investigated geometries is ensured by capturing the tested geometries under windload by photogrammetry (*Graf et al.* [13]), see Figure 5.28 .

The flow around model and sails is simulated using ANSYS-CFX. The computational domain extends 1.7 times model heights upwind of the model, 2.8 times downwind and 1.7 times upwards. The domain is discretised by an unstructured tetrahedron-prism grid. The sails are modelled as infinitely thin surfaces, shaped according to the geometries measured during the wind tunnel tests. The incident flow profile is based on that measured in the wind tunnel. Figure 5.29 shows the measured velocities and the polynomial fit applied to it for the simulations, *AWS_TFWT* is the measured velocity profile in the wind tunnel, *AWS_CFD* and *AWA_CFD* are the idealised incident velocity and flow angle used in the simulation. The setup is based on the findings of above cases and described in Table 5.12. Experimental and computed results are given in Table 5.13.

Because the computed lift area shows a strong deviation from the measured result, an issue with the correct prediction of flow separation might be present. A closer look at the pressure distribution on the sail (Figures 5.30) shows suction side pressure coefficients close to -1.00 over major parts of the chord. This indicates the presence of mostly separated flow on the leeward side, whereas large areas of attached flow were observed
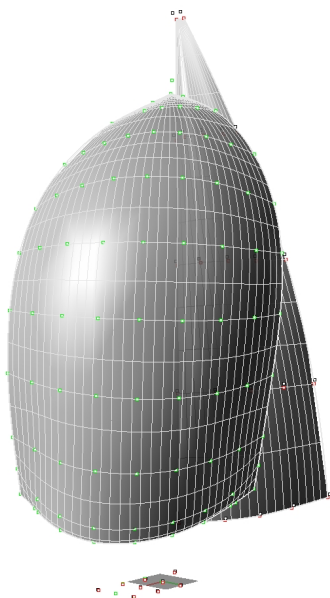
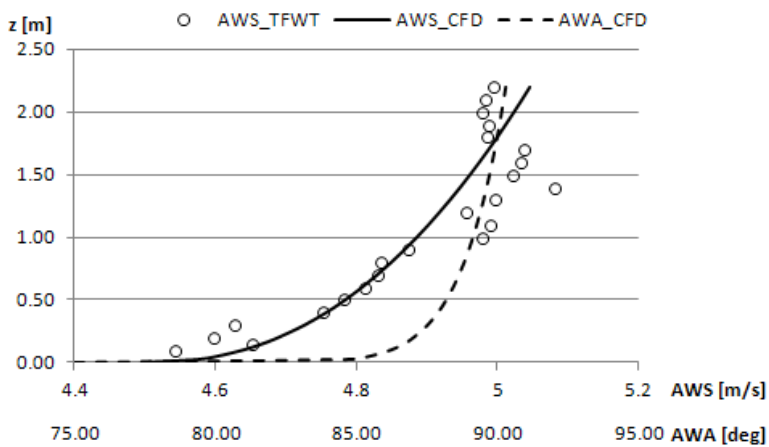Figure 5.28: Measured flying shape.

Figure 5.29: Polynomial fit to measured incident flow properties.

Incident Flow	According to polynomial
Turb. Mod.	SST
Turbulence Intensity	5%
Discretisation Order	2nd
Estimated y^+	1
dt	0.025s

Table 5.12: Simulation setup for validation of 3D-flow around fixed geometry

	Lift Area	Drag Area
	[m^2]	[m^2]
Measured	1.763	1.334
Calculated	1.644	1.328
Deviation	-5.62%	-0.45%

Table 5.13: Measured and calculated force areas at AWA = 90°

during the wind tunnel tests at an AWA of 90°. This might be an explanation for the large differences in simulated and measured lift force area (lift force normalised by dynamic pressure).

As, due to the twisted incident flow, some doubt about the actual flow direction in the wind tunnel is present - to which the sails adjust in the experiment due to flexibility -, the simulation is repeated at an AWA of 85° using the same geometry to assess the sensitivity of the results to inflow conditions. Table 5.14 gives a comparison of the achieved lift and drag areas in experiment and simulation. The computed results at the modified incident flow angle of 85° indicate slightly larger lift and drag areas than the measurements. This supports the assumption that too much flow separation is present in the simulation at 90° incident flow angle, respectively of an angle offset.

This issue indicates a strong sensitivity of the computed flow to accurate representation of incident flow and geometry. Especially due to the sharp leading edge, a small deviation may already trigger flow separation close to the leading edge. As neither the flow nor the geometry are measured as a continuum but only at a limited number of locations this may well have happened here.

	Lift Area	Drag Area
	[m^2]	[m^2]
Measured	1.763	1.334
Calculated AWA 90°	1.644	1.328
Calculated AWA 85°	1.788	1.342
Deviation AWA 85°	+1.42%	+0.60%

Table 5.14: Measured and calculated force areas at AWA = 85 & 90°

Figures 5.31 give the pressure coefficients over chord length at various mitre girth fractions for AWA 85° as well as measurement data kindly provided by *Dr. Viola* from experiments conducted for his publications ([14, 15]).While the computed pressure distribution at the lowest chord (1/4) looks very much the same as at AWA 90°, comparing the data for the other mitre girth fractions at AWAs 90° and 85° indicates significantly more attached flow in he case of the latter. Figures 5.32 and 5.33 show the wall shear magnitude and direction on the suction (leeward) side at AWAs 90° and 85°. The shear vectors in the case of AWA 90° indicate mostly reversed, therefore separated, flow on most of the sail's area. In contrast, the shear vectors in the 85° case show a very specific pattern, indicating attached flow over 2/3 of the girth in the lower regions with increasing separation moving upwards.

The experimental results depict local pressure coefficients measured on a flat cut asymmetric spinnaker at AWA 55°. Unfortunately, no geometry is available to these pressure measurements. Due to the difference in geometries and AWAs only a qualitative comparison of pressure distributions is possible.As can be expected from the different sail designs and test conditions the measured pressures indicate significantly more attached flow on the suction side of the sail but general patterns are quite similar.

Conclusion

The results of the validation exercise on two- and three-dimensional flow support the findings of the corresponding verification exercise, namely the difficulty in correctly predicting separation behaviour on a highly curved geometry. This is examplified by the deviation of computed from measured results in the two-dimensional case, and the variation thereof, depending on setup. While the salient features of the pressure distribution and the velocity profile close to the sails surface are all visible in the best setup, some quantitative difference is still apparent.

The results of the three-dimensional case further show the sensitivity of results to parameters like incident flow angle and precision of geometry capturing respectively, especially on a geometry with such a sharp leading edge. While no satisfactory agreement is reached in the case based on the actual measurements, the results achieved by a slight variation of incident flow angle are very close to the measured forces and observation from the experiments.

Still, the capabilities of the flow simulation method have been shown and can be considered to be satisfactory for the intended use as indicated by maximum deviation to experimental results of about 5%.

5.3.3. Fluid-Structure-Interaction Simulation Method

The entire fluid-structure-interaction method is validated by correlating simulation results for a spinnaker of known design shape to corresponding experimental data. Generated forces and moments and flying shape are compared directly. Sails and measured flying shapes are the same as in Section 5.3.2. As no facilities for flow or pressure measurements during the experiment were available, correct pressure distribution is implicitly assumed if the flying shape is computed correctly. This approach is based on the assumption of the sail having negleglible bending stiffness and therefore direct correlation between pressure distribution and flying shape.
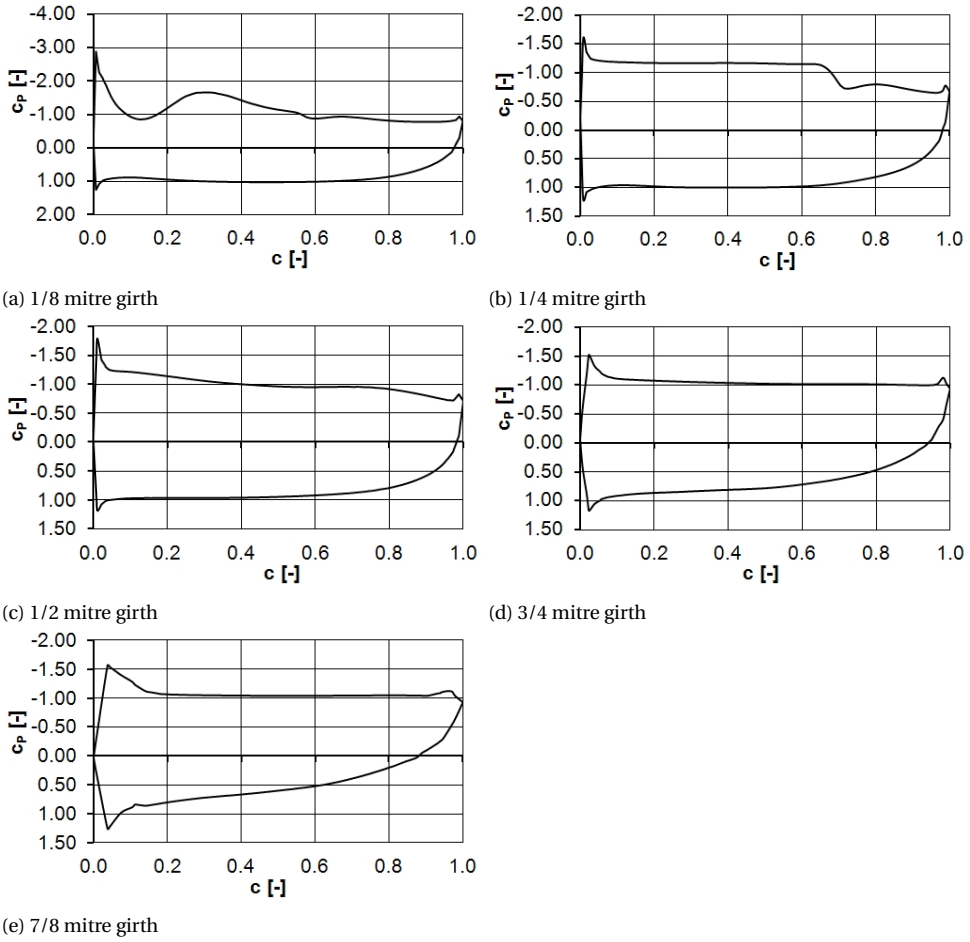
(a) 1/8 mitre girth

(b) 1/4 mitre girth

(c) 1/2 mitre girth

(d) 3/4 mitre girth

(e) 7/8 mitre girth

Figure 5.30: Pressure coefficient c_P over normalised chord c on spinnaker at various heights at AWA 90°

(a) 1/8 mitre girth

(b) 1/4 mitre girth

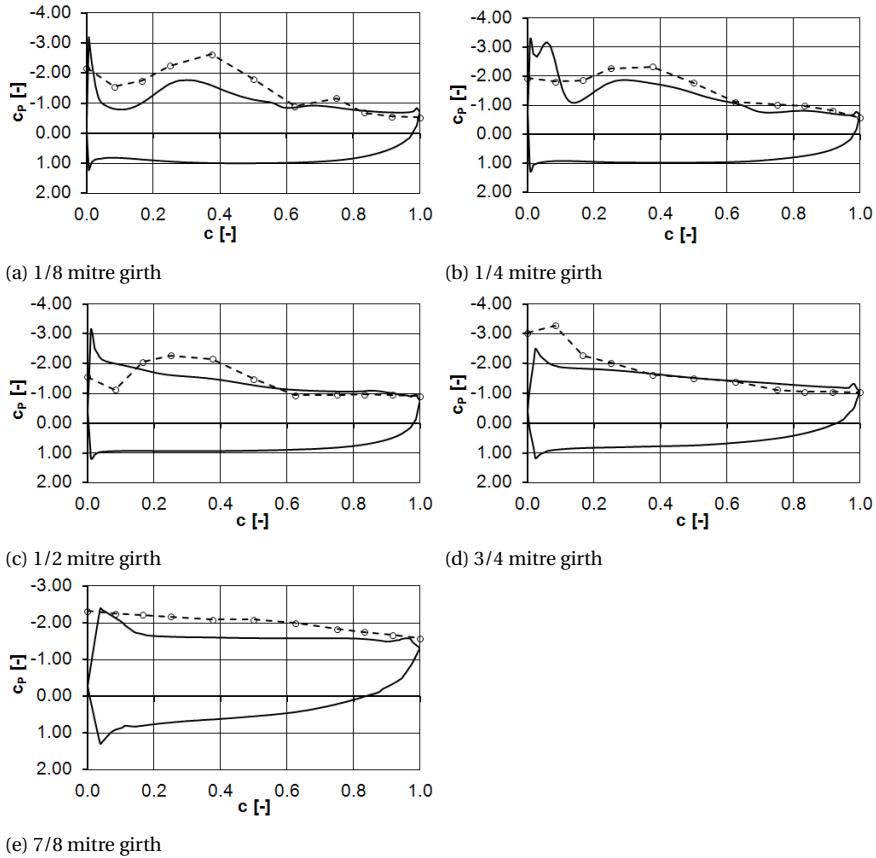(c) 1/2 mitre girth

(d) 3/4 mitre girth

(e) 7/8 mitre girth

Figure 5.31: Comparison of computed (continuous) and measured (by *I. M. Viola*) (dashed) pressure coefficients c_P over normalised chord c at various heights at AWA 85°
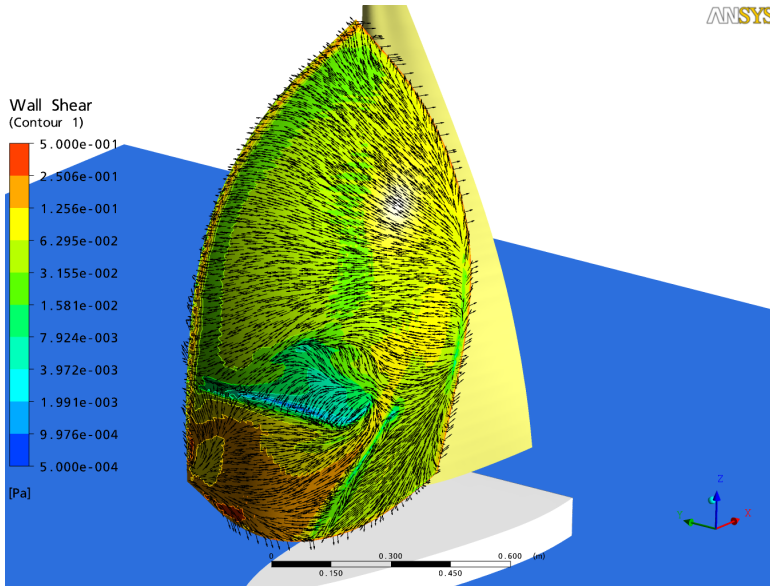
Figure 5.32: Wall shear magnitude and direction, suction side at AWA 90°
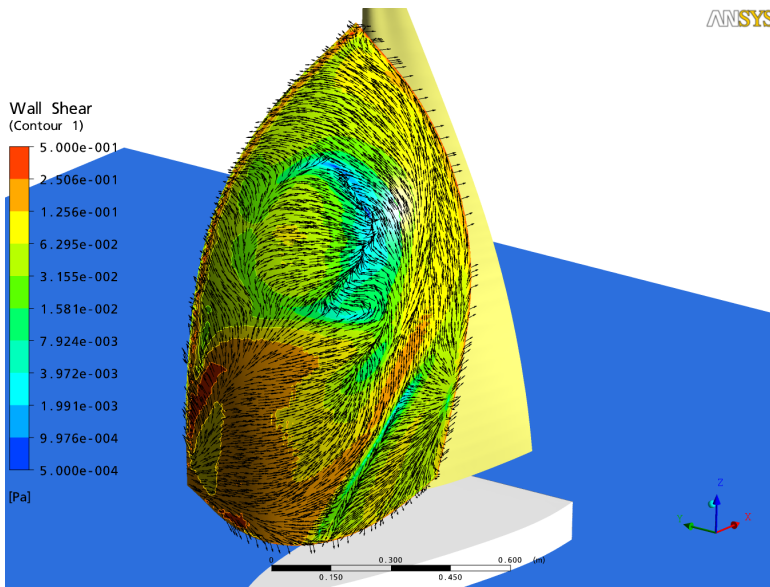
Figure 5.33: Wall shear magnitude and direction, suction side at AWA 85°

The flow around the setup of hull mainsail and spinnaker as well as the structural behaviour of the spinnaker are modeled. AWAs range from 90° to 180° in steps of 15°. The incident flow field is based on measurements of the actual wind tunnel flow field without a model present, as above.

Material properties of the spinnaker are taken from the cloth manufacturer's product literature. To improve computation speed, the materials are assumed to be isotropic. The material properties are given in Table 5.15.

Application	Young's Modulus	Poisson no.	weight/unit area
[-]	[N/m^2]	[-]	[N/m^2]
Body of Sail	1.16E+05	3.00E-01	3.24E-01
Corner Patches	1.16E+06	3.00E-01	3.24E+00
Sheet (1mm Dia.)	1.568E+09		7.99E-03 [N/m]

Table 5.15: Material properties as used for simulation

The chosen domain size is the same as in Section 5.3.2, the grid parameters are based on the findings described in that section. First layer heights are determined to keep y$^+$ values between 1 and 4, in line with above findings. The time step is chosen to ensure an average Courant number of about 30 for the resulting flow in the entire domain, the reduction compared to above cases is necessary to keep the simulations stable. The detailed parameters are given in Table 5.16. Trim settings are applied to mainsail and spinnaker according to those recorded in the wind tunnel for each AWA. To ensure continuity of grid quality despite the deformation of the spinnaker, the spinnaker is pre-deformed by applying a constant pressure distribution and the actual trim settings. The grids are generated using these pre-deformed sails. The inherent material stresses due to this pre-deformation are taken into account during the FSI computations. Simulations are carried out over a computed time of six seconds, forces are averaged over the last second.

Domain size	8.00 x 7.00 x 3.00 m
No. of FE-Elements	1.248E+04
Max. cell size	256 mm
Max. element size	16 mm
Number of prism layers on sail	3
First layer height on sail	1.1 mm
Time step length	3.75E-03 s

Table 5.16: CFD-Setup for FSI-Simulation

SIMULATION RESULTS

Below the measured and computed forces and flying shapes are compared and evaluated. A comparison of measured and calculated forces, converted to lift and drag areas

AL and *AD* by normalisation by the dynamic pressure, is given in Figure 5.34. *TFWT* indicates measured, *FlexSail* simulated results. As can be seen, the trends found in the wind tunnel are captured well by the simulations, albeit with offsets of about 0.05 to 0.10 m^2. As can be clearly seen in Figure 5.34 two distinct regimes of lift and drag areas exist,
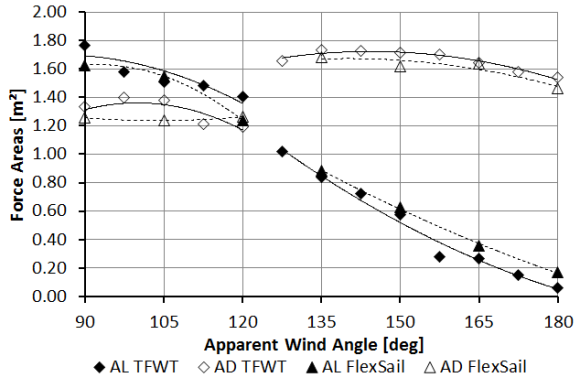

Figure 5.34: Lift and drag areas from wind tunnel tests and FlexSail simulations

separated at AWA = 120°. Below 120° simulated lift areas are slightly smaller than measured ones but showing the same trend with drag areas from simulation results being a bit smaller with varying offset. Above 120° the picture changes with the trends of simulated forces areas showing good agreement and simulated lift areas slightly larger and simulated drag areas slightly smaller than measured ones. The largest differences arise near 120°.

This behaviour is indicative of mostly attached flow below 120° and mostly separated flow above. Figure 5.35 shows the pressure distribution at an apparent wind angle of 90°, indicating mostly attached flow near the leading edge (indicated by strongly negative pressure). A gentle rise of pressure towards the trailing edge indicates mostly attached flow. Comparing these results to those shown in Section 5.2.3 indicates that the interaction between flow forces and structure has a corrective effect to establish attached flow where geometrically feasible, at least in this particular case.

In Figures 5.36 to 5.38 the measured and computed flying shapes at selected AWAs are shown. Similar to the computed and measured forces, the flying shapes at AWAs 90° and 150° show very close agreement with the largest deviations being about 1.9% of the respective edge. The largest difference can be found at AWA 120° where the profiles in the lower half of the sail differ quite significantly. The computed results indicate a much stronger suction peak near the leading edge, probably due to attached flow, while the rounded profile of the measured shape might indicate fully separated flow in this area. The deviations of the leeches and clew are given in Table 5.17.

Figure 5.39 gives an impression of the computed flying shape at AWA 90° with and without wrinkling model as well as the resulting principal stresses. The impact of the wrinkling model on the geometry, especially near the corners, can be nicely seen. The qualitative depiction of S_2 shows the effect of lack of wrinkling model with the associated
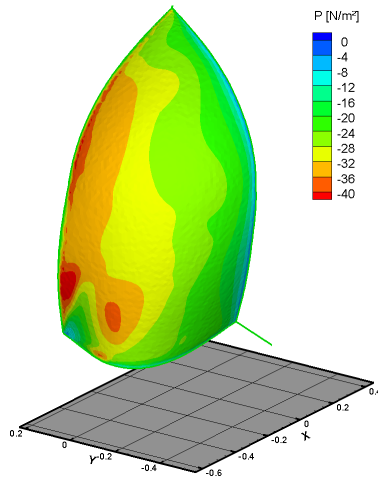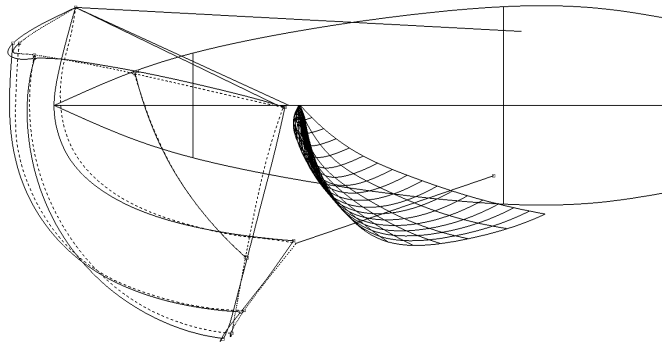
Figure 5.35: Pressure distribution on sail at AWA 90°

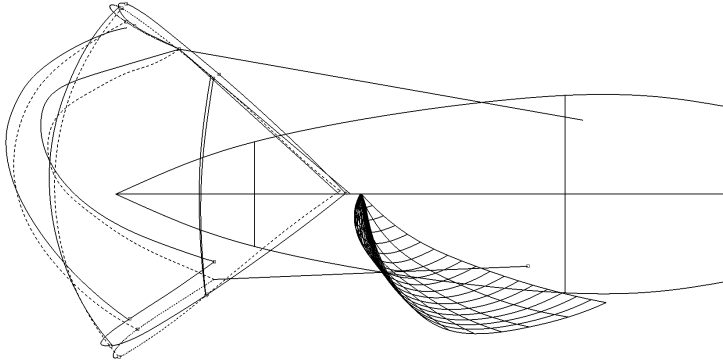Figure 5.36: Measured (dashed) and computed (continuous) flying shape at AWA 90°

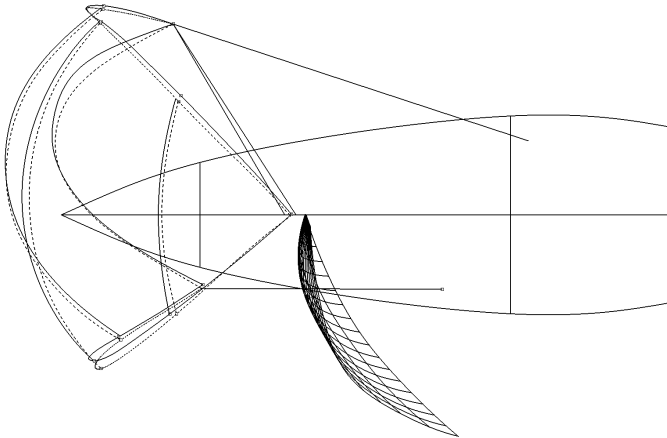Figure 5.37: Measured (dashed) and computed (continuous) flying shape at AWA 120°

Figure 5.38: Measured (dashed) and computed (continuous) flying shape at AWA 150°

AWA	Luff	Leech	Clew
90°	0.90%	1.63%	0.49%
105°	1.39%	2.16%	0.58%
120°	1.57%	2.41%	2.40%
135°	2.17%	1.66%	1.58%
150°	1.15%	1.86%	0.83%
165°	1.11%	2.34%	1.53%
180°	1.95%	4.52%	2.20%
Avg.	1.46%	2.36%	1.37%

Table 5.17: Max. deviation between measured and computed geometries in percent of leech length

impact on flying shape and S_1. This comparison strongly underlines the need to use a proper wrinkling model to compute a correct flying shape.

CONCLUSION

Due to the limitations of the measured data, only total forces and spinnaker flying shapes can be compared. Similarly to the findings on the simulation of flow around fixed geometries, good agreement of pressure distribution on the sail, as indicated by the flying shape, can be found for cases in either a mostly attached or mostly separated flow regime. Quite large deviations are present in cases with partially separated flow. The computed forces generally show quite good agreement to measured forces with the largest deviations arising in cases with partially separated flow as well. Judging from the results, a self-corrective effect is present to establish mostly attached flow in cases where it is feasible.

As the flying shapes and forces show a good agreement in most cases and the trends of the force measurements are well captured, this method can be considered suitable to support sail design decisions.

REFERENCES

[1] F. Stern, R. Wilson, and J. Shao, *Quantitative v&v of cfd simulations and certification of cfd codes,* International Journal for Numerical Methods in Fluids **50**, 1335 (2006).

[2] L. Eca and M. Hoekstra, *Code verification of unsteady flow solvers with the method of the manufactured solutions,* in *Proceedings of the Seventeenth (2007) International Offshore and Polar Engineering Conference* (2007).

[3] M. Stein and J. M. Hedgepeth, *Analysis of Partly Wrinkled Membranes,* Tech. Rep. (NASA, 1961).

[4] S. Wilkinson, *Partially Separated Flow Around Masts and Sails,* Ph.D. thesis, University of Southampton (1984).

[5] W. Rodi, *Comparison of les and rans calculations of the flow around bluff bodies,* Journal of Wind Engineering and Industrial Aerodynamics **69-71**, 55 (1997).
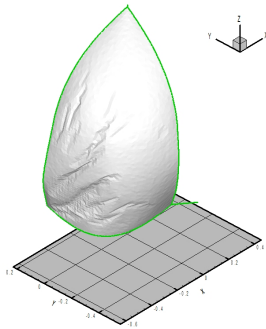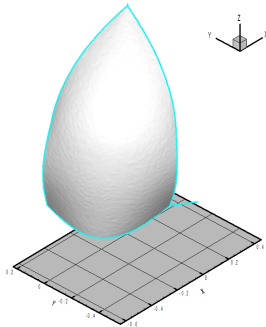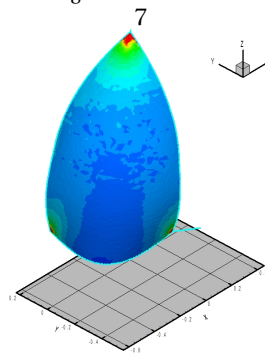
(a) flying shape without wrinkling model
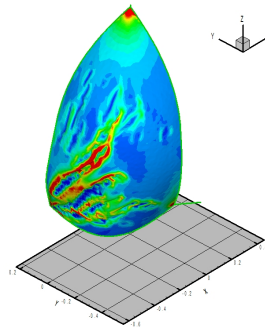
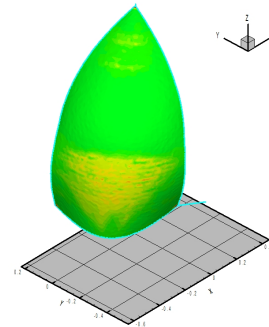(b) Principle stress S_1 without wrinkling model
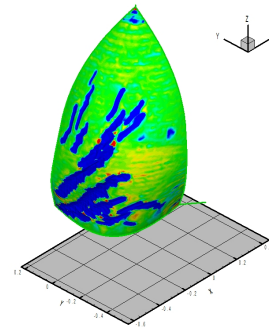
(c) Principle stress S_2 without wrinkling model

(d) flying shape with wrinkling model

(e) Principle stress S_1 with wrinkling model

(f) Principle stress S_2 with wrinkling model

Figure 5.39: Flying shapes and principal stresses with (bottom) and without (top) wrinkling model

[6] K. Lu, M. Accorsi, and J. Leonard, *Finite element analysis of membrane wrinkling,* International Journal for Numerical Methods in Engineering **50**, 1017 (2001).

[7] J. Pitkäranta, *The problem of membrane locking in finite element analysis of cylindrical shells,* Numerische Mathematik **61**, 523 (1992).

[8] S. J. Collie, M. G. Gerritsen, and P. S. Jackson, *A Review of Turbulence Modelling for use in Sail Flow Analysis,* Tech. Rep. (Department of Engineering Science, University of Auckland, 2001).

[9] J. Paton, H. Morvan, and P. Heppel, *Fluid structure interaction of yacht sails,* in *International Conference on Innovation in High Performance Sailing Yachts* (2008).

[10] D. Trimarchi, S. Turnock, D. Chapelle, and D. Taunton, *Fluid-structure interactions of anisotropic thin composite materials for application to sail aerodynamics of a yacht in waves,* in *12th Numerical Towing Tank Symposium* (2009).

[11] G. Iaccarino, A. Ooi, P. A. Durbin, and M. Behnia, *Reynolds averaged simulation of unsteady separated flow,* International Journal of Heat and Fluid Flow **24**, 147 (2003).

[12] Z. Xiao, Y. Zhang, J. Huang, H. Chen, and S. Fu, *Prediction of separation flows around a 6:1 prolate spheroid using rans/les hybrid approaches,* Acta Mechanica Sinica **23**, 369 (2007).

[13] K. Graf and O. Müller, *Photogrammetric investigation of the flying shape of spinnakers in a twisted flow wind tunnel,* in *19th Chesapeake Sailing Yacht Symposium* (2009).

[14] I. M. Viola, *Downwind sail aerodynamics: A cfd investigation with high grid resolution,* Ocean Engineering **36**, 974 (2009).

[15] I. M. Viola and R. G. J. Flay, *Force and pressure investigation of modern asymmetric spinnakers,* International Journal of Small Craft Technology, Trans. RINA **151** (2009).

6

APPLICATION

To demonstrate the capabilities of the method developed within the scope of this thesis, a series of designs for asymmetric spinnakers for a yacht according to the proposed AC90 rule [1] are investigated. This rule provides the design limits for the originally proposed type of yacht for the 33$^{\text{rd}}$ America's Cup, resulting in boats of 27.4m length, 23t displacement and an upwind sail area of about 500m^2. Among the distinguishing features of this design rule is the relative lack of constraints on spinnaker design. The only rules are the definition of tack line and halyard lead points, the prescription of asymmetric sail design and a maximum length of any edge of 50m. Compared to the usual constraints, limiting the measured sail area, this significantly opens up the design space, requiring its thorough evaluation. The main parameters of the proposed AC90 class are given in Table 6.1, the rig plan and description of the abbreviations is given in Figure 6.2.

Measured Length [m]	27.40
Beam [m]	5.30
Draft [m]	6.50
Displacement [kg]	23000
P [m]	35.50
E [m]	11.39
I [m]	30.20
J [m]	10.70
ISP [m]	37.85
JSP [m]	15.50
Sailarea$_{\text{Main}}$ [m^2]	300

Table 6.1: Relevant design paramters for AC90 class, abbreviations see Figure 6.2

6.1. GEOMETRY DEFINITION

To compare different spinnaker designs a generic setup of hull, rig and main sail according to the design rules is developed. Preparatory to the design of the spinnakers, for a range of true wind speeds (*TWS*) typical boat speeds (*uB*) and corresponding true and apparent wind angles (*TWA / AWA*) for optimal velocity made good (*VMG*) on downwind runs are determined using a velocity prediction program (*VPP*). Based on these apparent wind angles a baseline spinnaker design is developed. These design conditions are given in Table 6.2. Over a true wind speed range of 2 to 6 m/s the apparent wind angle changes just from 46° to 56°. Due to this limited range only one series of spinnaker designs has been investigated. A typical apparent wind profile is given in Figure 6.1

TWS	TWA	uB	AWS	AWA
[m/s]	[deg]	[m/s]	[m/s]	[deg]
2	138.97	2.98	1.95	46.12
4	138.94	5.64	3.68	49.48
6	140.57	7.67	4.81	56.35

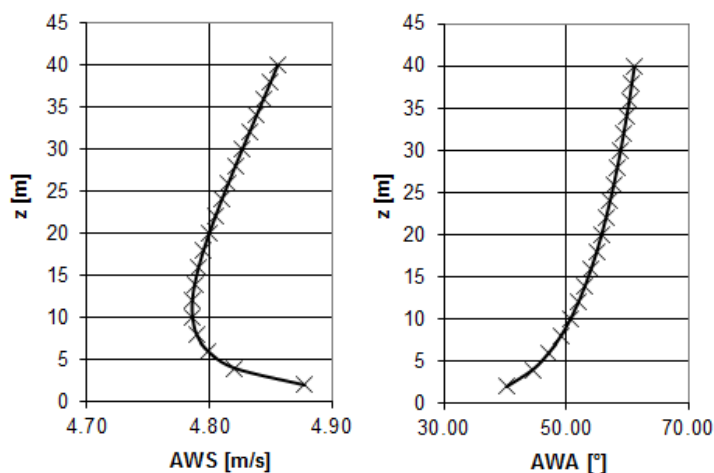Table 6.2: Design conditions for AC90 spinnakers

Figure 6.1: Apparent wind profile at TWS 6 m/s, TWA 140.6° and u_B 7.67 m/s

Starting from a parent design (see Figure 6.3), child designs are developed by systematically scaling the mid-girth. Leeches, mitre seam and curvature are faired towards head and foot, keeping the section shapes constant. The design parameters of the parent sail are given in Table 6.3, the variations in Table 6.4. The generated designs are shown in Figure 6.4.

The sails are assumed to be made from *Contender SK90* spinnaker cloth, the sheet is assumed to be *Gleistein Mega twin Dyneema*. The sail's corner patches are assumed to be built up of 10 layers of cloth. The material properties are given in Table 6.5.
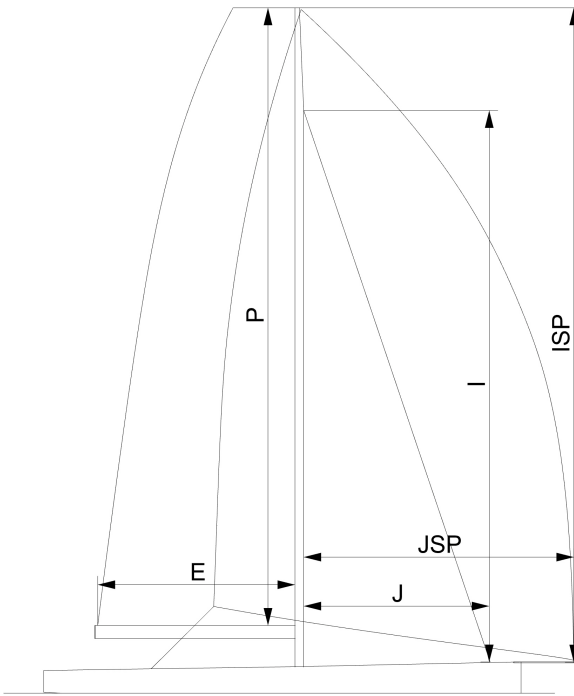
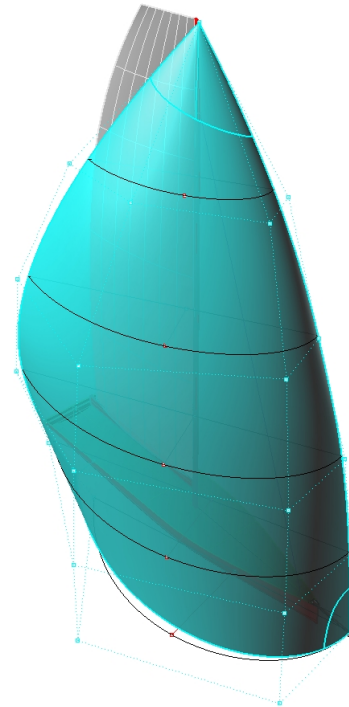Figure 6.2: Generic rig plan of AC90 yacht including main design parameters.

Figure 6.3: Parent design for AC90 spinnaker.

6.2. CALCULATION SETUP

The simulation setup is based on the one resulting from the V&V process (see Section 5.3.3), with incident flow conditions as given in Table 6.2 and Figure 6.1. The discretisation grid is generated based on the same inpu parameters, resuting in 1.8E+06 volume elements (tetrahedral and prism) with 8700 triangular elements on the spinnaker, see Figure 6.5. For simplification purposes the spinnaker is assumed to be of isotropic material with E*t = 130 N/mm^2. Following usual practice on high-performance boats with asymmetric spinnakers head, tack and lead position are assumed to be fixed with sail trim variation limited to systematic change of sheet length.

6.3. RESULTS

Figure 6.6 shows the resulting driving and side forces over sheet length for the various sail designs at TWS 6 m/s. Generally, three flow states can be observed: a too close-hauled spinnaker (left side of diagram) results in leeward separation close to the leading edge, together with a decrease of driving and side forces. An optimal sheeting of the spinnaker
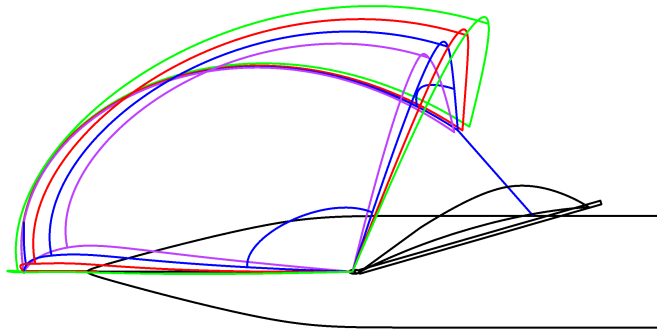
(a) Top
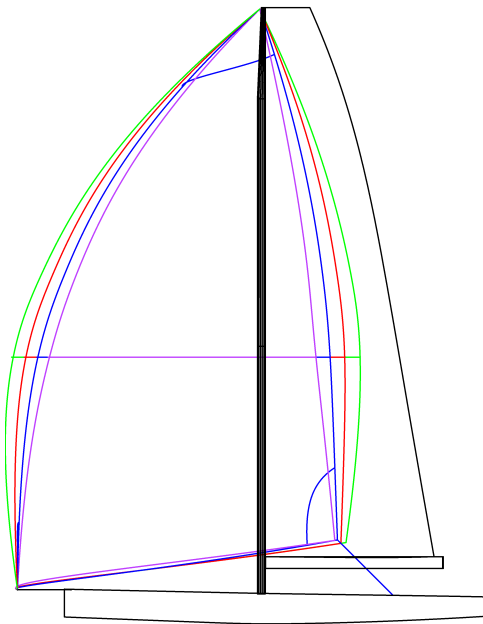
(b) Plan
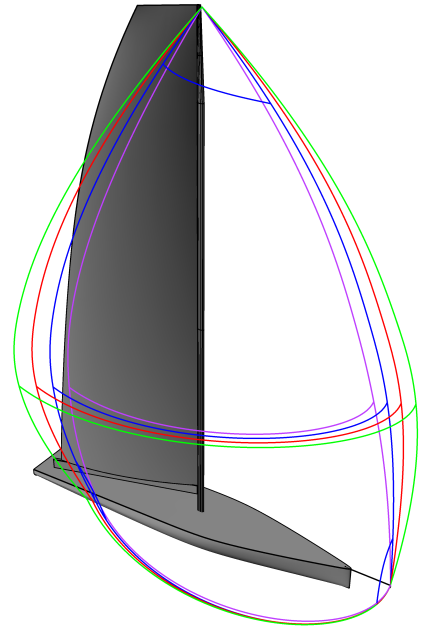
(c) Perspective

Figure 6.4: Parent (blue) and child asymmetric spinnaker designs

Luff [m]	42.230				
Leech [m]	38.862				
	Foot	1/4	1/2	3/4	7/8
girth [m]	27.117	25.349	21.014	11.774	6.093
chord [m]	21.956	21.974	18.897	11.030	5.778
camber [%]	29.65	23.30	19.53	14.91	13.36
tMax [%]	42.18	44.31	45.40	42.96	41.90
twist [deg]	0.00	7.63	12.53	14.03	14.58
entry angle [deg]	81.36	72.75	62.57	43.97	35.65
exit angle [deg]	51.00	45.21	38.92	23.59	18.89

Table 6.3: Design parameters of parent AC90 spinnaker

	Parent	Var 1	Var 2	Var 3
Luff [%]	100	101.02	102.19	99.17
Leech [%]	100	102.55	104.25	98.49
Foot [%]	100	101.00	102.35	99.44
1/4 girth [%]	100	107.14	115.59	93.59
1/2 girth [%]	100	109.83	118.28	90.85
3/4 girth [%]	100	109.15	115.55	90.05
7/8 girth [%]	100	109.16	114.21	89.61

Table 6.4: Parameter variations on AC90 spinnakers relative to parent design

6

results in attached flow at the luff, giving maximum driving force. A too open sheet will result in decreased forces due to windward separation at the luff, together with some luff curl. A conventional spinnaker will tend to collapse soon with an obvious rapid drop of driving force. However, the diagram shows only a smooth decrease of driving force. It can be concluded that, due to luff tension, these asymmetric spinnakers have a more stable luff and are less prone to collapsing than symmetric spinnakers. The diagram also indicates that the spinnaker with the largest mid-girth provides maximum driving force by a slight margin, though at the cost of the highest side force. Figure 6.7 gives the respective efficiencies of the sails, allowing an interesting comparison. While the largest spinnaker generates the highest driving force, the smallest is the most efficient. Comparing all four spinnakers, a strong dependency between forces, respectively efficiency, and mid girth is obvious. These differences and the necessity to haul the largest spinnaker significantly tighter than the smallest one indicate a much more prominent presence of separated flow.

Figures 6.8 show the resulting flying shapes and corresponding flow patterns from simulations at TWS=6m/s and various trims . In Figures 6.8a to 6.8c the effect of the different trim settings on the flow patterns is clearly visible. While the entrance flow at the luff of the optimally trimmed spinnaker is fully attached, one can clearly detect the separation on the windward side of the curling luff of the eased spinnaker. Similarly, on the
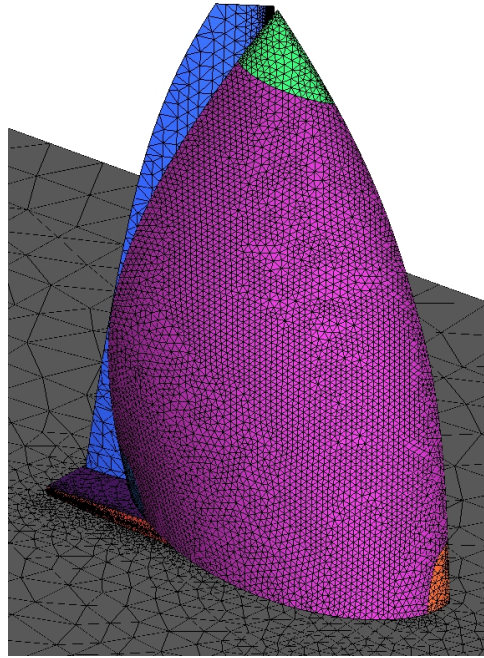
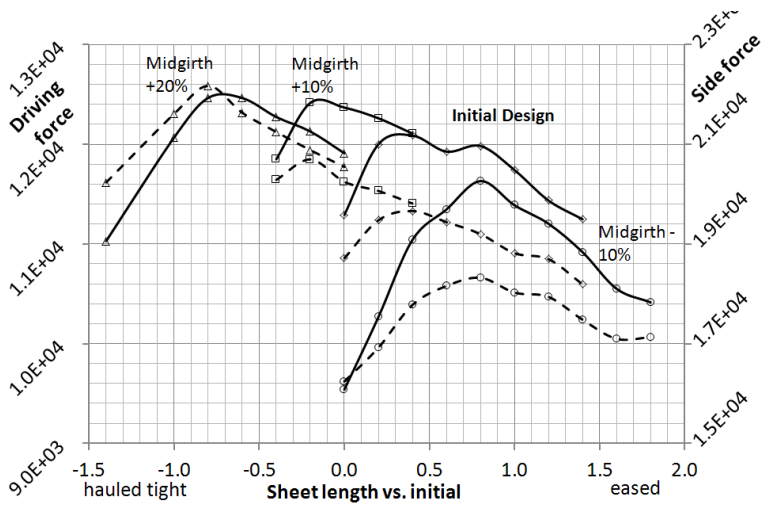Figure 6.5: Surface mesh on AC90 yacht, sails and water plane

6

Figure 6.6: Driving and Side Forces for the various spinnaker designs at 6 m/s TWS with trim variation

Contender SK90	
mass/area	48 g/m^2
E*t Warp	130 N/mm
E*t Fill	60 N/mm
E*t Bias	55 N/mm
Gleistein Mega Twin Dyneema	
Diameter	24 mm
mass/100m	39 kg
E	1.01E+03 N/mm^2

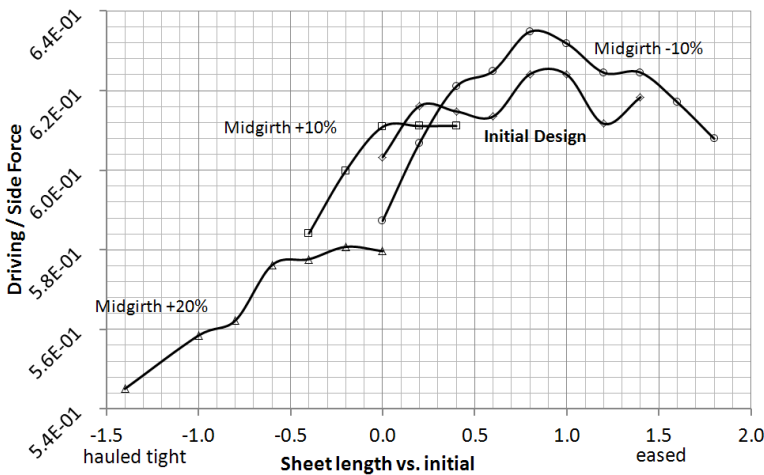Table 6.5: Material properties of spinnakers and sheets

Figure 6.7: Efficiency (driving by side force) for the various spinnaker designs at 6 m/s TWS with trim variation

close-hauled spinnaker, leeward flow separation at the luff is readily observable. While the slight loss of increased velocity near the luff in Figure 6.8b explains the slight loss in driving force due to easing the sheet, the leeward side flow separation in Figure 6.8c explains the dramatic loss of driving force and increase of side force due to sheeting the spinnaker too close. Figures 6.8d and 6.8e show flow and geometry detail near the luff at optimal and eased trim. In Figure 6.8d a nice section shape at the luff and clean incoming flow can be seen. In Figure 6.8e luff curl due to the eased sheet and corresponding windward side flow separation are present. Near the clew some macro-scale wrinkles (larger than element size), resulting from uni-directional stress in this area, can clearly be seen (see Figure 6.9 as well). Obviously, the shape and size of these wrinkles is - to some extent - determined by grid resolution and element orientation relative to these wrinkles.

(a) Optimal trim

(b) Eased

(c) Hauled

(d) Luff detail, optimal trim

(e) Luff detail, eased
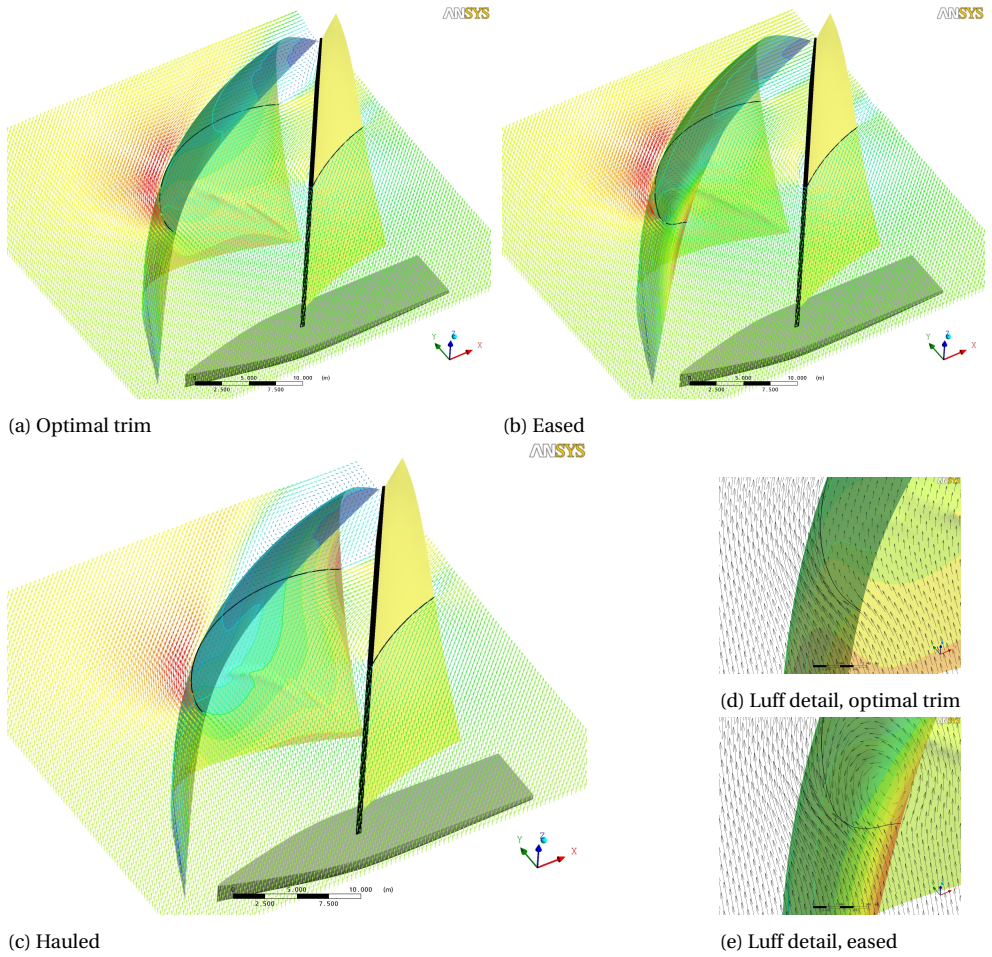
Figure 6.8: Flow patterns around spinnaker at different trim settings

(a) Macro-scale wrinkles

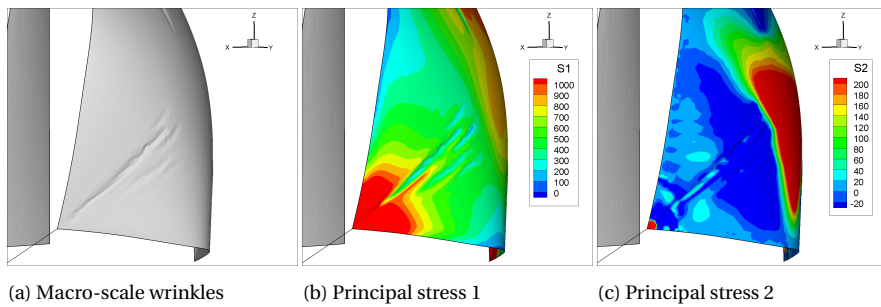(b) Principal stress 1

(c) Principal stress 2

Figure 6.9: Macro-scale wrinkles, resolved by grid

6.4. CONCLUSION

In the above study, the capabilities of the method for the evaluation of a range of sail designs as well as trim settings are demonstrated. The effect of spinnaker design as well as trim on generated forces resp. efficiency can clearly be seen in the corresponding force / efficiency plots. Further, the flow / geometry plots nicely show the effect of non-optimal trim on the flow and, in reverse, the effect of resulting flow forces on flying shape. The deformation of the sail's surface, especially the occurance of macro-scale wrinkles, gives valuable information on possible design improvements. The force / efficiency plots provide valuable guidance to the sail designer as well as trimmer regarding sail (design) selection and optimal trim settings.

REFERENCES

[1] A. M. S.A., *America's cup 90 class rule,* (2007), version 1.0.

6

7

CONCLUSIONS, RECOMMENDATIONS AND OUTLOOK

7.1. CONCLUSIONS

The present work was initiated to develop a novel method, compared to the present batch mode coupled approaches based on potential flow theory, to evaluate the properties of downwind sails at the design stage based on simulation of viscous flow as well as structural behaviour. With RANS-based viscous flow simulation methods gaining a strong foothold in industrial application and their capabilities increasing from pure flow simulation to include mesh motion and deformation, it was decided to couple an industrial RANS-solver to a purpose-written structural simulation code and evaluate the prospects of this combination to complement or replace wind tunnel experiments.

While couplings between flow and structural solvers, so-called Fluid-Structure-Interaction or *FSI* solvers were already in existence, their application was limited to upwind sails due to neglecting viscous effects in the flow solution. In the present method this shortcoming has been rectified by employing a flow simulation method based on the solution of the Reynolds-averaged Navier-Stokes equations, in principle capable of simulating partially or fully separated as well as attached flow. Within this study, these particular capabilities of the selected flow simulation method are thoroughly evaluated as part of the verification and validation (*V&V*) exercise.

As no structural solver capable of simulating the structural behaviour of flexible, possible partially slack, membrane structures was readily available, such a solver has been developed as part of this thesis (Chapter 3). Based on the classical CST-element, the element was extended by the capability to capture sub-element scale membrane wrinkling. A robust solution method has been implemented to solve the resulting system of equations. During the verification and validation exercise good agreement with experimental resp. analytical data has been shown, the importance of sufficiently fine grids has been clearly demonstrated. Further, the importance of a suitable wrinkling model has been demonstrated for the simulation of the kind of membrane structures investigated in this

thesis. Beyond the simulation of the structural behaviour of sails, this solver has since been successfully used on the simulation of sun shades and tent roofs.

To establish the coupling between the flow and the structural simulation methods a basic but robust data exchange method has been established (see Chapter 4). While, due to being explicit, this coupling is not suitable for the time-correct simulation of transient behaviour, good agreement between time-averaged experimental and essentially steady-state simulation results has been shown.

Preparing the V&V-phase it was found that detailed experimental data on flow around and structural behaviour of flexible sails was sadly scarce. To rectify this shortcoming an involved experimental series was undertaken at the YRU-Kiel twisted flow wind tunnel (see Section 5.1). The results have been published by the author [1] for further reference by other practitioners.

As part of the V&V exercise, the capabilities of a commercial RANS-solver to simulate the behaviour of partially separated flow were evaluated (see Chapter 5). Even though the results indicate shortcomings in the prediction of spontaneous flow separation, the results provide valuable indicators on generally suitable computational setups as well as the sensitivity of the flow simulation results to parameters such as grid resolution and time step length. It has been shown that, while quite some error is observable for quantitative force or local pressure values, trends like qualitative pressure or velocity distribution are captured quite well.

Finally, the applicability of the present method to practical sail design has been demonstrated (Chapter 6). A current 90' high performance monohull design has been chosen for this study, flow and structural behaviour have been evaluated at full scale. The present simulation method is used to evaluate a range of parametrical variations of a basic sail design including the generation of trimming information. The effect of the design variations on the usable apparent wind angle range as well as on optimal sail trim can clearly be seen from the results. Further, the effect of non-optimal trim on total forces resp. efficiency as well as on particular flow and structural behaviour can easily be evaluated from the results. Wind tunnel testing (at a scale of about 25 to 30) of said sail designs would have required the creation of scale models of boat and all sails and would have been affected by significant scale effects with regards to flow as well as structural behaviour. Full scale testing would only be possible on the finished boat and require the creation of huge (about 500m^2), expensive, quite possibly non-optimal, sails with the additional difficulty of usually non-repeatable non-laboratory conditions.

In total, in this thesis the development, verification and validation and application of a fluid-structure-interaction simulation method for possibly separated flow around highly flexible downwind sails is detailed. While various shortcomings are still evident, in general, the present method is a significant improvement with regard to more simple methods solely applicable to upwind sails, expecting fully attached flow and small deformations of the sails.

7.2. RECOMMENDATIONS AND OUTLOOK

As can be taken from above conclusions, the present simulation method still has some significant limitations and uncertainties. To further improve the simulations of flow and structural behaviour of downwind sails towards even more realistic results the following

steps are recommended:

- Further research and development work is needed on the improvement of flow simulation results for partially separated flows. The author is well aware that this issue is very much an ongoing topic of research as it affects a wide range of applications including, but not limited to, aerospace and car industries.

- *Large Eddy Simulations* or derivations thereof actually resolve the turbulence field and are supposed to be significantly more capable to correctly predict flow separation. While these methods are currently rendered impractical by their computational requirements, the continuous increase of computational power might resolve these issues in the near future.

- As the author could personally observe during actual usage, the behaviour of highly flexible downwind sails when trimmed for maximum driving force, especially at large apparent wind angles, is often quite dynamic. The current implementation of the coupling is not able to resolve these dynamics in a time-accurate manner. The practical value of computed results for these conditions would be significantly improved by implementing implicit or *strong* coupling for time-accurate prediction of transient behaviour.

- As the selection of available validation data is still limited, a public database containing results of experimental investigations by various practitioners / research establishments and on various geometries - two- as well as three-dimensional - would be desirable.

- In this thesis only the downwind sail is considered to be flexible. To assess the dynamics of the entire sailplan and rig, mainsail, mast and standing rigging would have to be included not only in the flow but in the structural calculation as well.

7

REFERENCES

[1] H. Renzsch and K. Graf, *An experimental validation case for fluid-structure-interaction simulations of downwind sails,* in *21st Chesapeake Sailing Yacht Symposium* (2013).

ACKNOWLEDGEMENTS

First, I would like to acknowledge the support generously given by Kai Graf at the Yacht Research Unit Kiel / University of Applied Sciences Kiel without whom this project would never have been possible.

I would also like to thank my supervisor René Huijsmans from Delft University of Technology for the time and effort he spent in guiding me through this work. He supported me to develop my own research, guided my scientific work and often pointed me towards relevant knowledge. Further thanks go to my co-promoter Mark Gerritsma for his support and guidance.

Furthermore, I would like to thank my colleagues at Yacht Research Unit Kiel, especially Christoph Böhm and Janek Meyer, for many inspiring and fruitful discussions.

Last but not least, my thanks go to Ralph Molenaar for translating the summary into Dutch.

A

VALIDATION DATA

A.1. PLANAR BENDING OF A PRE-TENSIONED BEAM-LIKE MEMBRANE

This validation case is based on a description given by *Stein et al.* [1]: A rectangular membrane is pre-tensioned by forces applied to its edges. Then equivalent and opposite moments are applied to its vertical edges. If the moments are applied as depicted in Figure A.1, wrinkles start to form at the lower edge from a moment depending on the pretension.
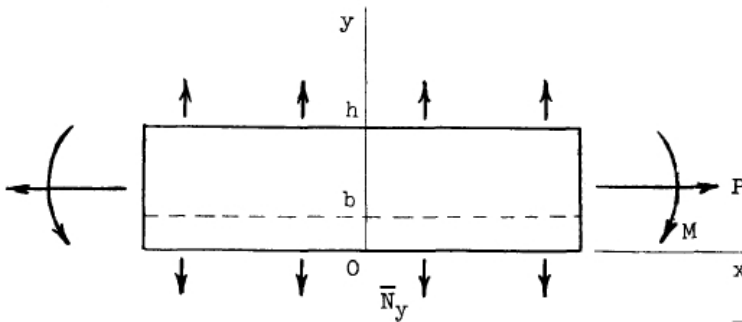

Figure A.1: Topology and applied forces and moments [1]

Stein et al. [1] (pp. 9 - 12) derive the following relation between curvature κ, pretension P and bending moment M:

$$\frac{2M}{Ph} = 1 - \frac{2}{3}\sqrt{\frac{2P}{\kappa E t h^2}}, \tag{A.1}$$

with the membrane thickness t. The amount of wrinkling can be calculated by:

$$\frac{b}{h} = 1 - \sqrt{\frac{2P}{\kappa E t h^2}}. \tag{A.2}$$

Such a setup, as shell-like structure, can be calculated as a bending beam with the following relation between curvature and bending moment, regardless of pretension:

$$\frac{M}{EI} = \kappa, \tag{A.3}$$

with κ being the curvature. With the sectional moment I being

$$I = \frac{h^3 t}{12}, \tag{A.4}$$

this yields the following relation for the normalised bending moment:

$$\frac{2M}{Ph} = \frac{1}{3} \frac{\kappa E t h^2}{2P}. \tag{A.5}$$

A.2. BENDING OF A PRESSURISED MEMBRANE CYLINDER

This validation case is based on a description given by *Stein et al.* [1] as well: An analytical solution is given for the bending and wrinkling behaviour of a pre-tensioned, pressurised tube subjected to a bending moment (Figure A.2). Even though experimental tests have been conducted, no experimental results are given in literature.
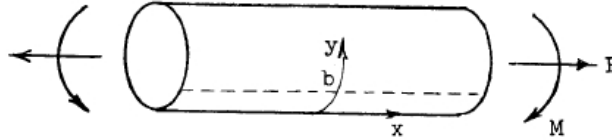

Figure A.2: Topology and applied forces and moments [1]

The formulations given by *Stein et al.* [1] (pp. 13 - 18) are as follows: For a cylinder of radius r and material thickness t, the state of the membrane is define by the axial pretension P, the internal pressure p and the bending moment M. The amount of wrinkling occurring is described by the ratio of circumference of wrinkling and radius b/r.

The following analytical relations are given for required pre-tension P and bending moment M depending on curvature κ and amount of wrinkling b/r:

$$P = 2Etr^2\kappa\left[sin\frac{b}{r} + \left(\pi - \frac{b}{r}\right)cos\frac{b}{r}\right], \tag{A.6}$$

$$M = Etr^3\kappa\left(\pi - \frac{b}{r} + \frac{1}{2}sin\frac{2b}{r}\right). \tag{A.7}$$

From classical engineering theory for a shell-like structure bending moment M would be:

$$\frac{M}{EI} = \kappa,$$ (A.8)

with the sectional moment I for a thin-walled tube being:

$$I = \pi r^3 t.$$ (A.9)

A.3. WILKINSON TESTCASE

In 1984 *Wilkinson* tested a two-dimensional sail-like geometry with mast in front in the 7' x 5' high speed section of the No. 1 wind tunnel of the University of Southampton (UK) [2]. The tests were designed to get an accurate measurement of flow separation and reattachment phenomena on a sole mainsail in upwind condition in the presence of a mast. During these tests the chord-wise pressure distribution and boundary layer velocity profiles in several locations were recorded. As a sail-like profile the NACA a=0.8 mean line, belonging to the NACA six-series wing sections [3], was chosen to ensure comparability to tests carried out by *Milgram* [4]. A circular mast in front of the sail was added to replicate a typical mainsail setup. The sail has a chord length C of 0.70m and a camber of 12.5% C. The mast has a diameter of 4.03% C. The sail is rotated (eased) by 5° relative to the boat's centreline, its angle of attack is 5°. The Reynold's number based on the sail's chord length is 600000. The relative pressure is given along the chord of the sail, boundary layer velocity profiles are given at five locations along the chord as shown in Figure A.3.
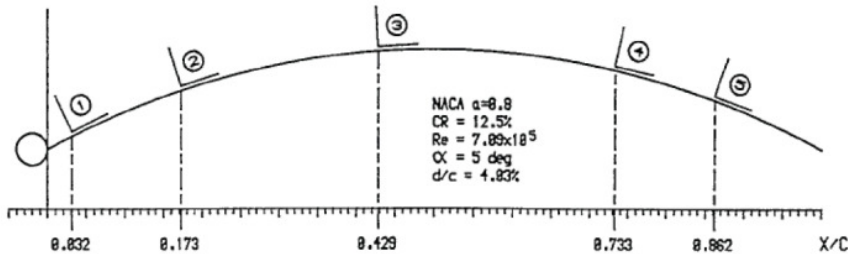

Figure A.3: Schematic description of Wilkinson test-case and measurement points [2]

As a result of these measurements Wilkinson found a typical flow pattern which he characterised by the nine zones shown in Figure A.4.

These zones are described as:

I : Upper mast attached flow

II : Upper separation bubble

III : Upper reattachment

IV : Upper airfoil attached flow

V : Trailing edge separation

VI : Lower mast attached flow

VII : Lower separation bubble

VIII: Lower reattachment
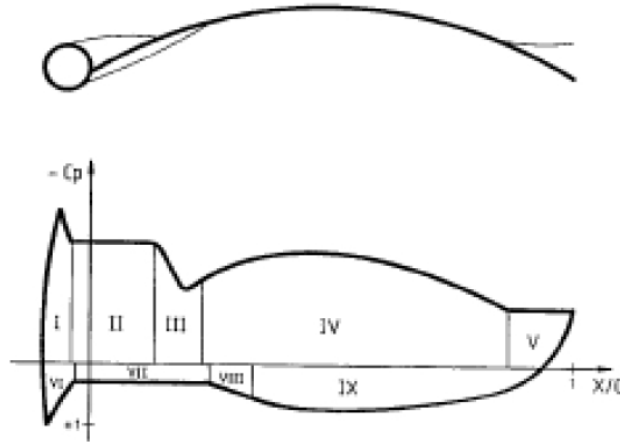
IX : Lower airfoil attached

Figure A.4: Nine zones of flow around mast-sail combination as characterised by *Wilkinson* [2]

Static pressure distribution was measured by three parallel chordwise rows of 40 pressure taps both on the upper and lower side of the sail. Further eight pressure taps were distributed around the mast at mid-span. Dynamic pressure measurements to evaluate the boundary layer profile on the suction side were taken by three-tube yaw probe. This yaw probe was traversed chordwise as well as normal to the sail's surface by a miniature robot to ascertain accurate probe location as well as a minimum of flow disturbance. The experimental setup is shown in [2].

In Figures A.5 to A.7 (taken from *Wilkinson* [2]) the measured pressure distribution as well as the boundary layer velocity profiles calculated from the dynamic pressure are shown for the case described above (AoA = 5°). The comparison of pressure distributions at different Reynolds numbers indicates negligible influence of the Reynolds number on the results (Figure A.5). The zonal model as described above(Figure A.4) corresponds well to the boundary layer profiles (Figures A.6 and A.7).
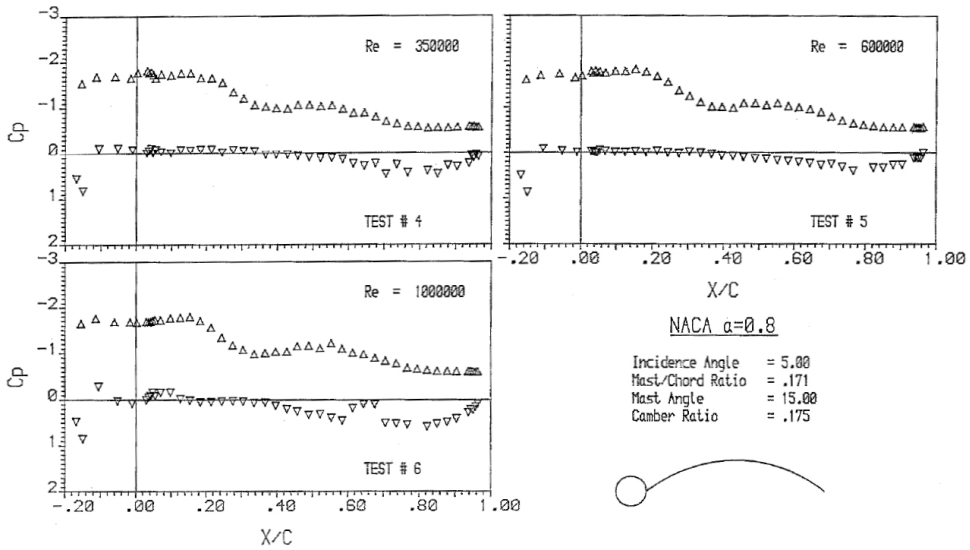
Figure A.5: Pressure distribution on sail section measured by *Wilkinson* at various Reynolds numbers [2].
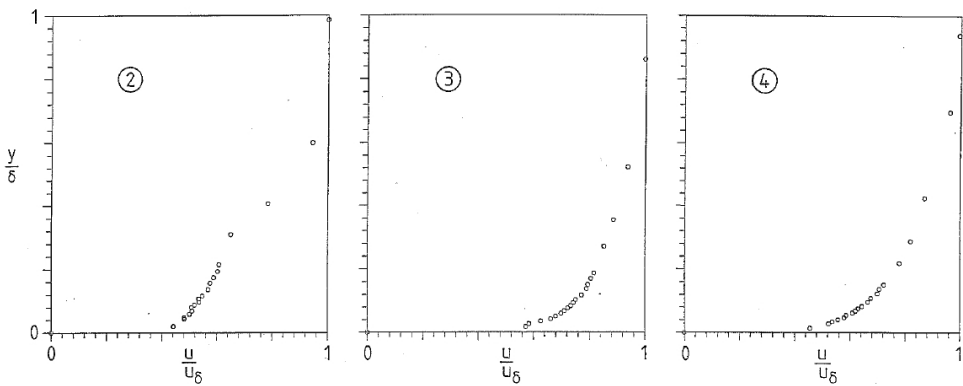

Figure A.6: Normalised boundary layer velocity profile in regions with attached flow as measured by *Wilkinson* [2].
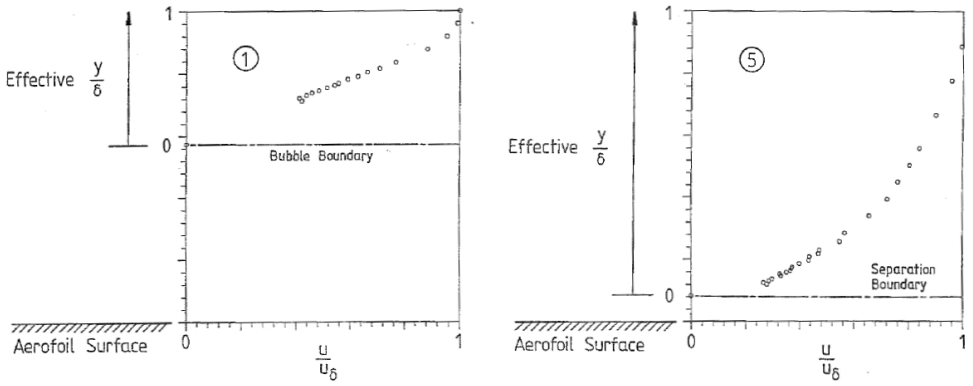
A

Figure A.7: Normalised boundary layer velocity profile in regions with separated flow as measured by *Wilkinson* [2].

B

FLOW SIMULATION METHOD

Coupled in a Fluid-Structure-Interaction method, the flow simulation is not only needed to calculate the flow around the geometry and global forces, but also the local pressure and shear forces used to generate the external forces for the structural loadcase. This places a special emphasis on the correct prediction of local phenomena like flow separation and reattachment locations.

The simulation of the viscous flow around sails in downwind conditions is a particularly challenging problem in the area of flow simulation. At the Reynolds numbers typical for the flow around sails (1E+06 < Re < 1E+07), the air can be assumed incompressible and isothermal, but the boundary layer has to be taken into account. The flow around the sails in these conditions is characterised by partial, often time dependent, separation on the highly curved surface. The occurrence and behaviour of this flow separation is highly dependent on the boundary layer.

The boundary layer on a sail typically has a laminar area near the leading edge, followed by a laminar separation bubble, transition to turbulent flow and reattachment as turbulent boundary layer flow. Turbulence is characterised by a constant change of flow velocity, direction and pressure in space and time. In principle this can be modelled using a *Navier-Stokes* equation approach. In practice resolving the flow to model all turbulent length and time scales, *Direct Numerical Simulation (DNS)* is, for the typical Reynolds numbers of interest, impossible due to the computational effort necessary.

For this reason typically the turbulence is modelled in a time and space averaged way using *turbulence models*. This approach yields the *Reynolds Averaged Navier-Stokes (RANS)* equations. The following description of the flows simulation method closely follows the description given in the *CFX Solver Theory guide* [5].

B.1. NAVIER-STOKES EQUATION THEORY AND REYNOLDS AVERAGING

The flow around the geometry is simulated by solving the Reynolds Averaged Navier Stokes Equations (RANSE) for the surrounding fluid. Basically, these are transport equa-

tions for mass, momentum and energy within the fluid. In the case of an incompressible, isothermal fluid, as assumed in this case, the equations can be somewhat simplified, variation of density and thermal energy do not need to be taken into account.

In a stationary coordinate frame the equation for the conservation of mass for an infinitesimally small volume can be written as:

$$\nabla \cdot \mathbf{U} = 0 \tag{B.1}$$

(B.1) states that all fluxes are balanced so that no mass can be lost or created. $\mathbf{U}$ is the velocity vector, ∇ is the partial derivative by the coordinate axes in a Cartesian system.

Similarly the Navier-Stokes equation for the conservation of momentum can be written as:

$$\frac{\partial(\rho\mathbf{U})}{\partial t} + \nabla \cdot (\rho\mathbf{U} \otimes \mathbf{U}) = -\nabla p + \nabla \cdot \tau + \mathbf{S}_M \tag{B.2}$$

With $\mathbf{U}$ being the same as above and ρ the density of the fluid (assumed to be constant in this case). p is the pressure, τ the stress tensor acting on the boundaries of this volume and $\mathbf{S}_M$ any other momentum source acting on the volume. On the left hand side of (B.2) the convective term depicts the transport of momentum. On the right hand side the diffusive term depicts the pressure, friction and other body forces acting on the fluid. The equation states that no momentum can be lost or generated, only transferred.

The stress tensor τ is related to the shear strain rate by

$$\tau = \mu\left(\nabla\mathbf{U} + (\nabla\mathbf{U})^T - \frac{2}{3}\delta\nabla \cdot \mathbf{U}\right) \tag{B.3}$$

with μ being the dynamic (molecular) viscosity. δ is the Kronecker Delta or Identity Matrix.

As stated above, turbulence is basically a chaotic state of fluid motion. To accurately simulate turbulent flow, it would be necessary to resolve the turbulent structures in space and time. As the computational effort for this is prohibitive, the fluctuations of velocity and pressure due to turbulence are averaged over time, called Reynolds Averaging. This is done by separating average and fluctuating parts of velocity by

$$U_i = \overline{U}_i + u_i \tag{B.4}$$

U_i denotes the actual velocity, $\overline{U}_i$ the temporal average and u_i the fluctuation. Similarly the pressure is averaged. The averaged component of the velocity is given by

$$\overline{U}_i = \frac{1}{\Delta t} \int\limits_{t}^{t+\Delta t} U_i \, dt \tag{B.5}$$

Δt is a timescale which is large relative to the timescale of the fluctuation to average but small relative to the timescale to which the equations are solved.

Substituting the averaged quantities into the original transport equations ((B.1) and (B.2)) yields

$$\frac{\partial}{\partial x_j} U_j = 0 \tag{B.6}$$

$$\frac{\partial \rho U_i}{\partial t} + \frac{\partial}{\partial x_j} \left(\rho U_i U_j \right) = -\frac{\partial p}{\partial x_i} + \frac{\partial}{\partial x_j} \left(\tau_{ij} - \rho \overline{u_i u_j} \right) + S_M \tag{B.7}$$

where τ is the molecular stress tensor (including normal and tangential stress components). The bars denoting averaged quantities are dropped in both above equations, except for the products of fluctuating quantities. In (B.7) the turbulent flux terms $\rho \overline{u_i u_j}$, the Reynolds stresses, are contained in addition to the molecular diffusive fluxes. These Reynolds stresses are unknown at this point, therefore (B.7) lacks closure. During the process of closure, an assumption has to me made regarding the instantaneous quantities of the Reynolds stresses.

B.2. Turbulence Modelling

The effect of turbulence on flow and flow forces is modelled using turbulence models. These models present different ways to calculate the Reynolds stresses contained in (B.7). In general these models can be classified by two different approaches:

- Modelling the turbulence as isotropic by introducing an additional turbulent viscosity - *Eddy Viscosity Turbulence Models*

- Modelling the anisotropic transport of the Reynolds stresses - *Reynolds Stress Turbulence Models*

Commonly turbulence models based on the additional turbulent viscosity approach are used. Reynolds Stress turbulence models theoretically should give more accurate results for complex flow, practice shows that they are often not superior to more involved Eddy Viscosity turbulence models. However they require more computational effort.

B.2.1. Eddy Viscosity Turbulence Models

In 1877 *Boussinesq* [6] introduced the concept of modelling the Reynolds stresses by introducing the so-called eddy viscosity. This concept is based on the assumption that turbulence consists of small eddies which are continuously forming and dissipating, and in which the Reynolds stresses are assumed to be proportional to the mean velocity gradients. This approach is formulated in a manner analogous to the relationship of stress and strain tensors in a laminar Newtonian fluid:

$$-\rho \overline{u_i u_j} = \mu_t \left(\frac{\partial U_i}{\partial x_j} + \frac{\partial U_j}{\partial x_i} \right) - \frac{2}{3} \delta_{ij} \left(\rho k + \mu_t \frac{\partial U_k}{\partial x_k} \right) \tag{B.8}$$

where k is the turbulence kinetic energy, given by $k = \frac{1}{2} \overline{u_i^2}$ and μ_t the turbulent viscosity which must be modelled.

Inserting (B.3) and (B.8) into (B.7) yields:

$$\frac{\partial \rho U_i}{\partial t} + \frac{\partial}{\partial x_j} \left(\rho U_i U_j \right) = -\frac{\partial p'}{\partial x_i} + \frac{\partial}{\partial x_j} \left[\mu_{eff} \left(\frac{\partial U_i}{\partial x_j} + \frac{\partial U_j}{\partial x_i} \right) \right] + S_M \tag{B.9}$$

μ_{eff} is the effective viscosity given by $\mu + \mu_t$. p' is a modified pressure given by:

$$p' = p + \frac{2}{3} \rho k + \frac{2}{3} \mu_{eff} \frac{\partial U_k}{\partial x_k} \tag{B.10}$$

The last term in (B.10)

$$\frac{2}{3}\mu_{eff}\frac{\partial U_k}{\partial x_k} \tag{B.11}$$

involves the divergence of velocity and can be neglected for incompressible fluids (see (B.1)).

Two-equation turbulence models based on above Eddy Viscosity hypothesis are typically used in industrial flow simulation applications . Most common are the k-ε and k-ω turbulence models with the Shear Stress Transport (SST) model being a combination of both combining their individual advantages.

THE K-EPSILON TURBULENCE MODEL

Generally considered as the standard turbulence model for many industrial CFD applications, the k-ε turbulence model is based on the Eddy Viscosity assumption as formulated in (B.9). In this turbulence model it is assumed that the turbulent viscosity is linked to the turbulence kinetic energy and dissipation by the following relation:

$$\mu_t = C_\mu \rho \frac{k^2}{\varepsilon} \tag{B.12}$$

with C_μ being a constant.

The values for the turbulence kinetic energy k and turbulence dissipation rate ε for incompressible, non-buoyant fluids come directly from the respective differential transport equations:

$$\frac{\partial}{\partial x_j}\left(\rho U_j k\right) = \frac{\partial}{\partial x_j}\left[\left(\mu + \frac{\mu_t}{\sigma_k}\right)\frac{\partial k}{\partial x_j}\right] + P_k - \rho\varepsilon \tag{B.13}$$

$$\frac{\partial}{\partial x_j}\left(\rho U_j \varepsilon\right) = \frac{\partial}{\partial x_j}\left[\left(\mu + \frac{\mu_t}{\sigma_\varepsilon}\right)\frac{\partial \varepsilon}{\partial x_j}\right] + \frac{\varepsilon}{k}\left(C_{\varepsilon 1} P_k - C_{\varepsilon 2}\rho\varepsilon\right) \tag{B.14}$$

where $C_{\varepsilon 1}$, $C_{\varepsilon 2}$, σ_k and σ_ε are constants. P_k is the turbulence production term due to the viscous forces, modelled by:

$$P_k = \mu_t\left(\frac{\partial U_i}{\partial x_j} + \frac{\partial U_j}{\partial x_i}\right)\frac{\partial U_i}{\partial x_j} \tag{B.15}$$

A scalable wall function approach is used in near wall flow modelling to provide flexibility regarding boundary layer resolution.

While being a robust and efficient model in free stream conditions, the k-ε turbulence model has serious deficiencies e.g. when modelling spontaneous flow separation or flow along curved surfaces.

THE WILCOX K-OMEGA TURBULENCE MODEL

A model with significantly improved near-wall flow prediction characteristics, especially for spontaneous flow separation and reattachment, is the k-ω turbulence model. Being based on (B.9) as well, the turbulent viscosity within this model is calculated by:

$$\mu_t = \rho\frac{k}{\omega} \tag{B.16}$$

In this turbulence model transport equations for the turbulent kinetic energy k and the turbulent frequency ω are solved. The transport equation for the turbulent kinetic energy k and turbulent frequency ω, assuming incompressible, non-buoyant fluid, are:

$$\frac{\partial}{\partial x_j}\left(\rho U_j k\right) = \frac{\partial}{\partial x_j}\left[\left(\mu + \frac{\mu_t}{\sigma_k}\right)\frac{\partial k}{\partial x_j}\right] + P_k - \beta' \rho k \omega \tag{B.17}$$

$$\frac{\partial}{\partial x_j}\left(\rho U_j \omega\right) = \frac{\partial}{\partial x_j}\left[\left(\mu + \frac{\mu_t}{\sigma_\omega}\right)\frac{\partial \omega}{\partial x_j}\right] + \alpha\frac{\omega}{k}P_k - \beta \rho \omega^2 \tag{B.18}$$

In the above equations α, β, β', σ_k and σ_ω are constants, P_k is computed according to (B.15), like in the k-ϵ model. The unknown Reynolds stress tensor is computed according to the eddy viscosity hypothesis, (B.8). Near wall treatment is by an automatic switch from wall functions to low Reynolds wall treatment depending on boundary layer resolution.

A well known problem with the Wilcox k-ω turbulence model is its sensitivity to free stream turbulence conditions. Changing the value of ω at the inlet can result in significant variations of results.

THE SHEAR STRESS TRANSPORT (SST) TURBULENCE MODEL

A model especially designed for application on curved surfaces and the prediction of spontaneous separation on a smooth surface is the k-ω based Shear Stress transport (SST) turbulence model. To this end a blending of near surface treatment by the k-ω with free stream treatment by the k-ε model is implemented. To ensure the correct prediction of onset and amount of flow separation the correct prediction of turbulent shear stress transport is necessary. This is achieved by a limiter for eddy viscosity, preventing its over-prediction as is typical for the k-ε and k-ω models.

For the development of this model the k-ε formulation is transformed to a k-ω formulation. The Wilcox model is multiplied by a blending factor F_1, the transformed k-ε formulation correspondingly by a blending function $1 - F_1$. The resulting functions are added. This results in an application of the Wilcox model at the surface and the k-ε model from the edge of the boundary layer outwards.

For the SST model the Wilcox model, assuming incompressible, non-buoyant fluid, can be written as:

$$\frac{\partial}{\partial x_j}\left(\rho U_j k\right) = \frac{\partial}{\partial x_j}\left[\left(\mu + \frac{\mu_t}{\sigma_{k1}}\right)\frac{\partial k}{\partial x_j}\right] + P_k - \beta' \rho k \omega \tag{B.19}$$

$$\frac{\partial}{\partial x_j}\left(\rho U_j \omega\right) = \frac{\partial}{\partial x_j}\left[\left(\mu + \frac{\mu_t}{\sigma_{\omega 1}}\right)\frac{\partial \omega}{\partial x_j}\right] + \alpha_1\frac{\omega}{k}P_k - \beta_1 \rho \omega^2 \tag{B.20}$$

Assuming the same conditions, the transformed k-ε formulation can be written as:

$$\frac{\partial}{\partial x_j}\left(\rho U_j k\right) = \frac{\partial}{\partial x_j}\left[\left(\mu + \frac{\mu_t}{\sigma_{k2}}\right)\frac{\partial k}{\partial x_j}\right] + P_k - \beta' \rho k \omega \tag{B.21}$$

$$\frac{\partial}{\partial x_j}\left(\rho U_j \omega\right) = \frac{\partial}{\partial x_j}\left[\left(\mu + \frac{\mu_t}{\sigma_{\omega 2}}\right)\frac{\partial \omega}{\partial x_j}\right] + 2\rho\frac{1}{\sigma_{\omega 2}\omega}\frac{\partial k}{\partial x_j}\frac{\partial \omega}{\partial x_j} + \alpha_2\frac{\omega}{k}P_k - \beta_2 \rho \omega^2 \tag{B.22}$$

with the additional constants α_i, β_i, σ_{ki} and $\sigma_{\omega i}$, i being 1 or 2.

The above mentioned eddy viscosity limiter is formulated as follows:

$$v_t = \frac{\alpha_1 k}{\max(\alpha_1 \omega, SF_2)} \tag{B.23}$$

where

$$v_t = \frac{\mu_t}{\rho} \tag{B.24}$$

In these equations F_2 is a blending factor similar in function and application to the boundary layer to F_1, S is an invariant measure of the strain rate.

The blending functions F_1 and F_2 are of critical importance to the success of the method. The formulation of these blending functions is based on the distance to the nearest surface and on the flow variables, giving a range from 0 to 1 over the thickness of the boundary layer. They are given as:

$$F_1 = \tanh\left(arg_1^4\right) \tag{B.25}$$

with

$$arg_1 = \min\left[\max\left(\frac{\sqrt{k}}{\beta' \omega y}, \frac{500 v}{y^2 \omega}\right), \frac{4 \rho k}{CD_{kw} \sigma_{\omega 2} y^2}\right] \tag{B.26}$$

Here y is the distance to the nearest wall and v the kinematic viscosity. Further:

$$CD_{kw} = \max\left(2\rho \frac{1}{\sigma_{\omega 2} \omega} \frac{\partial k}{\partial x_j} \frac{\partial \omega}{\partial x_j}, 1.0 \times 10^{-10}\right) \tag{B.27}$$

$$F_2 = \tanh\left(arg_2^2\right) \tag{B.28}$$

with

$$arg_2 = \max\left(\frac{2\sqrt{k}}{\beta' \omega y}, \frac{500 v}{y^2 \omega}\right) \tag{B.29}$$

Wall functions in the SST turbulence model are treated the same way as in the k-ω turbulence model.

B.2.2. THE BASELINE EXPLICIT ALGEBRAIC REYNOLDS STRESS (BSL-EARSM) MODEL

The Explicit Algebraic Reynolds Stress Model is an extension to the standard eddy-viscosity based two equation models and, in this particular case, based on the *Baseline k-ω* (BSL) turbulence model which is closely related to the SST-model described above. The difference is the computation of the non-linear relation between Reynolds stresses and mean strain-rate and vorticity tensors instead of approximating the Reynolds stresses by the Boussinesq-approach based on the isotropic turbulent viscosity. This modification is aimed at rectifying shortcomings of the BSL-model against the SST model for example in the prediction of secondary flows or flows with high streamline curvature. Due to the higher-order terms included in the model, these and other flow phenomena are included without the need to solve additional transport equations.

The Reynolds stresses $\overline{u_i u_j}$ are related to the anisotropy tensor a_{ij} by:

$$\overline{u_i u_j} = k \left(a_{ij} + 2/3 \delta_{ij} \right),$$ (B.30)

where k is the turbulent kinetic energy and a_{ij} is the anisotropy tensor. a_{ij} is expressed by:

$$
\begin{aligned}
a_{ij} = &\beta_1 S_{ij} + \beta_3 \left(\Omega_{ik}\Omega_{kj} - \frac{1}{3} II_\Omega \delta_{ij} \right) + \beta_4 \left(S_{ik}\Omega_{kj} - \Omega_{ik}S_{kj} \right) + \\
&\beta_6 \left(S_{ik}\Omega_{kl}\Omega_{lj} + \Omega_{ik}\Omega_{kl}S_{lj} - \frac{2}{3} IV \delta_{ij} \right) + \\
&\beta_9 \left(\Omega_{ik}S_{kl}\Omega_{lm}\Omega_{mj} - \Omega_{ik}\Omega_{kl}S_{lm}\Omega_{mj} \right).
\end{aligned}
$$ (B.31)

The non-dimensional strain-rate and vorticity tensors S_{ij} and Ω_{ij} are defined by

$$S_{ij} = \frac{1}{2}\tau \left(\frac{\partial U_i}{\partial x_j} + \frac{\partial U_j}{\partial x_i} \right)$$ (B.32)

and

$$\Omega_{ij} = \frac{1}{2}\tau \left(\frac{\partial U_i}{\partial x_j} - \frac{\partial U_j}{\partial x_i} \right).$$ (B.33)

For a full description of the coefficients used in the above formulae see [5].

B.3. Volume Discretisation

To solve the RANS equations for an arbitrarily shaped volume, this volume (or *domain*) has to be divided into small, regularly shaped *control volumes*. Usually several millions of these control volumes are used. Typical shapes for these control volumes are tetrahedral (four nodes), pyramid (five nodes), wedge or prism (six nodes) or hexahedral (eight nodes). To calculate the flow through these control volumes the formulations given in Sections B.1 and B.2.1 are integrated over the control volume and transformed to surface integrals on the boundary faces of the control volumes by applying Gauss' Divergence Theorem. Integrating the differential conservation equations for mass and momentum in a Cartesian coordinate frame

$$\frac{\partial}{\partial \mathbf{x}_j} \left(\rho \mathbf{U}_j \right) = 0$$ (B.34)

$$\frac{\partial}{\partial t} \left(\rho \mathbf{U}_i \right) + \frac{\partial}{\partial \mathbf{x}_j} \left(\rho \mathbf{U}_j \mathbf{U}_i \right) = -\frac{\partial P}{\partial \mathbf{x}_i} + \frac{\partial}{\partial \mathbf{x}_j} \left[\mu_{eff} \left(\frac{\partial \mathbf{U}_i}{\partial \mathbf{x}_j} + \frac{\partial \mathbf{U}_j}{\partial \mathbf{x}_i} \right) \right]$$ (B.35)

yields the integrated equations

$$\int_s \rho \mathbf{U}_j \, dn_j = 0$$ (B.36)

$$
\begin{aligned}
\frac{d}{dt} \int_V \rho \mathbf{U}_i \, dV + \int_s \rho \mathbf{U}_j \mathbf{U}_i \, dn_j = \\
-\int_s P \, dn_j + \int_s \mu_{eff} \left(\frac{\partial \mathbf{U}_i}{\partial \mathbf{x}_j} + \frac{\partial \mathbf{U}_j}{\partial \mathbf{x}_i} \right) dn_j + \int_V S_{\mathbf{U}_i} \, dV
\end{aligned}
$$ (B.37)

where s and V denote surface and volume regions of integration, and dn_j are the differential Cartesian components of the outward normal vector of the individual control volume faces.

After discretisation of volume and surface integrals, the above equations in integral form become:

$$\sum_{ip} \dot{m}_{ip} = 0 \tag{B.38}$$

$$V\left(\frac{\rho \mathbf{U}_i - \mathring{\rho}\mathring{\mathbf{U}}_i}{\Delta t}\right) + \sum_{ip} \dot{m}_{ip}(\mathbf{U}_i)_{ip} =$$

$$\sum_{ip}(P\Delta n_i)_{ip} + \sum_{ip}\left[\mu_{eff}\left(\frac{\partial \mathbf{U}_i}{\partial \mathbf{x}_j} + \frac{\partial \mathbf{U}_j}{\partial \mathbf{x}_i}\right)\Delta n_j\right]_{ip} + \overline{S_{\mathbf{U}_i}}V \tag{B.39}$$

In the two above equations $\dot{m}_{ip} = \left(\rho \mathbf{U}_j \Delta n_j\right)_{ip}$, V is the control volume, Δt is the timestep and Δn_j is the discrete outward surface vector. The subscript ip denotes evaluation at the integration points of the control volume and the superscript ° refers to the old time level of the timeseries. In the above equations a First Order Backward Euler scheme has been assumed for simplicity, in practice a second order scheme is typically used for increased transient result accuracy.

In simulations utilising mesh motion or mesh deformation (e.g. due to the deformation of boundaries) it is necessary to take the motion and deformation of the control volumes in time into account. For a variable ϕ this is done by the application of the Leibnitz rule:

$$\frac{d}{dt}\int_{V(t)}\phi\,dV = \int_V \frac{\partial \phi}{\partial t}\,dV + \int_s \phi \mathbf{W}_j\,dn_j \tag{B.40}$$

with $\mathbf{W}_j$ being the velocity of the control volume boundary.

Applying (B.40) to the conservative equations in integral form yields:

$$\frac{d}{dt}\int_{V(t)}\rho\,dV + \int_s \rho\left(\mathbf{U}_j - \mathbf{W}_j\right)dn_j = 0 \tag{B.41}$$

$$\frac{d}{dt}\int_{V(t)}\rho\mathbf{U}_i\,dV + \int_s \rho\left(\mathbf{U}_j - \mathbf{W}_j\right)\mathbf{U}_i\,dn_j =$$

$$-\int_s P\,dn_j + \int_s \mu_{eff}\left(\frac{\partial \mathbf{U}_i}{\partial \mathbf{x}_j} + \frac{\partial \mathbf{U}_j}{\partial \mathbf{x}_i}\right)dn_j + \int_V S_{\mathbf{U}_i}\,dV \tag{B.42}$$

On the left hand side of both above equations the transient terms include the rate of change of volume of the deforming control volume while the advective terms include the net flux through the moving and deforming control volume's boundaries. During the motion and deformation of a control volume the Geometric Conservation Law $\frac{d}{dt}\int_{V(t)} dV = \int_s \mathbf{W}_j\,dn_j$ has to be satisfied. This Geometric Conservation Law simply states that the change of volume has to be equal to the net flux through the boundaries.

A peculiarity of the RANS solver used (CFX) is the handling of these control volumes. Instead of taking the control volumes as they are, new control volumes are built around

the nodes. Figure B.1 indicates how these new control volumes are generated. These control volumes have more faces than the original cells, theoretically increasing isotropy of the mesh and accuracy of the solution.
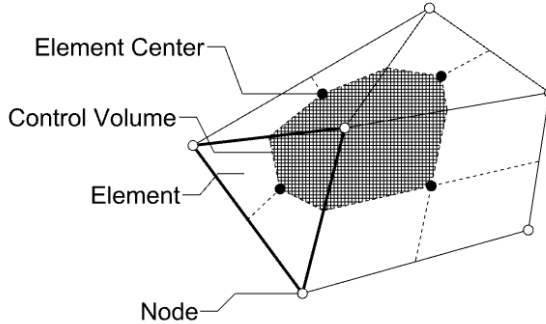
B

Figure B.1: Generation of new control volumes in CFX (reduced to 2-D) [5]

For each sector of the newly generated control volume in Figure B.2 the volume integrals are discretised and accumulated. On each face of the newly generated polyhedral control volume the surface integrals are discretised at the integration points (ip_n).
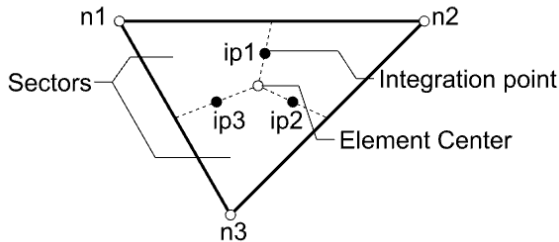

Figure B.2: Determination of integration points on control volume faces [5]

The RANS solver used (CFX) supports wholly unstructured meshes of various geometric control volume types, provided one-to-one cell face connectivity is maintained, i.e. no Split-Cartesian meshes. Typically the computational meshes consist of tetrahedral elements for the majority of the domain with prism or wedge elements for the resolution of boundary layers. Pyramid elements may be present in transition regions between the other two element types. Hexahedral elements are usually not used in this kind of unstructured meshes.

B.4. Solution of System of Equations

The system of equations generated from above equations is usually solved by utilising a segregated approach. In this approach the equations for momentum are solved based on a guessed pressure field, the pressure field is subsequently solved based on the computed momentum field and the momentum field corrected. Typical variants of this approach are the SIMPLE and PISO methods (*Ferziger et al.* [7]. To obtain a stable, convergent solution, solvers based on this kind of approach require a large number of iterations and small timestep lengths.

Untypically, ANSYS-CFX utilises a fully coupled approach to the solution of the system of equations [5]. In this approach a coefficient matrix is assembled from the linearised equations and solved using Algebraic Multi-Grid accelerated Incomplete Left-Upper factorisation. While requiring significantly more computational effort per timestep, timestep length for transient simulations can be significantly greater and residual reduction per timestep is significantly improved.

C

CODE IMPLEMENTATION

The program system, named FlexSail, is designed as an extension to the Navier-Stokes equation based flow solver ANSYS-CFX. ANSYS-CFX is the commercial result of the SEMPA-project conducted at the Munich Technical University 1995 - 1998 [8].

In the following the implementations generated within the scope of this thesis will be described.

C.1. FLUID-STRUCTURE-INTERACTION-COUPLING

The simulation of fluid-structure-interaction is based on the observation that flow-forces lead to a deformation of a body, which in turn affects the flow around it. Ideally, this interaction would be modelled in a single system of equations, describing the behaviour of the fluid medium as well as the solid body. Except for some simple cases, such a direct coupling has not yet been carried out. Typically, in fluid-structure-interaction simulations, two separate systems of equations are coupled by sequential exchange of information at the fluid-solid boundary.

This coupling at the boundary can be of different closeness. In cases where deformation of the solid boundary is deemed to be sufficiently small to not affect the flow behaviour, one-way coupling where only the flow-forces are transferred may suffice. In cases where the flow's behaviour is deemed to change due to the boundary's deformation, flow forces as well as changed boundary shape have to be transferred by two-way coupling.

Similarly, in a time-series, the coupling can either be weak or strong. In weak, or explicit, coupling, information transfer only takes place once per timestep per direction or even more seldom. This kind of coupling can be used if no time dependent solution is desired. In strong, or implicit, coupling, the information exchange is iterated within a timestep until transient solutions for both systems of equation are satisfied. This kind of coupling allows to simulate time-dependent processes.

In the program developed within the scope of this thesis a weak two-way coupling is implemented. Every few timesteps, nodal pressure data is communicated from the CFD-code to the FE-code, the resulting deformation of the sail is computed and transfered

123

back to the CFD-code. Based on this deformation, the boundaries representing the sail and the associated volume mesh are deformed.

ANSYS-CFX provides two interfaces for communication with external routines: User CEL (*CFX Expression Language*) routines and Junction Box routines. Both interfaces are designed to call user provided external subroutines with FORTRAN-77 being the preferred language. A range of ANSYS-provided F77 files can be included in the external code to provide standardised variables and access to various parts of ANSYS-CFX's data structure. To be able to use the more versatile features of FORTRAN-90, the files to be included were translated to F90 standard.

User CEL routines are based on User CEL functions defined in ANSYS-CFX, allowing communication of prescribed data in and out of CFX as calling arguments. As User CEL functions relate directly to variables computed during the iterative solution process (like mesh deformation), these routines and as a result associated User CEL functions are called from within ANSYS-CFX when appropriate for the computation of the related variable. They allow limited access to the ANSYS-CFX Memory Management System *MMS*. Data communicated are proprietary to each partition in parallel runs.

Junction Box routines are called from within ANSYS-CFX at user-defined points of the solving process. This can be at globally defined points like beginning of calculation or local points within each iteration. When calling a Junction Box routine it is not possible to communicate data as calling argument, instead full access to the MMS of the calling partition is granted. It is possible to communicate between Junction Box routines called by different partitions by using ANSYS-CFX's Parallel Virtual Machine (*PVM*) communication system.

Both kinds of interfaces provided are used in the implementation of the Fluid-Structure-Interaction coupling. Data communication in and out of ANSYS-CFX is accomplished on partition level by a User CEL routine called at the beginning of the mesh deformation step of each iteration. Data communicated are nodal pressures, current location and a side identifier as calling arguments, new nodal coordinates are received. Similarly, at each mesh deformation step a Junction Box routine is called to faciliate the communication between partitions and call the Finite-Element code. In the following sections both routines will be described in more detail.

C.1.1. USER CEL ROUTINE
The User CEL routine is called at the beginning of the mesh deformation calculation of each timestep on each partition. The following data are communcated as calling arguments:

- number of affected nodes in current partition

- number of variables pernode passed as arguments

- number of variables per node returned as arguments

- array of calling arguments

- array of return arguments

- result qualifier: good / bad

- MMS stack pointers

The calling arguments array contains current nodal positions, nodal pressure, component index of displacement vector and sail's side. The return arguments array contains the new nodal position components related to the displacement vector index. The sides identifier indicates windward or leeward side.

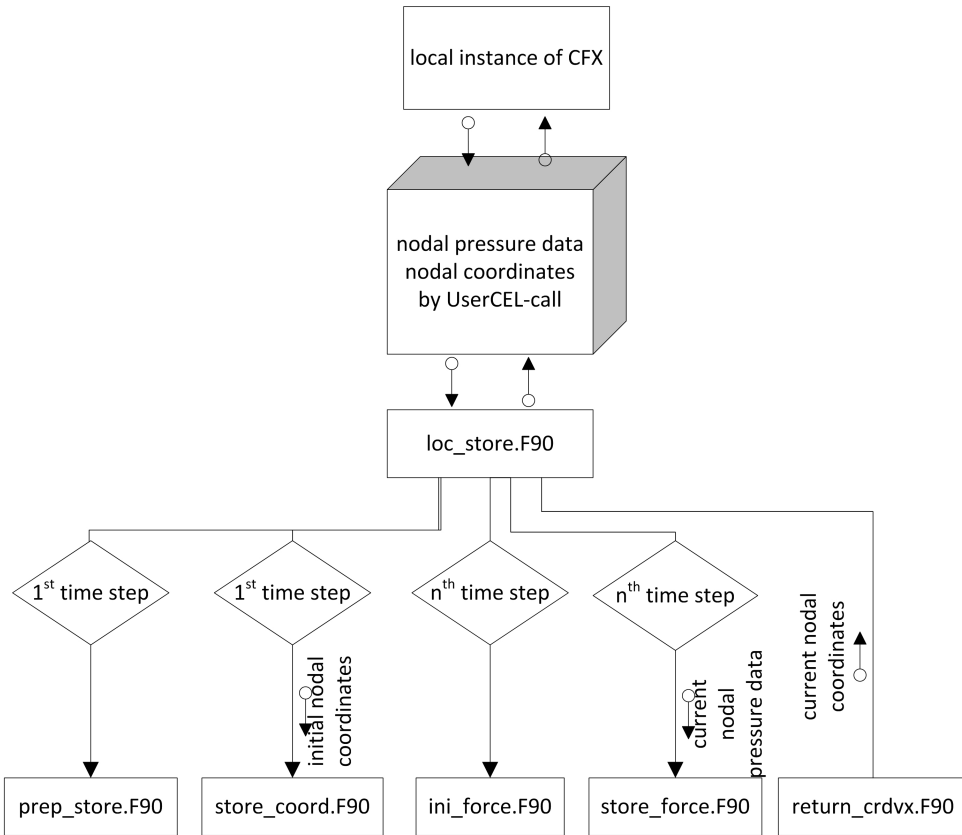The User CEL routine consists of various subroutines as per Figure C.1.

Figure C.1: Diagram of subroutines of User CEL routine.

The routine *loc_store* is called by ANSYS-CFX with arguments as described above. On the first call on each partition, storage space for the argument variables is allocated in the local MMS by *prep_store* and the initial nodal coordinates are stored by *store_coord*. Within ANSYS-CFX the update frequency for the sail's flying shape is defined as every n-th timestep. At every timestep before the n-th, the storage space for the nodal pressures is initialised by *ini_force* and the current pressures stored by *store_force*. On each call the nodal coordinates stored within the MMS at that time are read by *return_crdvx* and returned to the calling routine. The coordinates stored in the MMS are regularly updated by the Junction Box routine according to the FEM calculations.

C.1.2. JUNCTION BOX ROUTINE

The Junction Box Routine is called at user-defined locations of the ANSYS-CFX iteration, right before the beginning of the mesh deformation computation. By definition, no arguments are passed, except for pointers to the ANSYS-CFX MMS stacks. The structure of the Junction Box Routine is shown in Figure C.2.

The Junction Box routine's master routine *par_comm* first checks whether ANSYS-CFX is running in sequential or parallel mode. In case of sequential, execution is stopped. For conveniences sake the execution is limited to parallel, as it is impossible to handle meaningful mesh sizes in sequential mode. Older versions designed for sequential execution exist. At the second time step the inter-partition communication is set up, humpbacking on ANSYS-CFX's PVM system. This is done by calling *mastercom* respectively *slavecom* and includes setting up the data areas required for the exchange within the user part of the MMS. Similarly the nodal coordinates attached to the sail are communicated to the master from each partition.

At the third time step the reference mesh in initial and pre-deformed state is read from file by the master partition by calling *read_structure*. Nodal and facial mappings are generated on the master partition by calling *node_map* and *face_map*.

At every n-th time step (e.g. every tenth) the locally stored current nodal pressure data are communicated from the slave partitions to the master partition by calling *force_com*. On the master partition they are assembled for the whole surface mesh and stored by calling *sort_force*. Subsequently the FEA routine is called on the master partition by calling subroutine *flexsail*. After sucessfully running the FEA routine, the new nodal coordinates are distributed to all concerned partitions by calling *coord_com* on all partitions.

C.2. STRUCTURAL CODE

The structural code is implemented in FORTRAN90. Basically, two versions of the structural code exist, a stand-alone version, calculating a flying shape based on a pre-defined pressure distribution, and one version linked to ANSYS-CFX. Generally, both versions are similar, therefore they will be described as one, with the differences pointed out. The structure is depicted in Figure C.3.

The structural code is controlled by routine *flexsail_pre*, respectively subroutine *flexsail*. In the stand-alone version the user is prompted whether a pressure distribution should be read from a file, if not, for a constant pressure difference between both sides of the sail.

C.2.1. DATA PREPARATION AND SETTING UP OF SYSTEM OF EQUATIONS

Next, both versions call *read_loadcase*. In the stand-alone version, *read_loadcase* reads the surface mesh, structural and solution parameters from file, if prompted the pressure distribution as well. In the FSI-version the initial and current (deformed) mesh as well as nodal pressures are read from the MMS, structural and solution parameters are read from file.

Next, subroutines *get_structure* and *vmasses* are called. By these subroutines element data as required for the formulae given in Section 3.1.2 and virtual masses as described in Section 3.2.2 are calculated. Nodal forces are calculated from pressure data and element
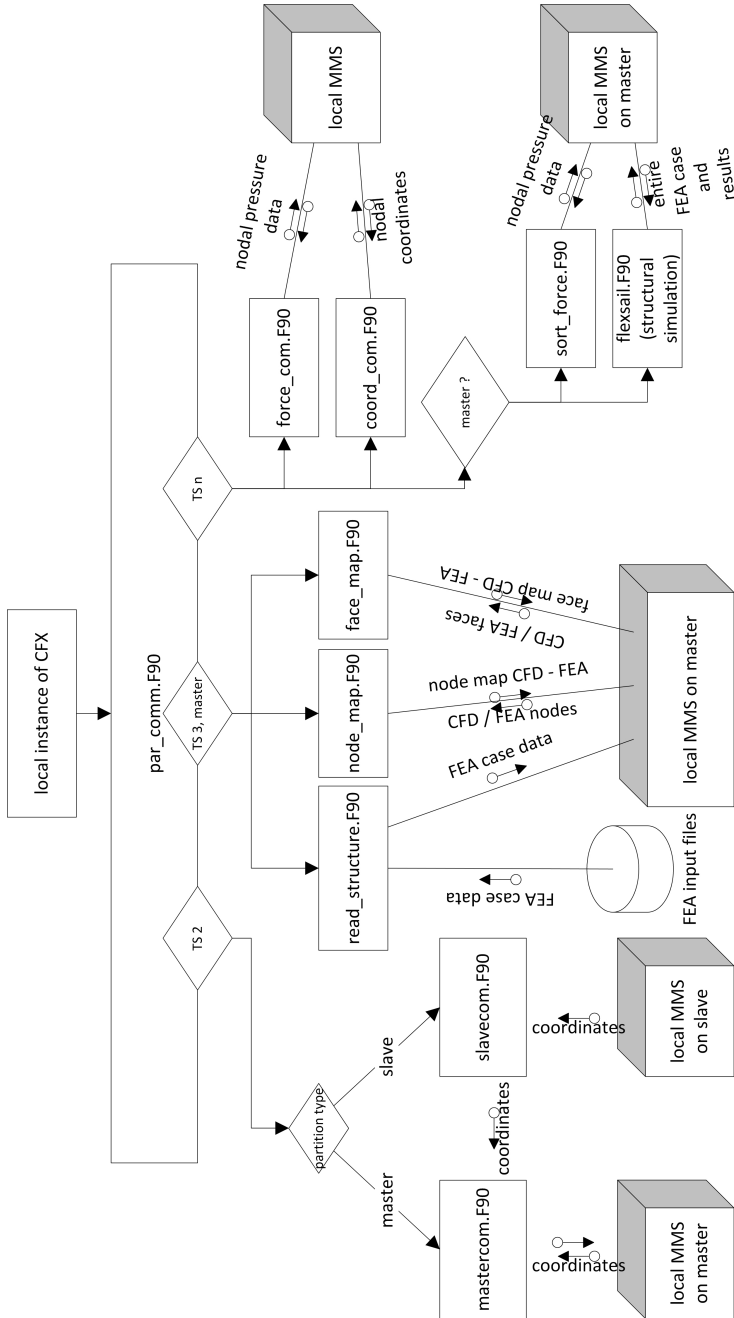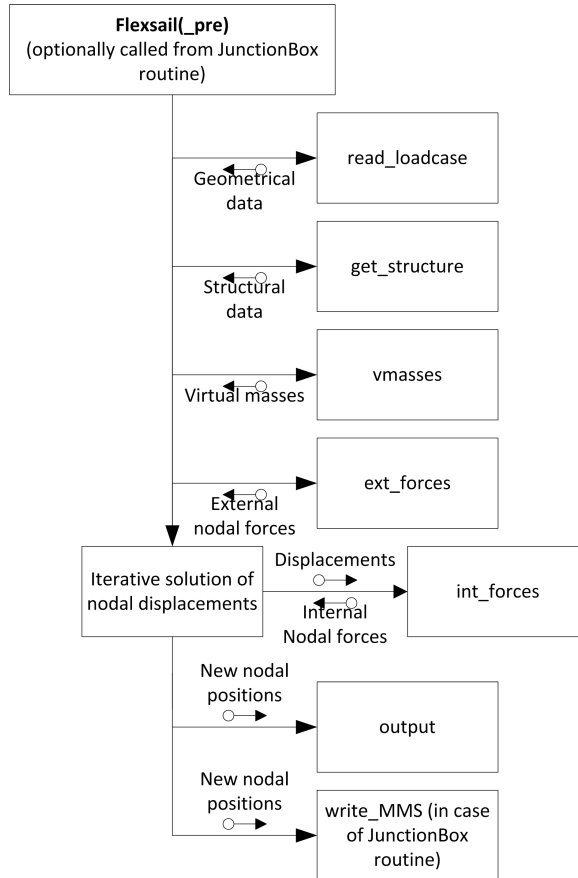
Figure C.2: Diagram of subroutines of Junction Box routine.

Figure C.3: Diagram of program *FlexSail*.

areas and normal vectors by subroutine *ext_forces*. In the FSI-version the global node-displacement vector is updated to the current geometry.

C.2.2. SOLVING

The solving part is, again, the same for both versions. For simplicity's sake it is contained in the main routine *flexsail*, respectively *flexsail_pre*. It basically consists of two nested loops: An inner loop between kinetic energy peaks and an outer loop for global convergence.

At the beginning of each outer loop, nodal velocities and correspondingly total kinetic energy are initialised to zero. Following that, external forces based on the current deformed geometry are computed by calling *ext_forces*. During the first 101 outer loops displacements of boundary conditions and prescribed element deformations (e.g. sheet length changes) are applied by a ramping process.

At the first time step (first inner loop) per outer loop, the internal nodal forces from element deformations are computed and yield, together with the external forces, the left hand side of (3.49). Nodal velocities are computed according to (3.54). The new nodal positions are computed by (3.51). Following that, total kinetic energy and residuals are computed.

At the beginning of each following time step a left hand side of (3.49) is computed by calling *ext_forces*. Nodal velocities and positions are computed by (3.52) and (3.51). Total kinetic energy and residuals are computed. During the time step-iterative procedure total kinetic energy is traced. If a maximum is detected, the pseudo-time of the actual maximum is computed by (3.55) and nodal displacements corrected accordingly. At this point the inner loop is terminated and the outer loop advances by one. If the residuals fall below a predefined threshold, the solution is deemed to be converged and the outer loop terminates as well. Last the subroutine *output* is called.

REFERENCES

[1] M. Stein and J. M. Hedgepeth, *Analysis of Partly Wrinkled Membranes*, Tech. Rep. (NASA, 1961).

[2] S. Wilkinson, *Partially Separated Flow Around Masts and Sails*, Ph.D. thesis, University of Southampton (1984).

[3] I. H. Abbott and A. E. von Doenhoff, *Theory of Wing Sections* (Dover Publications Inc., New York, 1959).

[4] J. H. Milgram, *Section Data for Thin, Highly Cambered Airfoils in Incompressible Flow*, Tech. Rep. (NASA, 1971).

[5] *ANSYS CFX-Solver Theory Guide*, Ansys Inc., 12th ed. (2009).

[6] J. V. Boussinesq, *Essai sur la théorie des eaux courantes,* in *Mémoires présentés par divers savants à l'Académie des Sciences XXIII*, Vol. 1 (1877) pp. 1–680.

[7] J. H. Ferziger and M. Peric, *Computational Methods for Fluid Dynamics*, 3rd ed. (Springer, 2002).

[8] P. Luksch, U. Maier, S. Rathmeyer, and W. Weidmann, *SEMPA - Software Engineering Methods for Parallel Applications in Scientific Computing*, Tech. Rep. (Lehrstuhl für Rechnertechnik und Rechnerorganisation, Institut für Informatik, Technische Universität München, 1998).

C

CURRICULUM VITÆ

Hannes Florian RENZSCH

Hannes Renzsch was born on June 1st in Bonn, Germany. He attended the Beethoven Gymnasium Bonn from 1990 to his graduation in 1999. Following this, he completed a year of social service with the German Red Cross. From 2000 he studied Naval Architecture at University of Applied Sciences Kiel. The studies were interrupted for one term in 2001/02 due to working as boatswain on a sailing yacht voyaging from Germany to the Caribbean. He graduated in 2005 with a thesis on the simulation of viscous free surface flows around sailing yachts.

Following his graduation, he started working at the Yacht Research Unit Kiel, focussing on numerical sail aerodynamics, fluid structure interaction and unsteady ship dynamics. During this work he was actively involved in various projects for international sailing campaigns, e.g. in the 32nd America's Cup and the 2006/07 Volvo Ocean Race. His last project at the Yacht Research Unit Kiel was the analysis of platform and wing aerodynamics for the ACEA Shared Design Team for the 34th America's Cup. During this time he repeatedly gave lectures at University of Applied Sciences Kiel about ship and sailing yacht fluid dynamics.

In 2009 he commenced working on his PhD research at the section Ship Hydromechanics and Structures of the Delft University of Technology about fluid-structure-interaction simulation of downwind sails subjected to viscous flow. The result of this work is presented in this thesis.

In 2011 he left the Yacht Research Unit Kiel for an appointment at the R&D department of the Hamburg Ship Model Basin HSVA as project leader. In 2013 he left HSVA for a lecturing contract at University of Applied Sciences Kiel and to start his own consulting company which is still active to this day. Since 2016 he is a member of the department for product development at Nobiskrug Shipyard Rendsburg, focussing on the application of CFD methods in the mega-yacht design process.

LIST OF PUBLICATIONS

JOURNAL PUBLICATIONS

2. **H. Renzsch and K. Graf**, *Flying Shape Prediction of Asymmetric Spinnakers – An Experimental Data Set for Validation of FSI-Simulations*, International Journal of Small Craft Technology, Trans. RINA, Part B2 **158**, 55 (2017).

1. **H. Renzsch and K. Graf**, *Fluid Structure Interaction Simulation of Spinnakers – Getting Closer to Reality*, International Journal of Small Craft Technology, Trans. RINA, Part B2 **153**, 71 (2011).

OTHER PUBLICATIONS

15. **K. Graf, J. Meyer, H. Renzsch, C. Preuss**, *Investigation of modern sailing yachts using a new free-surface RANS-code*, International Conference on Innovation in High Performance Sailing Yachts, 4th Edition (2017).

14. **J. Meyer, H. Renzsch, K. Graf and T. Slawig**, *Advanced CFD-Simulations of free-surface flows around modern sailing yachts using a newly developed OpenFOAM solver*, The 22nd Chesapeake Sailing Yacht Symposium (2016).

13. **K. Graf, H. Renzsch and J. Meyer**, *Prediction and optimization of aerodynamic and hydrodynamic forces and boat speed of foiling catamarans with a rigid wing and a jib*, The 22nd Chesapeake Sailing Yacht Symposium (2016).

12. **H. Renzsch**, *Challenges in Modelling of Membrane Structures*, Airborne Wind Energy Conference (2015).

11. **H. Renzsch and K. Graf**, *An Experimental Validation Case for Fluid-Structure-Interaction Simulations of Downwind Sails*, The 22nd Chesapeake Sailing Yacht Symposium (2013).

10. **K. Graf and H. Renzsch**, *Neuartiger Segelantrieb als Hilfsantrieb für Megayachten und Handelsschiffe*, Schiff & Hafen **02/2013**, 22 (2013).

9. **H. Renzsch**, *A Simple Approach for Preliminary Assessment of the Feasibility of Wind-powered Auxiliary Propulsion*, 11th International Marine Design Conference (2012).

8. **J. Marzi, S. Gatchell and H. Renzsch**, *The need for 'green' bulk carriers*, The Naval Architect, The Royal Institution of Naval Architects, **June 2012**, 34 (2012).

7. **H. Renzsch and K. Graf**, *Fluid Structure Interaction Simulation of Spinnakers – Towards Simulation Driven Sail Design*, 21st International HISWA Symposium on Yacht Design and Yacht Construction (2010).

6. **H. Renzsch and K. Graf**, *Fluid Structure Interaction Simulation of Spinnakers – Getting Closer to Reality*, 2nd International Conference on Innovation in High Performance Sailing Yachts (2010).

5. **K. Graf, C. Böhm and H. Renzsch**, *CFD- and VPP-Challenges in the Design of the New AC90 America's Cup Yacht*, The 19th Chesapeake Sailing Yacht Symposium (2009).

4. **H. Renzsch, O. Müller and K. Graf**, *FlexSail – A Fluid-Structure-Interaction Program for the Investigation of Spinnakers*, International Conference on Innovation in High Performance Sailing Yachts (2008).

3. **H. Renzsch, O. Müller, M. Hoffmann, K. Graf**, *Strömungssimulation und Windkanal-experiment für die Analyse von Vormwind-Segeln*, 27. Symposium Yachtbau und Yachtentwurf (2006).

2. **K. Graf and H. Renzsch**, *RANSE Investigations of Downwind Sails and Integration into Sailing Yacht Design Processes*, 2nd High Performance Yacht Design Conference (2006).

1. **K. Graf, E. Wolf and H. Renzsch**, *Strömungssimulation und Ge-schwindigkeitsprognose für Segelyachten*, 24. Symposium Yachtbau und Yachtentwurf (2003).